Università degli Studi di Perugia

Dottorato di Ricerca in Fisica
XXIV Ciclo

Measurement of the Atmospheric Muon Flux on Ground with the AMS-02 Detector

Matteo Duranti

Tutori

Prof. Bruna Bertucci
Dott. Alberto Oliva

Coordinatore del Corso di Dottorato

Maurizio Busso

Anno Accademico 2010-2011

What's the matter?
What's the antimatter?
Does it antimatter?
Wes Niske

Contents

Introduction

The AMS-02 instrument is a magnetic spectrometer conceived to perform cosmic ray measurements in space, on board of the International Space Station (ISS). Search for anti-matter, either anti-nuclei of primordial origin or light anti-matter from exotic sources, is the primary goal of this experiment, successfully operating in orbit since May 19, 2011.

The assembly of the detector ended in July 2010 and, after its calibration with beam particles at CERN, the instrument was shipped to the Kennedy Space Center at the end of August to be integrated with the mechanical and electrical interfaces to the Shuttle and ISS. During the seven months spent by the instrument in the Space Shuttle Processing Facility prior to the launch, extended periods of data taking were carried in order to finalize the data acquisition procedures and to continue the detectors calibration on ground. The study of the detector performances before launch was in fact mandatory to disentangle possible effects arising after the mechanical and thermal stresses encountered in its operation in space and to perform a careful evaluation the simulation and reconstruction software with a relatively well know flux of particles, as the atmospheric muons, and negligible physics backgrounds.

The measurement of the flux and charge ratio of atmospheric muons presented in this thesis is the result of the analysis of the $\sim 3 \cdot 10^8$ triggers recorded during the AMS-02 commissioning period at the KSC. This analysis not only has been the first measurement of a particle flux performed with the completed AMS-02 detector but it also represented a severe test bench for the simulation and reconstruction software over a wide range of energies. Several modifications to the reconstruction and simulation software had to be implemented in order to obtain the presented results, and more will be needed to improve the performed measurement at low energies. This dissertation is focused on the main topics of the muon measurement; we explicitly choose not to report the details of the intermediate steps of the work, as well as the contributions to construction, commissioning and running of the silicon tracker during the assembly and testing with beams during the PhD period.

In the following, after a brief introduction on the Cosmic rays and the characteristics of atmospheric particle fluxes on ground (Chapter 1) an overall description of the AMS-02 instrument and its physics goals will be given (Chapter 2). A set of $\sim 10^9$ muon events have been generated with Monte Carlo techniques, simulated and reconstructed in the detector in order to assess the detector acceptance and reconstruction efficiency. The MC sample has been also used to qualify the selection process and to study in details the unfolding technique used to account

for the momentum resolution. A detailed discussion of the relevant characteristics of the MC generation and the performed studies on the simulated sample are presented in Chapter 3. An accurate pre-selection of the DATA sample was performed to discard the DAQ commissioning periods with peculiar detector or trigger configurations. This has been the first step of our study, followed by the requirements to define well reconstructed muon events in the detector. A thorough comparison between DATA and MC has been then carried through all the intermediate steps of the analysis in order to validate the selection criteria versus the simulation results: all the details are described in Chapter 4. The flux and muon charge ratio measurements are finally reported in Chapter 5.

Chapter 1

Cosmic Rays

Cosmic Rays (CRs) are charged particles that reach the Earth atmosphere in all directions, from the outer space, after they traveled throughout the Galaxy for several million years. The CR flux detected at Earth is predominantly composed by nuclei ($\sim$85% protons, $\sim$12% helium and $\sim$1% heavier nuclei), while electrons and positrons contribute with $\sim$2% to the total flux [26].

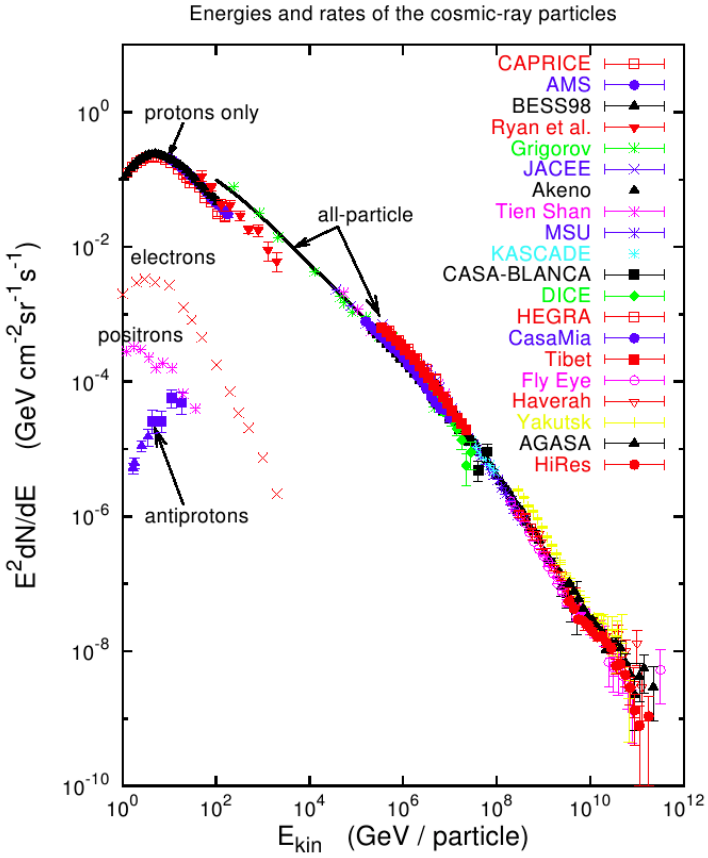

Figure 1.1: All particle CR spectrum [33]. The spectrum extends to many orders of magnitude. Measurements from different experiments are shown.

The CR energies span over a wide interval, from eV to 10^{21} eV, whereas the all-

species differential fluxes vary significantly: from particle/cm^2/second/MeV up to particle/km^2/century/ZeV respectively. CRs with lowest energy, eV-GeV, are of solar origin and make up the solar wind [25].
CRs with energy between 10^9 and 10^{18} eV are thought to originate and accelerated in supernova explosions occurring in the Galaxy. In this picture, particle are accelerated by non-thermal mechanisms that lead to the power-law spectrum described in Fig. 1.1:

$$\Phi = \Phi_0 E^{-\gamma} \tag{1.1}$$

where the spectral index γ takes the value ~ 2.7. The low energy part of the CR spectrum ($E \lesssim 10$ GeV) is influenced by the solar wind as discussed in Sec. 1.2.

At energies $\sim 10^{15}$ eV the CR spectrum has a steeping, the *knee*, characterized by a sudden variation of the all-particle spectral index from 2.7 to 3.1 (Fig. 1.1). At higher energies, the *ankle* is observed at $\sim 10^{18}$ eV, which marks another transition to a flatter spectrum, with $\gamma \approx 2.7$. As the nature and the origin of these structures are still debated, they are thought to be related to the transition between the galactic and the extra-galactic component of the CR flux [14]. In the highest energy region $E \gtrsim 10^{19}$ eV, the Greisen-Zatsepin-Kuzmin (GZK) suppression is expected on the flux, due to inelastic interactions of cosmic rays with the CMB photons [29].

1.1 Cosmic Rays in the Galaxy

The origin and propagation of galactic CRs are among the major subjects of the modern astrophysics. In this chapter we will focus on the CR nuclear component, which accounts for $\sim 99\%$ of the total flux and it is relevant the subject of this thesis, i.e., the atmospheric muon physics. CR nuclei detected at energies from ~ 100 MeV to ~ 1 PeV are believed to be produced by galactic sources such as supernova remnants (SNRs), pulsars or stellar winds, by means of diffusive shock acceleration (DSA) mechanisms.
From the energetic point of view, the SNR scenario is completely acceptable and seems more likely than other scenarios (stellar winds and pulsars). The average energy density of CRs is $\sim$ eV/cm^3. In a galactic disc volume of 10^{63} cm^3, the total energy content is $\sim 10^{67}$ eV. Given the average CR lifetime ($\sim 3 \cdot 10^{14}$ s), the total energy, to inject into the system to have the measured CR flux, is $\sim 5 \cdot 10^{40}$ erg/s. Assuming a supernova explosion every 50 years and a typical release of energy of 10^{50} erg for a single explosion this lead to a production of $6 \cdot 10^{40}$ erg/s.
After acceleration, CRs are released in the circumstellar environment, where they pass trough a long chain of transformations in their energy spectra and elemental composition. Their galactic origin is well confirmed looking to the relative abundances of the various nuclei. Comparing them in the CRs and in the solar system a clear correlation is seen (see Fig. 1.2). Such correlation can be simply explained if one considers that the solar system elemental abundance is representative of the typical CR sources. On the other hand, the discrepancies

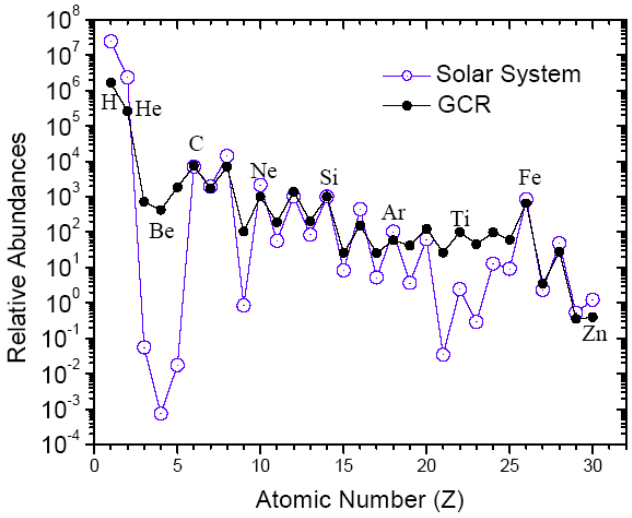

Figure 1.2: Relative abundances of the various elements in CRs and in the solar system [34]. The correlation with solar system well confirms a galactic origin for CRs, while the discrepancies in the Li-Be-B and sub-Fe groups indicate spallation properties of CRs in the ISM.

in the Li-Be-B ($Z = 3$-5) and in the sub-Fe ($Z = 22$-25) groups are signatures of secondary CR production, called *spallation*, due to nuclear collisions of CRs with the ISM gas. The slightly less pronounced odd-even effect observed in CRs can explained in term of spallation too.

1.1.1 Acceleration in SNRs

The DSA theory is able to explain the power-law spectrum ($\Phi \propto E^{-\gamma}$) observed in galactic CRs above ~ 10 GeV/n of energy, i.e., where they are not influenced by the solar wind (see Sec. 1.2). The DSA mechanism is based on the *first order Fermi acceleration theory*, which leads to an efficient energy gain through individual head-on collisions of accelerated particles with the shock waves generated by SNR explosions. For strong shocks, the spectral index is close to the value $\nu = 2$ and it is independent on the SNR properties such as ambient density, magnetic field intensity or turbulence. This mechanism therefore provides an excellent physical reason why power-law energy spectra with a unique spectral index may occur in different astrophysical environments [26].

1.1.2 Interstellar Propagation

The interstellar propagation of CR nuclei is dominated by particle transport in the turbulent magnetic field and interactions with the matter, that is generally described by a diffusion-transport equation including source distribution functions, magnetic diffusion, energy losses, hadronic interactions, decays, diffusive reacceleration and convective transport (the latter is not considered in the following). Models of CR propagation in the Galaxy employ analytical, semi-

analytical or fully numerical calculation frameworks [48]. Very popular is the *diffusive-reacceleration* model implemented by many propagation models such as GALPROP[1], which numerically solves the cosmic ray propagation equation for a cylindrical diffusive region with a realistic interstellar gas distribution and source distribution. The propagation equation of the diffusive-reacceleration model for a CR species j is given by:

$$\frac{\partial \mathcal{N}_j}{\partial t} = q_j^{tot} + \vec{\nabla} \cdot \left(D_{xx} \vec{\nabla} \mathcal{N}_j \right) - \mathcal{N}_j \Gamma_j^{tot} + \frac{\partial}{\partial p} p^2 D_{pp} \frac{\partial}{\partial p} p^2 \mathcal{N}_j - \frac{\partial}{\partial p} \left(\dot{p}_j \mathcal{N}_j \right) \quad (1.2)$$

where $\mathcal{N}_j = dN_j/dVdp$ is the CR density of the species i per unit of total momentum p. The source term can be written as $q_j^{\rm tot} = q_j^{\rm pri} + q_j^{\rm sec}$, where the *primary* acceleration spectrum, $q_j^{\rm pri} = q_0 \, (R/R_0)^{-\nu}$, describes the SNR acceleration (power-law type with spectral indices ν) and it is normalized to the abundances q_j^0 at the reference rigidity R_0 (the rigidity is defined as the ratio $R = pc/Ze$). The *secondary* source term, $q_j^{sec} = \sum_k \mathcal{N}_k \Gamma_{k \to j}$, describes the products of decay and spallation of heavier CR progenitors with number density $\mathcal{N}_k$. For collisions with the interstellar gas:

$$\Gamma_{k \to j} = \beta_k c \sum_{\rm ism} \int_0^\infty n_{\rm ism} \sigma_{k \to j}^{\rm ism}(E, E') dE' \,, \quad (1.3)$$

where $n_{\rm ism}$ are the number densities of the ISM nuclei, $n_H \approx 0.9 \, cm^{-3}$ and $n_{He} \approx 0.1 \, cm^{-3}$, and $\sigma_{k \to j}^{\rm ism}$ are the fragmentation cross sections for the production of a j-type species at energy E from a k-type progenitor of energy E' in hydrogen or helium targets. $\Gamma_j^{tot} = \beta_j c \left(n_H \sigma_{j,H}^{tot} + n_{He} \sigma_{j,He}^{tot} \right) + \frac{1}{\gamma_j \tau_j}$ is the total destruction rate for inelastic collisions (cross section σ^{tot}) and/or decay for unstable particles (lifetime τ). The spatial diffusion coefficient D_{xx} is taken as spatially homogeneous and rigidity dependent as $D_{xx}(R) = \beta D_0 \, (R/R_0)^{\delta}$, where D_0 fixes its normalization and the parameter δ specifies its rigidity dependence. Diffusive reacceleration is described as diffusion process acting in momentum space. It is determined by the coefficient D_{pp} for the momentum space diffusion: $D_{pp} \propto v_A/D$, where v_A is the Alfvén speed of plasma waves moving through the ISM. The last term describes Coulomb and ionization losses by means of the momentum loss rate $\dot{p}_j$. In two-dimensional models, the diffusion region is a cylinder region of radius r_{max} and half-thickness L. The boundary conditions $\mathcal{N}_j(r{=}r_{max}){=}0$ and $\mathcal{N}_j(z{=}\pm L){=}0$ completely characterize the solution of Eq. 1.2 in steady-state conditions ($\partial \mathcal{N}_j/\partial t = 0$). The local interstellar spectrum (LIS) can be therefore computed for each species at the solar system coordinates $r_\odot = 8.5 \, kpc$ and $z = 0$:

$$\Phi_j^{\rm LIS}(E) = \frac{c A_j}{4\pi} \mathcal{N}_j(r_\odot, p) \quad (1.4)$$

where A_j is the mass number and the flux $\Phi_j^{\rm LIS}$ is given in units of kinetic energy per nucleon E.

[1] `http://galprop.stanford.edu`

This description may reproduce well the CR elemental fluxes at energies of $\sim 100\,\mathrm{MeV} - 100\,\mathrm{TeV}$ per nucleon. However, the difficulty in disentangling experimentally measurable effects due to a single physics process, results in an effective degeneracy of the parameters that specify these models. Several complementary constraints on CR source and propagation properties can be extracted from the measurement of their chemical and isotopic composition. In particular, *secondary-to-primary* ratios of stable nuclei, such as ^{3}He/^{4}He, B/C or sub-Fe/Fe ratios, are used to constrain the galactic diffusion coefficient spectral slope δ, the ratio D_0/L and the Alfvén speed v_A. Furthermore, the D_0/L parameter degeneracy may be resolved using *unstable-to-stable* isotopic ratios such as ^{10}Be/^{9}Be, or ^{26}Al/^{27}Al, because the radioactive isotopes such as ^{10}Be (lifetime $\tau \sim 1.5\,\mathrm{Myr}$) are insensitive to the boundaries of the diffusion region. Thus, simultaneous measurements of B/C and ^{10}Be/^{9}Be ratios allow the determination of the basic transport parameters of the model. Additional data on the *primary* nuclei spectra (such as p, He, C, N, O, or Fe) allows to determine the source parameters such as the abundance factors q_j^0 and their acceleration log-slope ν. Finally, the results of such calculations can be used to predict the secondary production of other rare particles such as $e^{\pm}$, $\overline{p}$ or $\overline{d}$, and to set limits on the search for exotic signals such as, e.g., those arising from the annihilation of dark matter particles.

1.2 Cosmic Rays in the Heliosphere

At the final stages of their travel toward the Earth, CRs are influenced by the solar wind, that extends up to the boundaries of the solar system. The energy spectrum of CRs in the solar system is modulated for energies up to several GeV/n. This is due to a magnetized plasma in hydrodynamic expansion: the solar wind. In fact a fully ionized gas, basically constituted of low energy electrons and protons ($E \sim 0.5\,\mathrm{MeV}$) is pushed radially out of the Sun's corona.
Once the plasma has left the corona, the dynamic pressure of this wind dominates over the magnetic pressure through most of the solar system, so that the magnetic field lines are driven out by the plasma. The combination of the outflowing particles motion with the Sun's rotation leads to a spiral pattern for the flow. The region of space in which the solar wind is dominant is called heliosphere. The charged particles that penetrate the heliosphere are diffused and energetically influenced by the expanding solar wind. As this effect involves all the cosmic rays that we detect at Earth (or in near space), it must be taken into account for interpretation of the measured spectra.
A simple description of this effect is the *force-field* method [28], which consists in regarding the solar wind as a radial field with a potential ϕ. Within this description, the solar-modulated spectrum, $\Phi^{\odot}$, is related to the LIS spectrum of Eq. 1.4 through the simple relation:

$$\Phi^{\odot} = \frac{E^2 - m^2c^4}{(E + Ze\phi)^2 - m^2c^4}\Phi^{LIS}(E + Ze\phi) \tag{1.5}$$

The proportionality factor between and $\Phi^{\odot}$ and Φ^{LIS} is the ratio of the two corresponding squared momenta, $p_{\odot}^2/p_{LIS}^2$; the modulation parameter ϕ may be inter-

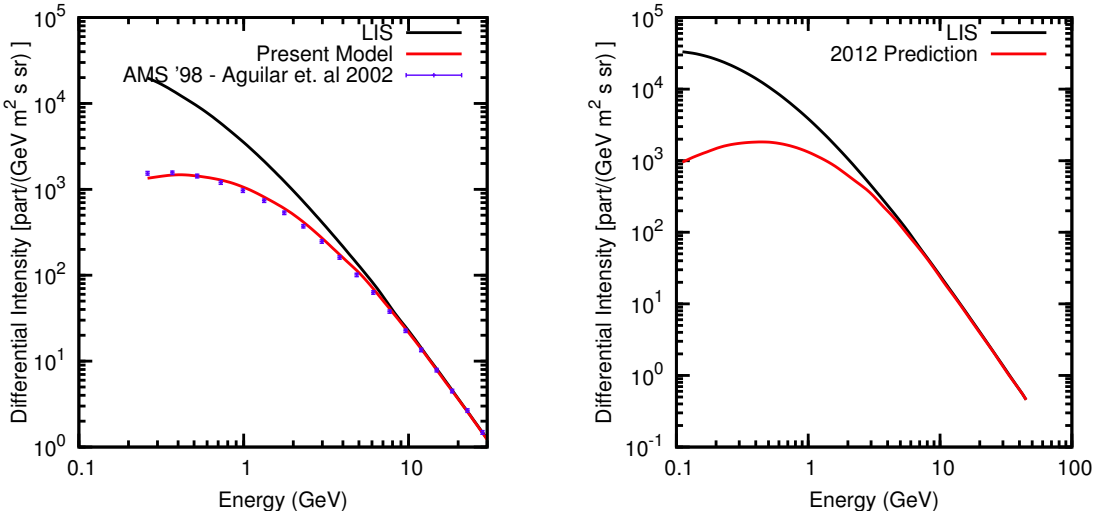

Figure 1.3: Interstellar (black) and solar modulated (red) proton spectrum [16]. Left: calculation for the solar activity condition of June 1998 in comparison with the AMS-01 data. Right: predictions for January 2012.

preted as the characteristic energy loss, per charge unit, of CR particles in the heliosphere. Its value ranges between ~ 300 MV (solar minimum) and ~ 1500 MV (solar maximum), depending on the solar activity conditions. More refined models includes curvature, gradient and drifts effects. Such models describe the modulation dependence on the charge sign of CR particles and magnetic polarity of the solar wind [16]. In Fig. 1.3 the effect of the solar modulation on the proton flux is shown. The proton LIS is compared with the modulated spectrum for the periods of June 1998 and January 2012.

1.3 Cosmic Rays in the Magnetosphere

The last obstacle for cosmic rays before being detected by an Earth orbiting detector is the Earth magnetosphere, that extends its influence on the cosmic radiation modulating the low-energy part of the observed spectra (up to ~ 20 GV of rigidity).
To first approximation, the geomagnetic field can be represented as an offset and tilted dipole field with moment $M = 8.1 \cdot 10^{25}$ G cm^3, an inclination of 11° to the axis of Earth rotation and a displacement of about 400 km with respect to the Earth center. Because of the offset, the geomagnetic field, for a fixed altitude from the ground, is characterized by distortion, the highest of which is in the South Atlantic, where the field strength is the weakest. The charged particles penetrate deeper in this region and the radiation becomes stronger. This high radiation phenomenon is the so called *South Atlantic Anomaly* (SAA).
The most important aspect for CR measurements is the determination of the geomagnetic cut-off [47]. Charged particles traversing the magnetic field experience the Lorentz force that produces a curved path for low rigidity particles. Cosmic rays can thus be prevented form reaching the detector, depending on their rigid-

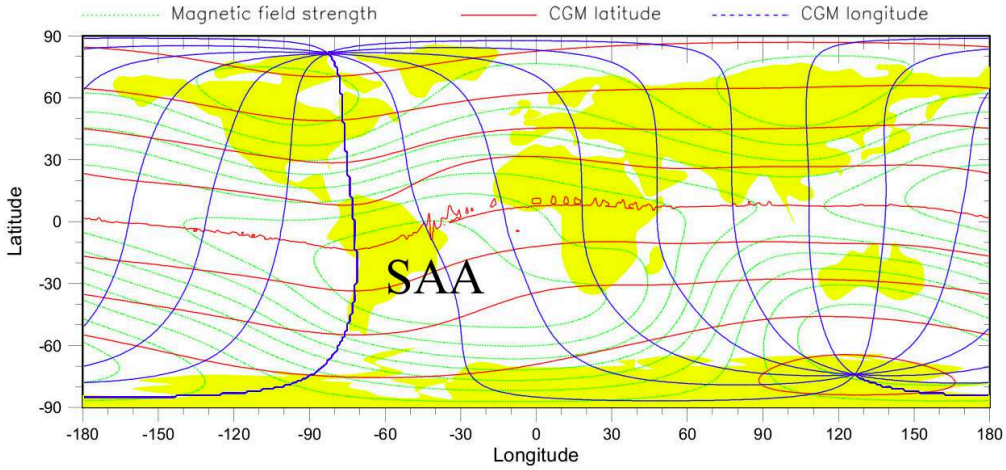

Figure 1.4: CGM coordinate grid projected on the geographic coordinate system. Magnetic field level curves are superimposed for reference. In the lowest magnetic field region the SAA is marked.

ity and incoming direction.
For a CR particle directed toward the Earth, the screening is determined by its rigidity, the detector location in the geomagnetic field and its incoming direction. Conversely, for given arrival direction and location, there will exist a minimum value of the particle rigidity R_C for which galactic CRs are allowed to penetrate the magnetosphere and be detected. In the dipole approximation, the rigidity cut-off R_C was analytically evaluated by Störmer [47] that found the relation:

$$R_c = \frac{M \cos^4 \lambda}{R_e^2 \left[1 + (1 \pm \cos^3 \lambda \cos \phi \sin \xi)^{\frac{1}{2}}\right]^2} \tag{1.6}$$

where M is the dipole moment. The arrival direction is defined by ξ and ϕ, respectively the polar angle from local zenith and the azimuthal angle counted clock-wise form local magnetic East. The $\pm$ sign applies to negatively/positively charged particles. The arrival location is defined by the geomagnetic coordinates (R_e,λ), a commonly used coordinate system relative to the dipole axis. R_e is the distance from the dipole center expressed in Earth radii units, and λ is the latitude along the dipole. These quantities come from the simple dipole field description, where the components of the field are:

$$B_r = -\frac{M}{r^3} 2 \sin \lambda \tag{1.7}$$

$$B_\lambda = \frac{M}{r^3} \cos \lambda \tag{1.8}$$

and the field lines have the form $r \propto \cos^2 \lambda$. For vertical incidence ($\xi = 0$) the azimuthal dependence of the cut-off simply vanished, putting in evidence the

cutoff behavior as a function of the geomagnetic latitude:

$$R_{VC} = \frac{M}{4R_e^2}\cos^4\lambda \equiv \frac{M_0}{R_e^2}\cos^4\lambda \tag{1.9}$$

where $M_0 = 15$ if R_{VC} is measured in GV . The cut-off is maximum at the geomagnetic equator, with a value of approximately 15 GV, and vanishes at the poles.
A more precise description of the cut-off can be obtained by replacing the dipole coordinates (GM) with the Corrected GeoMagnetic coordinates (CGM). The method consists in defining an opportune transformation GM $\leftrightarrow$ CGM that maps a more realistic geomagnetic field model into the dipole representation [30].
The most commonly used geomagnetic field model is the DGRF/IGRF one. In this picture, a rather complex magnetic field B is treated as the derivative of a scalar potential V, $B = -\nabla V$, with V expressed by a series of spherical harmonics [44]:

$$V = R_{\oplus}^{\pm}\sum_{n=0}^{\infty}\left(\frac{R_{\oplus}^{\pm}}{r}\right)^{n+1}\sum_{m=0}^{n}P_n^m(\cos\theta)(g_n^m\cos m\psi + h_n^m\sin m\psi) \tag{1.10}$$

where $R_{\oplus}^{\pm}$ is the mean earth radius (6321.2 km), r is the geocentric radius, θ is the geographic colatitude and ψ is the East longitude from Greenwich. $P_n^m(\cos\theta)$ are the Legendre polynomial functions, g_n^m and h_m^n are the Gaussian coefficients that specify the geomagnetic field, determined experimentally. The DGRF/IGRF model is widely used in geophysics and contains coefficients up to order 12. The dominant terms in Eq. 1.10 are related to $n = 1$ that leads to the simple dipole field.
By definition, the CGM coordinates (latitude, longitude) of a point in space are computed by tracing the DGRF/IGRF magnetic field line through the specified point to the dipole geomagnetic equator, then returning to the same altitude along the dipole field line and assigning the obtained dipole latitude and longitude as the CGM coordinates to the starting point. At the near-equatorial region, where the magnetic field lines may not reach the dipole equator and where, therefore, the standard definition of CGM coordinates is irrelevant, a different approach based on a B_{min} value along the given magnetic field line can be used. The procedure evaluates also a CGM altitude ($\sim$ distance from the center of the "effective" magnetic dipole). Using the CGM coordinates allows to use Störmer equations in a more realistic IGRF framework. A map of the CGM coordinates, valid for 1998, is shown in Fig. 1.4.

1.4 Cosmic Rays in the Atmosphere

As discussed in Sec. 1.2, the energy spectrum of CRs at Earth is influenced by the solar wind in the heliosphere and by geomagnetic field. Great portion of the CR spectra, however, is able to reach the Earth.
In addition, the Earth is surrounded by the atmosphere, which is essentially composed of nitrogen and oxygen atoms. The atmosphere extends for hundreds kilometers from the surface of the planet. Half of its mass is located within ~ 5 km

from the ground, where its column density is $\sim 1000\,\mathrm{g/cm^2}$. Its pressure decrease, following a power-law, with the increasing altitude above the see level. CRs that traverse the atmosphere are subject to destructive interactions with electrons and nuclei of the air and to energy losses due to ionization and radiative processes. Due to interactions, the CR composition changes dramatically during their propagation through the atmosphere: while above the atmosphere, protons and helium nuclei dominate the CR flux, the sea level flux is mostly composed by neutrinos and muons.

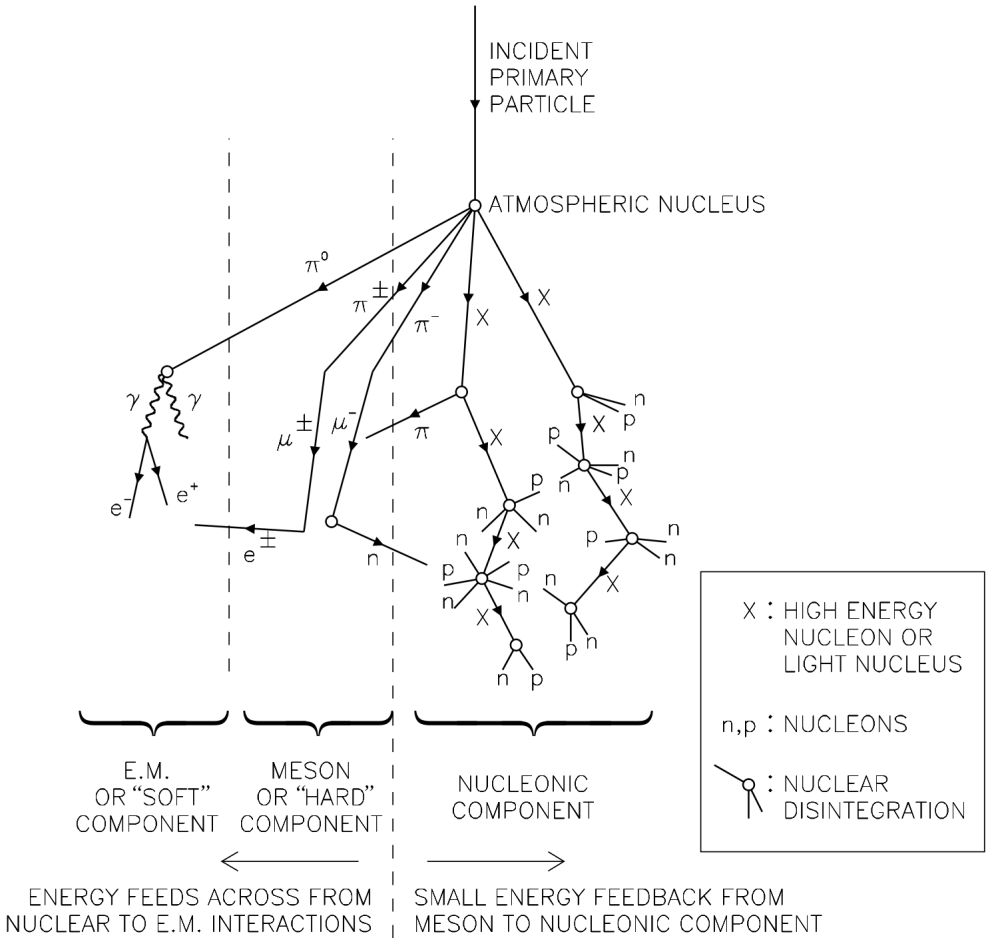

Figure 1.5: Schematic diagram of particle interactions in the atmosphere [17]. The diagram shows the *nucleonic component*, due to the fragmentation either of the incoming particle or of the target nucleus, the *hard component*, due to mesons decaying into muons, and the *soft component*, due to particles which interact electromagnetically. Neutrinos resulting from decays are not shown.

Galactic CRs that enter the atmosphere travel on average one *interaction length* before interacting. The interaction length, or mean free path, for a j-type CR nucleus in the air is given by

$$\Lambda_j = \frac{\rho}{\rho_j \sigma_j^{\mathrm{air}}} = \frac{A_j m_p}{\sigma_j^{\mathrm{air}}} \tag{1.11}$$

where ρ is the atmospheric density, ρ_j is the nucleon density, σ_j^{air} is the nucleon-air interaction cross section, A_j is the nucleus mass number and m_p is the nucleon mass. For CRs in the multi-GeV energy range, Λ is about 90 g/cm^2 for protons and 50 g/cm^2 for helium nuclei, which is a small number if compared to the atmospheric depth. The vertical intensity of the primary CRs can be expressed as:

$$\mathcal{N}(E, X) = \mathcal{N}(E, 0)e^{-X/\Lambda} \tag{1.12}$$

where X is the atmospheric depth or column density (given in g/cm^2) traversed by CRs since the "top" of the atmosphere ($\sim$ 100 km of altitude). From Eq. 1.12, it can be seen that almost none of the primary CRs will survive at the see level ($X \approx 1000$ g/cm^2).
Destructive interactions are always followed by a copious production of secondary particles. Some of the typical processes arising from such interactions are sketched in Fig. 1.5. The incoming CRs generate atmospheric particles that, by subsequent reactions or decays, develop a hadronic shower. The shower composition can be divided into three components: a *nucleonic component* containing nucleons or light nuclei created by CR spallation with the air nuclei, a *hard component* generated by the decay of mesons into muons, and a *soft component* which includes electromagnetically interacting photons and electrons. Neutrinos, not displayed in the figure, are also created in the decay of mesons and muons. Particles of the nucleonic component can further interact as long as they are energetic enough. They also experience energy losses due to ionization in the gas. Pions and kaons, which are the most abundant produced mesons, are usually present only in the higher layers of the atmosphere, because they are short-lived unstable particles ($\tau_{\pi^\pm} = 2.6{\cdot}10^{-8}$ s and $\tau_{K^\pm} = 1.2{\cdot}10^{-8}$ s). Thus, they rapidly decay into muons or neutrino as $\pi^+ \to \mu^+ + \nu_\mu$ and $K^+ \to \mu^+ + \nu_\mu$ and their associated anti-particles decay into μ^- and $\overline{\nu}_\mu$. The electromagnetic component originates essentially from the decay of neutral pions into photons, $\pi^0 \to \gamma\gamma$. Subsequent by pair creation processes and bremsstrahlung emissions develop an electromagnetic shower until the critical energy is reached.
The muons may decay as $\mu^+ \to e^+\nu_e\overline{\nu}_\mu$ and $\mu^- \to e^-\overline{\nu}_e\nu_\mu$. Their relatively large lifetime, $\tau_\mu = 2.2{\cdot}10^{-6}$ s, combined with the relativistic effect of time dilation and their fairly small interaction cross sections, make a large fraction of them able to reach the ground before disappear. As a result of these processes, the sea level flux is dominated by muons and neutrinos.

1.5 Atmospheric Muons

Atmospheric muons comprise a significant fraction of the cosmic ray flux at the sea level. Figure 1.6 shows the vertical fluxes of atmospheric muons above 1 GeV of energy as estimated by theoretical models. Estimates are compared with experimental data on negative muons.
The behavior which is expected on the basis of the processes outlined above is confirmed: the number of nucleons, which are the main components at high altitude, falls quickly as they interact with air. The peak in the intensity curve

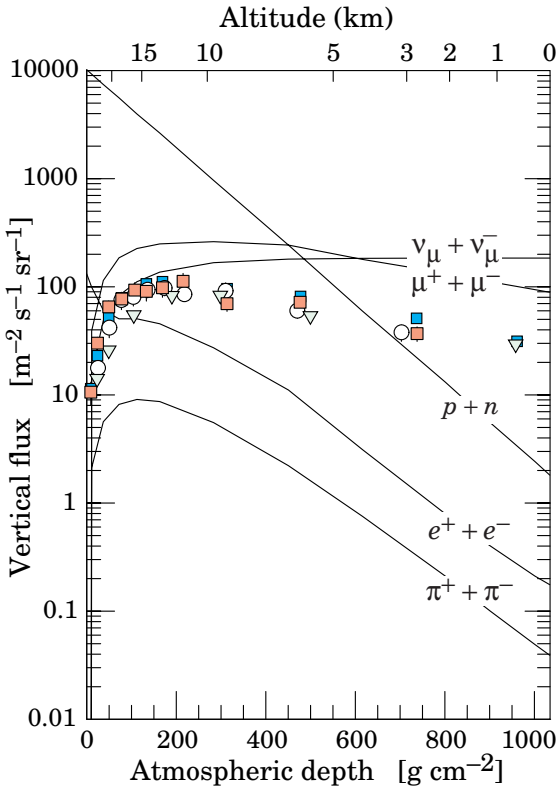

Figure 1.6: Vertical flux of CRs E> 1 GeV in the atmosphere as function of altitude. Negative muon data (markers) and theoretical calculations for different species (lines) are shown [35].

of pions around 15 km accounts for their production in the first interactions and for their subsequent decay. The muons, being produced by decaying mesons but having a longer lifetime, show a similar shape but with the maximum shifted towards lower altitudes; the number of neutrinos increases due to their negligible interaction cross sections. Primary electrons are enriched in the atmosphere by atmospheric secondaries (decay of charged and neutral mesons and mainly of muons) but their atmospheric spectrum falls quickly due to interactions. The integral vertical intensity of electrons plus positrons is very approximately 30, 6, and 0.2 m^{-1} s^{-1} sr^{-1} above 10, 100 and 1000 MeV. Above 1 GeV the integral vertical electrons/positrons flux is less than 3‰ of the muons one [35].
In summary, the most abundant charged particles which can be detected at the sea level, are muons, plus a small fraction of protons (about 1/100), and an even smaller fraction of electrons and positrons (about 1/1000).

A world survey of the present experimental situation of muon flux measurements at the sea level as a function of momentum is displayed in Fig. 1.7. The atmospheric muon spectrum at ground can be described, above few GeV of energy, by a power law distribution:

$$\frac{dN}{dE} \propto E^{-\alpha} \tag{1.13}$$

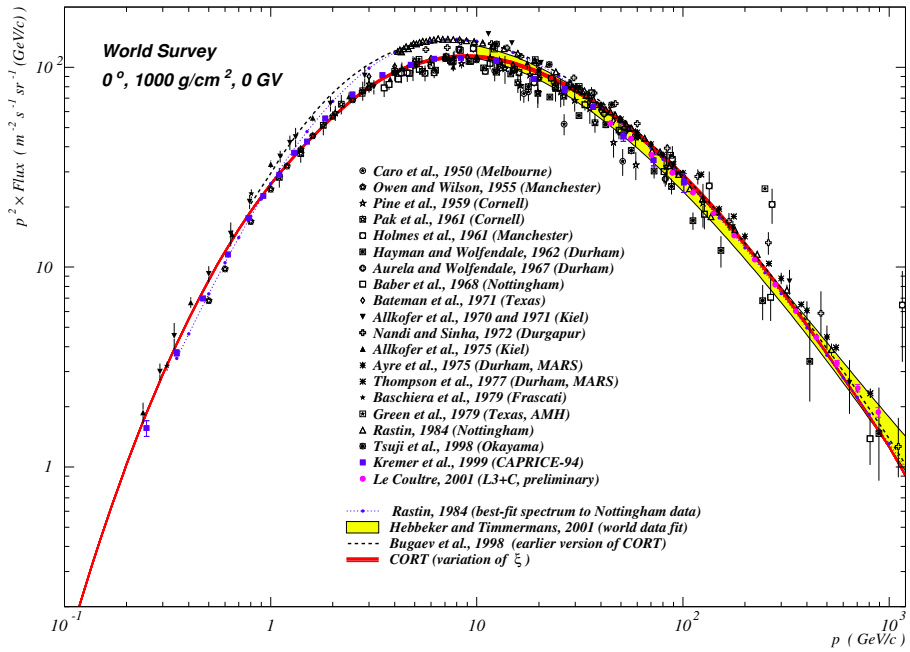

Figure 1.7: World survey of "vertical" muon differential measurements on ground. Fits on data and theoretical calculations are reported for comparison. The data are compiled in Ref. [43]. The spectrum is multiplied by p^{-2}.

where $\alpha \sim 3.7$, i.e., the muons spectrum is one power steeper than the primary CR spectrum. Below few GeV of energy the flux is almost flat, it steepens gradually to reflect the shape of the spectrum of primaries till about 100 GeV, and then it steepens further because of the decrease in the number of muons produced by decaying pions, which tend to interact rather than to decay at such high energies. For high energies ($E \gtrsim 100$ GeV) the spectrum can be calculated analytically [35]. The parametrization:

$$\frac{dN}{dE\,d\Omega} \approx \frac{0.14\,E^{-2.7}}{\mathrm{cm^2\,s\,sr\,GeV}} \times \left(\frac{1}{1 + \frac{1.1\,E\cos\theta}{115\,GeV}} + \frac{0.054}{1 + \frac{1.1E\cos\theta}{850\,GeV}} \right) \tag{1.14}$$

describes well both the energy and angular dependence of the muon flux at sea level. This equation accounts for the pion decays in the first term, and the kaon contribution in the second, while it neglects the charm contribution entirely, which is considered negligible in this context. Note that Eq. 1.14 is valid when the muon decay is negligible ($E > 100/\cos(\theta)$ GeV) and the curvature of the Earth can be neglected ($\theta < 70°$). Under such conditions, the angular distribution of the muon spectrum results $\propto \sec\theta$. At lower energies ($E \sim 3$ GeV) the muon spectrum exhibit a totally different angular distribution, i.e. $\propto \cos^2\theta$.

The ratio of positive to negative muons, the so-called *muon charge ratio*, μ^+/μ^-, is a significant quantity which reflects important features of the hadronic meson production in cosmic ray collisions and can help to discern the primary CR mass composition. From the discussion in Sect. 1.4, it is also apparent that the muon flux in the atmosphere is strongly related to the neutrino flux and that the muon

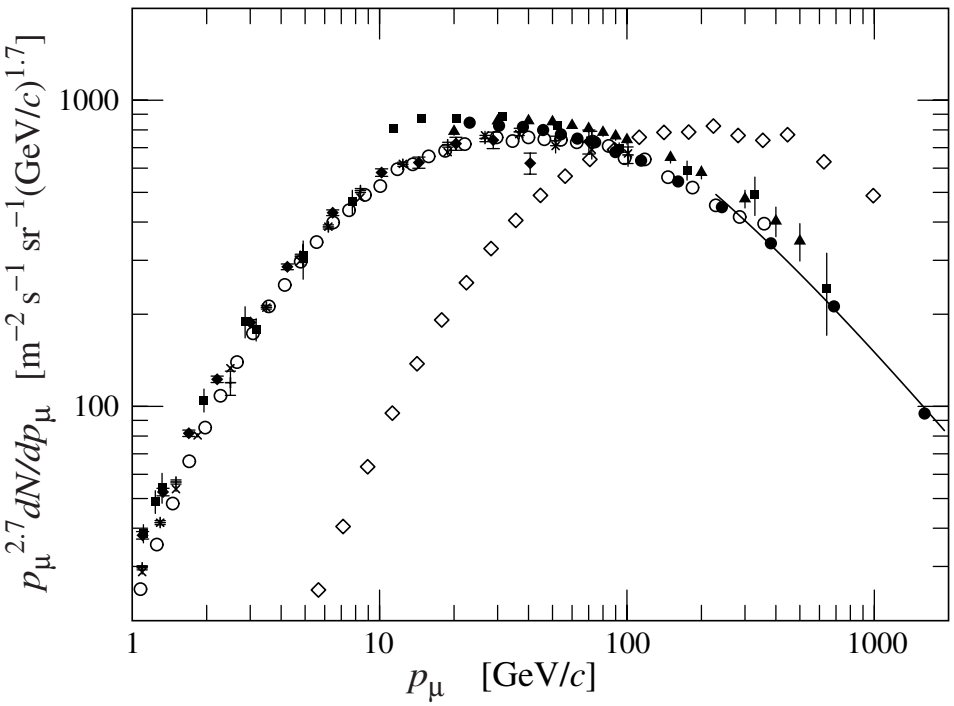

Figure 1.8: Spectrum of muons at $\theta = 0°$ (○, ●, ×, ♦, ▼, ▲, ■, +) and $\theta = 75°$ (◇). Theoretical line for "vertical" particles, from Eq. 1.14 is superimposed. The spectrum is multiplied by $p^{-2.7}$. The data are compiled in Ref. [35].

charge ratio, $\mu^+/\mu^- \sim \nu_e/\bar{\nu}_e$, may provide relevant information on the neutrino composition physics. The charge ratio μ^+/μ^- depends on the π^+/π^- and K^+/K^- hadronic production ratios, on the proton-to-neutron primary composition ratio, on the primary energy spectrum and atmospheric properties such as pressure or local magnetic field.
In typical nuclear collision, pions are produced like $p + p \rightarrow p + p + \pi^+ + \pi^+ + \pi^- + ...$, with the multiplicity dependent primarily on the *inelasticity* of the collision, i.e., on the fraction of primary nucleon energy available for the interaction. Since the protons are positively charged, and the amount of CR antiparticles is negligible, there are more positive than negative pions produced. In the nuclei constituting the air, there are roughly an equal number of neutrons as protons available. In galactic cosmic rays, nucleon are roughly 18% of the "all-nucleon" CR spectrum. The neutron-neutron collisions produce just as many positive pions as negatives and so pull the pion charge ratio, π^+/π^-, toward the value 1.0. Thus, among the nucleon-nucleon collisions ($p-p$, $p-n$, $n-n$), only 9% are of the type $n-n$ and produce equal numbers of π^+ and π^-, while the other 91% contribute to give an excess of π^+.

On the other hand, kaons require strangeness production. The kaon is more likely to be positive regardless of whether neutrons or protons are involved in the collision. A hadronic collision with enough energy for creating a strange-antistrange pair will preferentially put the strange quark into a baryon with two other quarks. In fact the collision starts with quarks rather than anti-quarks.

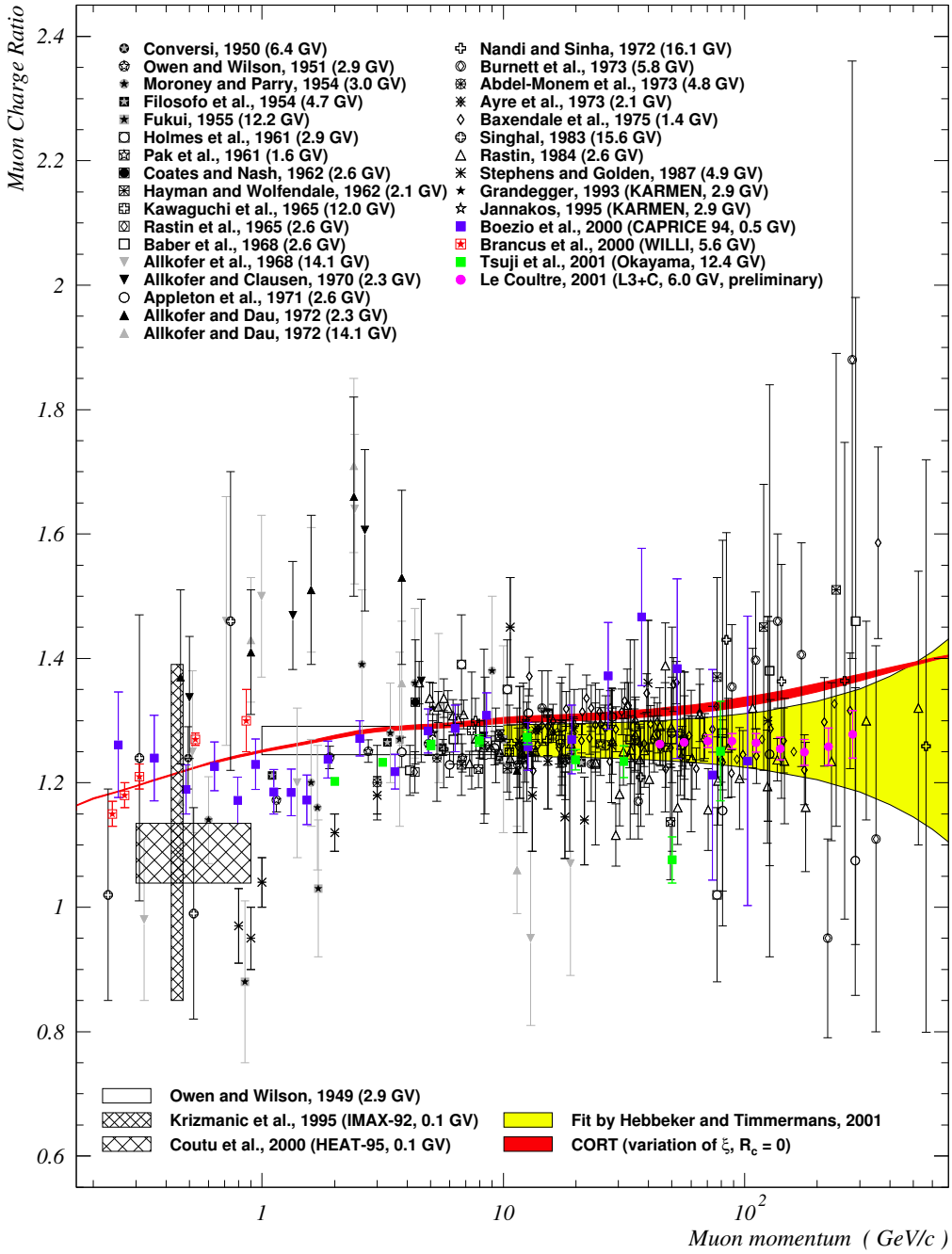

Figure 1.9: World survey of "vertical" muon charge ratio ($\mu+/\mu^-$) measurements on ground as function of momentum. The cut-off rigidity associated to each experiment is indicated. Fits on data and theoretical calculations are reported for comparison. The data are compiled in Ref. [43].

The antistrange would then likely either be paired with a *down* quark to make a neutral kaon or an *up* quark to make a positive kaon. This will tend to be true up to high enough energies where enough anti-matter can be created to make an antibaryon. Neutron-proton collisions have similar reaction channels, although the resultant meson charges produced are one third of the proton-proton

collisions [13].
All these considerations lead to a μ^+/μ^- ratio around the value ~ 1.3. The exact calculation of its energy dependence requires to model the complex secondary production chain, to give the the pion and kaon contributions. Contributions from semileptonic decay of charged and neutral kaons increases with energy and contributions from decay of charmed hadrons becomes important at higher energies. Furthermore, the proton-to-neutron ratio in the CR all-nucleon spectrum does not remain constant as a function of energy, and is expected to decrease with increasing energies.
Figure 1.9 shows the muon charge ratio μ^+/μ^- at the sea level as a function of momentum. The ratio appears to be nearly constant but large uncertainties are evident from the wide scattering of the data, in particular below some GeV where there is a systematic dependence on location, due to geomagnetic effects, and at high energies where statistics is poor. The excess of positively charged particles is due to the greater number of protons as compared to neutrons in primary cosmic rays, and so of π^+ with respect to π^- being produced in proton initiated interactions.

The study of the atmospheric muons on ground, flux and charge ratios, is of fundamental importance in calibrating the parameters of the hadronic models that describe the interactions of CRs in the atmosphere. Such studies are strongly connected with neutrino physics. In particular, since μ^+ and μ^- are produced in association with ν_μ and $\overline{\nu}_\mu$, and they can be revealed more easily than neutrinos, they represented a useful tool for understanding the so-called "atmospheric neutrino anomaly". The low number of measured muon neutrinos in the atmosphere, with respect to predictions, was among the proofs supporting the existence of neutrino oscillations. The accurate knowledge of the muon flux on ground, in conjunctions with the knowledge of primaries spectra outside the atmosphere, is crucial for tuning and checking the algorithms used to simulate the hadronic interactions of CRs in the atmospheric medium. Popular algorithms are `QGSJET` and `SYBILL` [45, 10]. These algorithms are extensively used in many areas of the underground CR physics such as neutrino physics, dark matter search, protons decay or double neutrino-less β decay. Precise knowledge of the muon flux allows to estimate the muon or muon-induced background or to study the primary CR spectrum in indirect measurements at ground-based experiments, such as the Pierre Auger Observatory [51].

Chapter 2

The Alpha Magnetic Spectrometer

2.1 Introduction

The Alpha Magnetic Spectrometer is a large acceptance instrument conceived to perform accurate measurements of the cosmic radiation on board the International Space Station. The AMS detector has been designed and built taking advantages from the experience of the high energy particle physics experiments. A prototype version of the detector, AMS-01, successfully collected $\approx$ 100 Million trigger on board the Space Shuttle Discovery during the 10 days STS-91 mission in 1998, demonstrating the concept of a space-borne, large scale, particle physics detector [6]. In its final design, AMS-02 has an acceptance of $\approx 0.45\,\mathrm{m}^2\,\mathrm{sr}$ and has been successfully installed on May 19^{th} on the International Space Station. Requirements for a space-borne high energy physics experiment are extremely challenging. Several constraints in the AMS design have been imposed by the transport on the Space Shuttle - with acceleration up to $9\,g$ and vibrations up to 150 dB during the launch - and the long term operation on the ISS, in vacuum and at ambient temperatures varying in time between -80° C and 50° C. A weight limit of 7 tons, a maximum allowed power consumption of 2 kW and an average data transmission rate of 9 Mb per second have been the requirements imposed to the detector design. In the design and constructions of each sub-system prototypes have produced to both qualify the physics performances and the space safety compliance. All the electronic components have been certified against radiation damage and the electronic boards produced in engineering, qualification and flight models, tested against mechanical and thermal stress in vacuum. A Thermal test in vacuum of the whole AMS detector and calibration with particle beams have been performed to verify the whole system in space-like operating conditions and to calibrate its sub-detectors. [21].

In this chapter the principal constituents of AMS-02 are reviewed: the characteristics of the Data AcQuisition system (DAQ) and of the sub-detectors will be discussed, providing a detailed description of the Silicon Tracker. The physics capabilities of the experiment will be discussed at the end of the chapter.

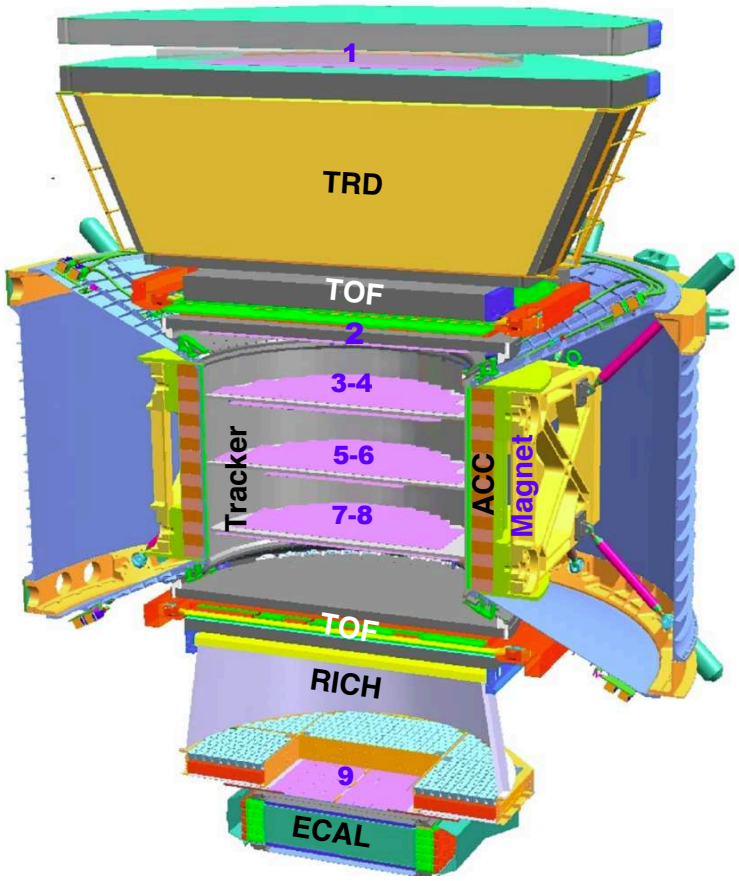

Figure 2.1: The AMS-02 detector

2.2 The detector

A schematic view of the AMS-02 instrument is shown in Figure 2.1. The core of the detector is the magnetic spectrometer: nine layers of double sided silicon microstrip detectors are used to reconstruct the trajectory of charged particles bent by the 0.15 T magnetic field provided by a permanent magnet. With a $\approx$ 10 µm position resolution on the bending coordinate, the TRACKER system is able to measure the charged particle rigidity in the GV - TV range. At both ends of the magnet two pairs of segmented scintillator planes are placed to measure the Time Of Flight (ToF) of the impinging particles and provide the main trigger of the experiment. An Anti-Coincidence scintillator Counter (ACC) system surrounds the TRACKER planes installed within the magnet volume: it provides the veto signal to the trigger in order to reject multi-particle events generated in the interaction of cosmic rays entering the detector through the sides.
The AMS-02 detector is completed by other three sub-detectors which provide redundant measurements of the particle charge magnitude and complete the particle identification: the Ring Image CHerenkov (RICH) detector dedicated to the precise measurement of the particle velocity and absolute charge magnitude; the Transition Radiation Detector (TRD) and the Electromagnetic CALorimeter (ECAL) to ensure an accurate separation between leptons and hadrons. The

ECAL allows to determine electron and photon energy at the % level providing also a dedicated trigger for photons.

2.2.1 The Magnet

The AMS-02 permanent magnet is designed to optimize the competing requirements of a large, powerful and uniform dipole magnetic field in a flight-qualified, relatively light-weighted system. The external field has been designed to be smaller than $2 \cdot 10^{-2}$ T to avoid torques on the Space Shuttle and on the International Space Station and to minimize unwanted interferences with the electronic devices [9].
The magnet is made of 6400 Nd-Fe-B blocks of sides $5 \times 5 \times 2.5\,\mathrm{cm}^3$. The blocks are arrayed in 100 circle shaped 64 elements layers (one layer is depicted in Fig. 2.2), constituting a cylinder of length 800 mm, inner radius $r_1 = 111.5$ cm and outer radius $r_2 = 129.9$ cm. The blocks are arranged to form 64 segments with varying field directions in order to produce a 0.15 T field intensity in the magnet center [6].
The magnetization vector resulting in the cylindrical shell is constant in magnitude and oriented according to:

$$\alpha = 2\phi + \pi/2 \tag{2.1}$$

being ϕ the angular cylindrical coordinate. Such a distribution gives an internal field of:

$$B = B_r \ln(r_1/r_2) \tag{2.2}$$

where B_r is the residual magnetic flux density of the ring and r_1/r_2 is the inner/outer radii ratio. The magnet fulfills the strict space requirements, as demonstrated in its first space flight in 1998 as constituent of the AMS-01 detector.
The orientation of the almost uniform magnetic field defines the whole reference frame of the AMS-02 experiment. The center of the frame is at the center of the magnet. The AMS-02 x axis is oriented along the direction of the field lines. The z axis is defined by the magnet cylinder symmetry axis, with positive values toward the top of the instruments. The last axis, y completes the cartesian right-handed tern (see Fig. 2.2). All the curved motion of a charged particle in the AMS-02 magnetic field is contained in the z-y plane.

2.2.2 The Silicon Tracker

The core of the AMS-02 apparatus is a micro-strip silicon tracker. The tracker is composed by 9 layers [41] arranged along the height of the AMS-02 detector, as shown in Fig. 2.4. Layers 1 and 9 constitute the *external* tracker and are positioned at both ends of the AMS-02 detector, above the TRD (z=155 cm) and the ECAL (z=-135 cm) respectively, to maximize the lever arm in the trajectory determination. In Fig.2.7 the external layers during the AMS-02 detector integration are shown. Layers 2 to 8 constitute the *inner* tracker and are arranged

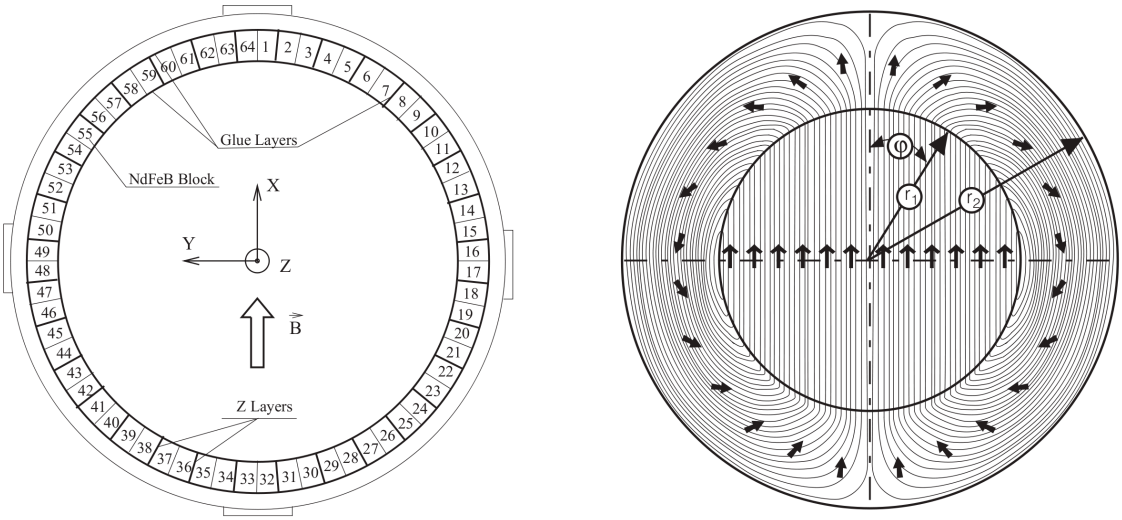

Figure 2.2: The AMS-02 magnet field orientation [6]. The varying direction of the magnetic field in the material allowed the flux to be returned primarily within the material allowing for a negligible external field. A quite uniform field is generated in the inner part of the volume. The magnet blocks and the coordinate system are shown in the left picture. The arrows in the right exhibit the magnetization direction α.

Figure 2.3: The AMS-02 permanent magnet that operated [6] on board of the Space Shuttle Discovery in 1998 (Mission STS-91 - Experiment AMS-01).

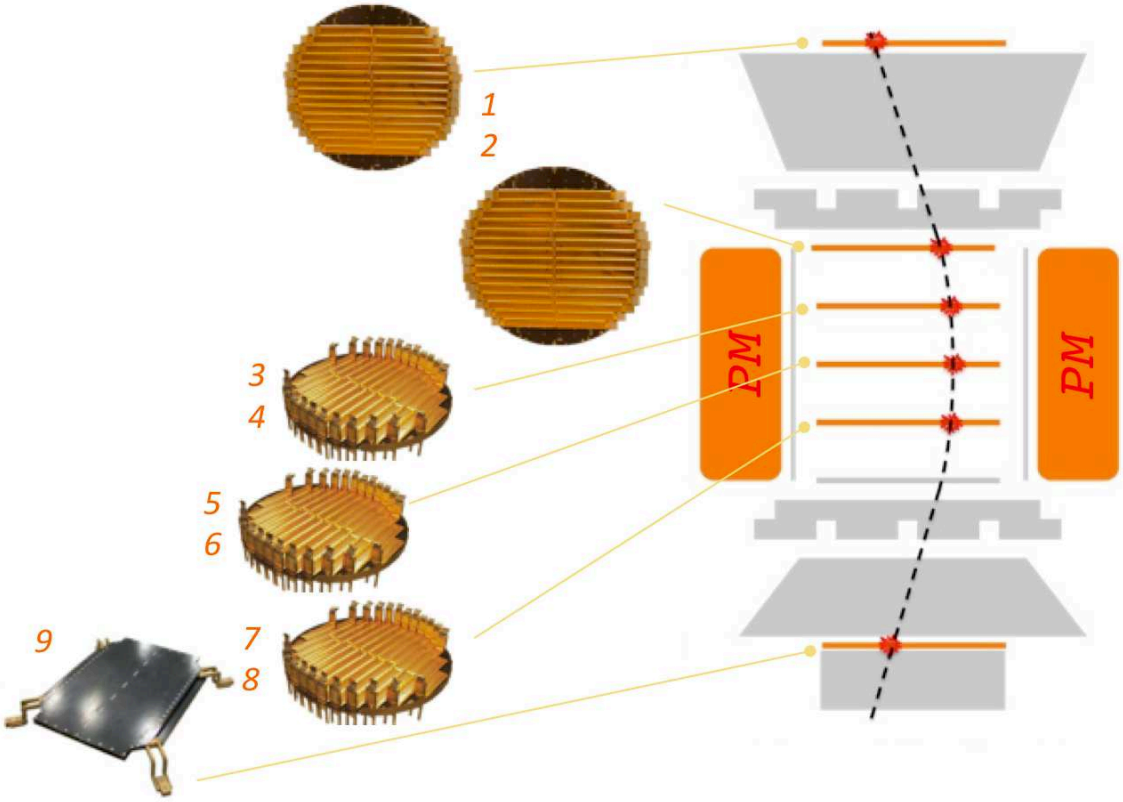

Figure 2.4: Sketch of the AMS-02 tracker layers configuration.

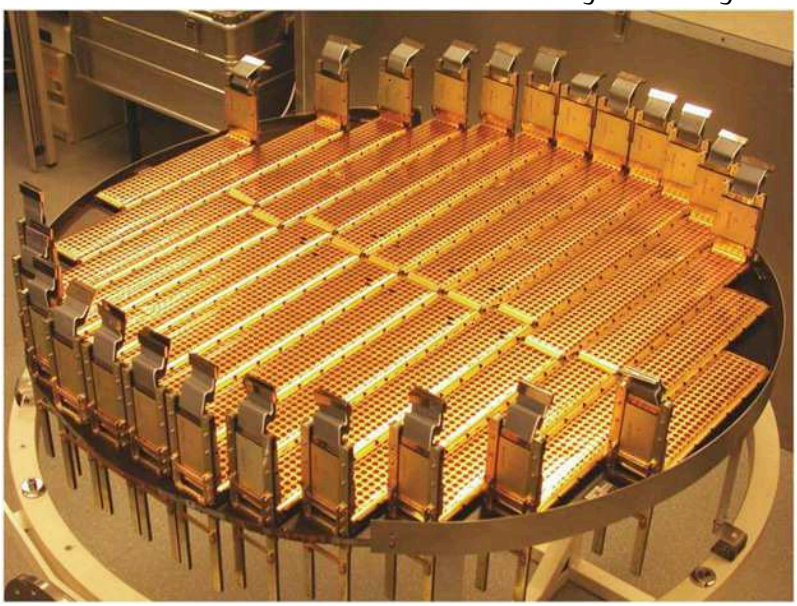

Figure 2.5: One of the internal tracker planes. On one of the two sides are visible the shielded silicon detectors installed with the front-end electronics in vertical.

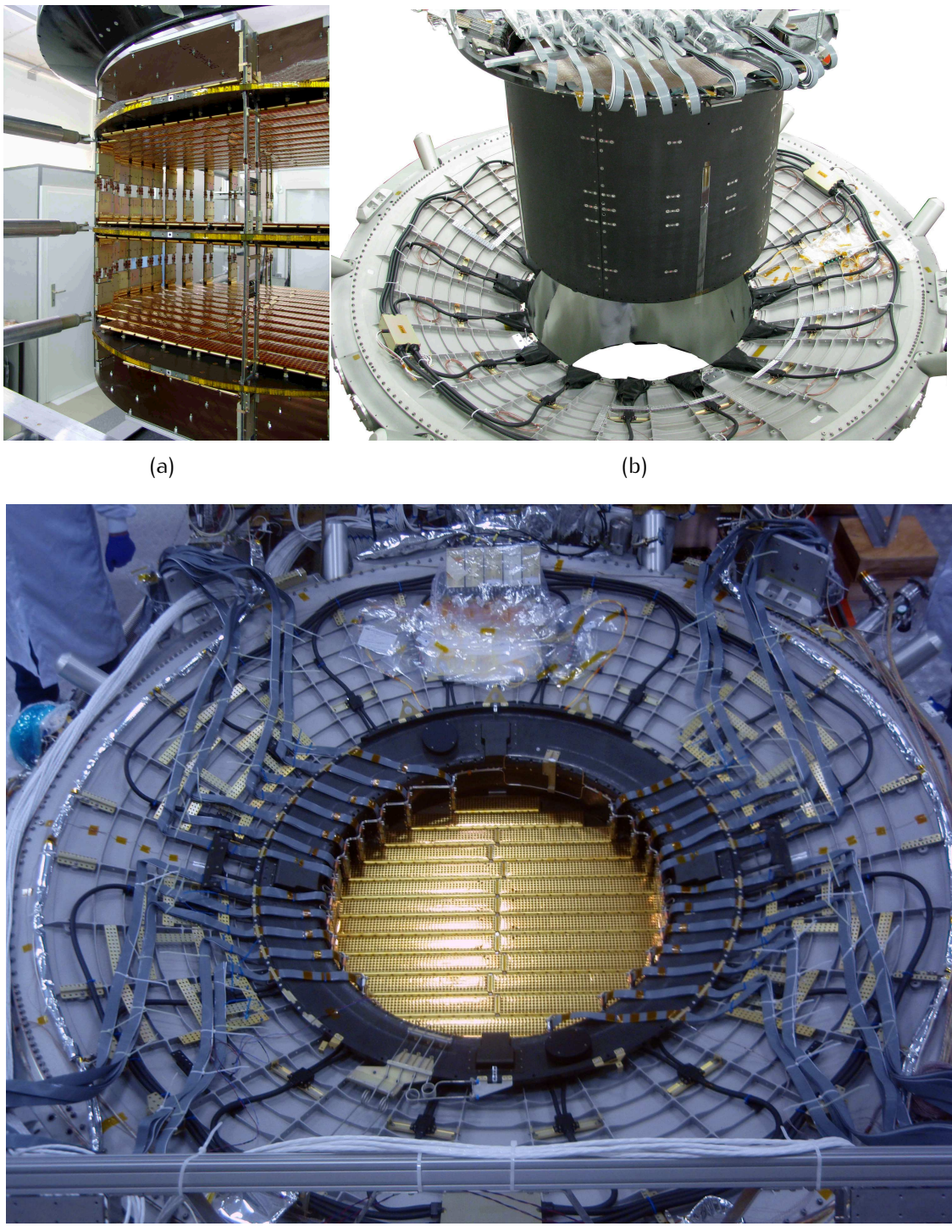

(a) (b)

(c)

Figure 2.6: The internal part of the AMS-02 Silicon Tracker. The three planes with coupled layers integrated together (a). The cylindrical carbon fiber support structure with the internal layers being lowered into the magnet case bore (b). The internal part of the tracker integrated and cabled (c).

(a) (b)

Figure 2.7: External layers of the AMS-02 Silicon Tracker. The layer 1 being lowered on top the TRD (a). The shielded silicon detectors are visible. The layer 9 integrated over the electromagnetic calorimeter (b). The Ring Imaging Čerenkov and the lower planes of the Time of Flight are being lowered over the silicon tracker layer.

just above the magnet mechanical structure (layer 2, z=55 cm) and inside the magnet bore (layers 3-8). Three carbon fiber and aluminum honeycomb planes (see Figs. 2.5 and 2.6) support the layer pairs inside the magnet bore (3-4, 5-6, 7-8), with a relative distance between layers belonging to the same plane of $\approx$ 4 cm along the z axis. The most inner plane (layers 5-6) is placed at the magnet center (z=0) and the two neighbours symmetrically disposed at z=$\pm$ 27 cm from the central one.
Each layer contains a variable number (around 20) of read-out units, called ladder. Each ladder has a variable number (from 7 to 15) of silicon sensors. The total active area of 6.4 m^2, for a total number of 2264 Silicon sensors arranged in 192 ladders, makes the AMS-02 Silicon Tracker the largest tracker for a magnetic spectrometer ever built for space applications [11].

2.2.2.1 The Silicon sensor

The basic element of the Silicon Tracker is a double-sided micro-strip sensor. Its size is 72.045 $\times$ 41.360 $\times$ 0.300 mm^3 (see Figs. 2.8 and 2.9). The thickness of the silicon (300 µm) as well as the choice of a double-side detector is made to minimize the material budget along the particles path and so the consequent multiple scattering.
The substrate is high resistivity n-type Si sensor made with a dynamic resistive coupling, as punch through and surface-through techniques. The sensors are inverse biased with an operating voltage of 80 V. On the two surfaces are placed p^+ strips, with a readout (implantation) pitch of 110 (27.5) µm, and n^+ strips (orthogonal to the previous ones) with a pitch of 104 (208) µm. The capacitive coupling net between the implanted strips and the analog readout of the strip signals allows to apply a center-of-gravity technique to achieve a 10(30)µm position measurement resolution on the junction(ohmic) side of the sensor for single

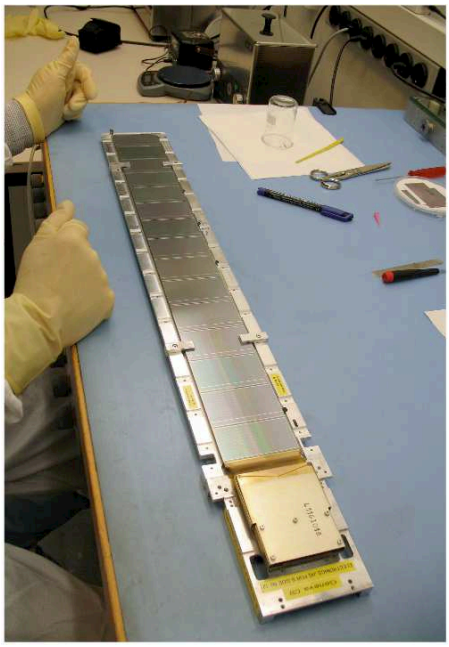

Figure 2.8: A 15 sensors ladder being assembled. The junction side is visible.

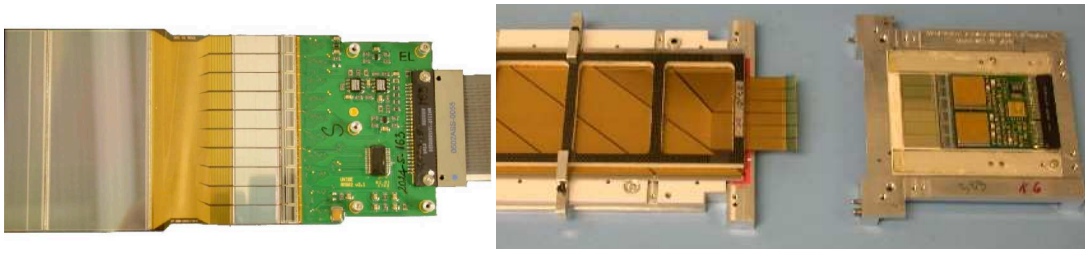

(a) (b)

Figure 2.9: The hybrids on the two sides of a AMS-02 Silicon Tracker ladder. On the left (a) the hybrid for the junction side of the micro-strip detector. The side is usually addressed as *S-side* (Silicon side), *p*-side (p^+ strips) or *y*-side. On the right (b) the hybrid for the ohmic side. The side is usually addressed as *K-side* (Kapton side), *n*-side (n^+ strips) or *x*-side.

charged particles. The junction side strips are used in AMS to measure the *y* coordinate in the bending (yz) plane of the particle trajectory.

2.2.2.2 The Ladder

A ladder is composed of an array of variable number of sensors (see Fig. 2.8), from 7 to 15, glued on a Upilex cable and mounted on an Airex support that confers the mechanical stability to the module. The ladder is protected from the light, a source of noise in the silicon substrate, and from the electromagnetic interferences by a Upilex metalized foil (see Fig. 2.10). The Upilex foil is separated from the silicon sensor surface by an Airex structure.
In order to maximize the layer acceptance and to minimize the number of readout channels the front end electronics is placed on the ladder end for both sensor

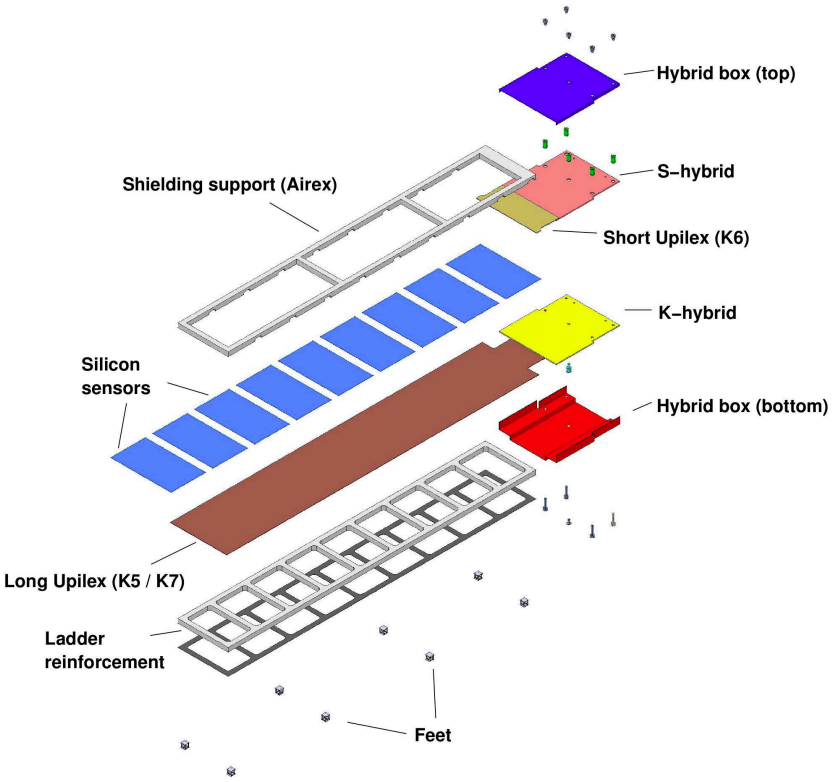

(a)

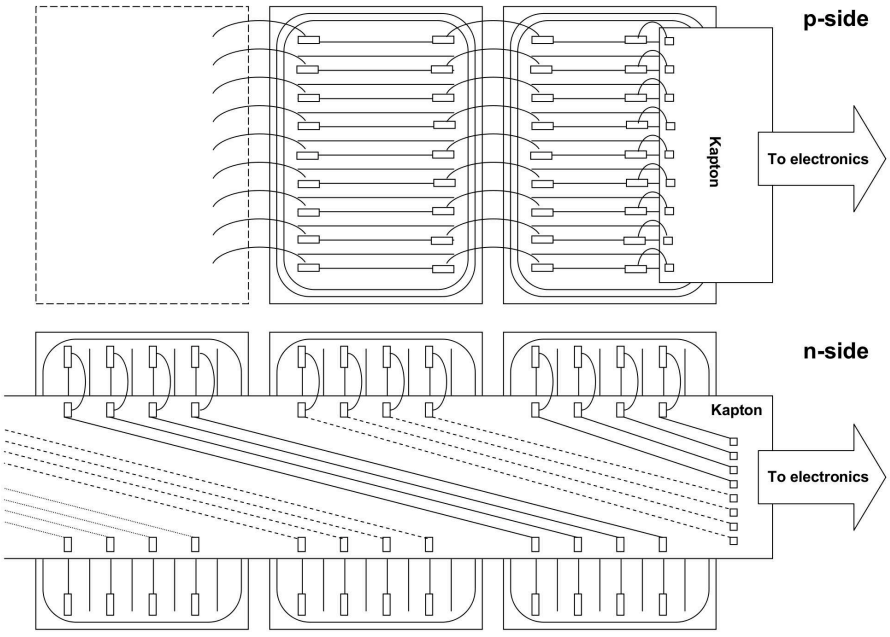

(b)

Figure 2.10: Exploded view of the ladder scheme (a). Detail of the bonding scheme of the readout strips (b); Even (odd) sensors, on the *n*-side, are coupled to decrease the numbers of readout channels.

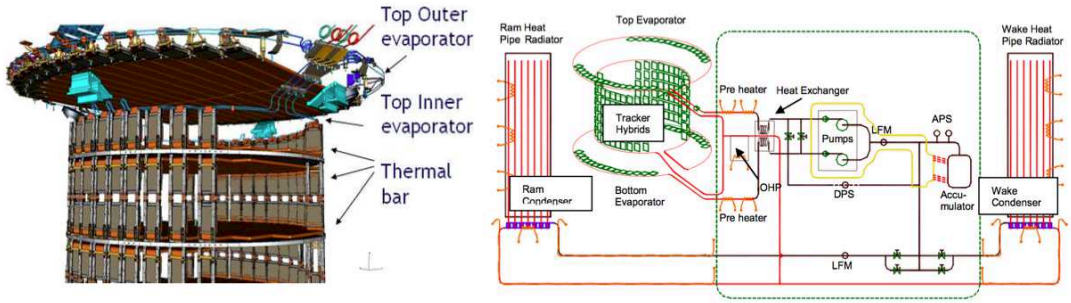

(a) (b)

Figure 2.11: The Tracker Thermal Control System. A CO_2 loop, working as evaporator for the TTCS system, exchanges heat with a thermal bars system connected to the ladder hybrids (a). The schematic of the whole TTCS system (b).

sides, with a bonding scheme of the sensors in a ladder as shown in Fig. 2.10(b). The 640 p^+ strips of each sensor of the same ladder are bonded to a short Upilex cable which brings the signal to the front end electronics hosted on PCBs (hybrids, see Fig. 2.9). The flexibility of the cable allows to place the electronics of the inner layers at an angle of 90° with respect to the tracker plane, allowing to maximize the active area within the magnet bore. To bring the n^+ strip signal to the electronics on the ladder edge, every i-th n^+ strip (for a total of 192) of even (odd) sensors is bonded on the same i-th channel of a long Upilex cable. The x coordinate is thus reconstructed with a multiplicity that can be solved only from the complete track knowledge.
All the 1024 (640 + 384) readout channels of a single ladder are AC coupled with 16 (10 + 6) high dynamic range Voltage Amplifiers (VA) trough 700 pF capacitors. The capacitors permit to suppress the high frequency components of the leakage current allowing a very low power consumption of less than 1 mW per channel. The signal passes trough a semi-Gaussian CR-RC shaper with a $\approx 5\,\mu s$ shaping time. Such a long shaping time allows a consistent reduction of noise. Then signal is sampled and sent to the Tracker Data Reduction board (see Sec. 2.2.9.1).

2.2.2.3 Tracker Thermal Control System (TTCS)

Tracker electronics, mainly the voltage amplifiers in the hybrids, develop $\approx 120\,W$ of heat that must be removed from the volume of the inner tracker to prevent overheating of the system: a maximum temperature of 80°C can be withstanded by the electronics before a permanent damage, however an optimal constant temperature of $\approx$ 20°C is desirable to keep uniform performance of the overall system.
A two phases CO_2 cooling system was designed and built to steal the heat from the hybrids and bring it outside the detector where it could be radiated toward the outer space.
As shown in Fig. 2.11, the ladder hybrids are thermally connected to a system of thermal bars to keep the whole tracker at the same temperature. A pump forces the liquid CO_2 into a loop passing trough the thermal bars, working as evaporator. In this evaporator the hybrids heat makes the CO_2 boiling and becoming

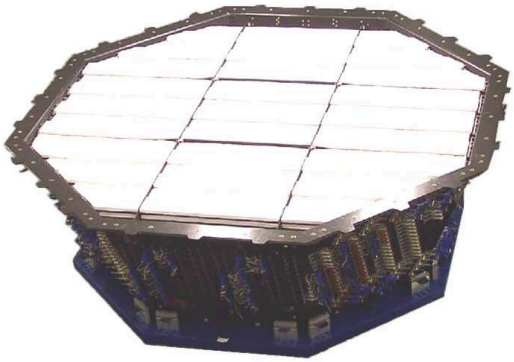

Figure 2.12: The truncated octagonal pyramid shape TRD integrated and ready to be installed on the whole AMS-02 detector.

two phases. Exiting from the tracker the two phases CO_2 is thermally connected to the liquid entering the evaporator, bringing the second as close as possible to the boiling point. After this step the two phases CO_2 goes toward a two radiators system, facing the outer space, working as condenser. A CO_2 accumulator works as *buffer* providing the correct dimensioning of the thermoidraulic device. The boiling of the liquid, and so the use of latency heat, makes the system more efficient with respect to a single phase device.
The whole TTCS system (loop, pumps, accumulators, etc...) is completely doubled to have fully redundancy.
The layer 1, facing almost directly the outer space, has no over-heating problem and doesn't need a cooling system.

2.2.2.4 Tracker Alignment System (TAS)

Laser diodes are installed on the layer 2 support structure. Five laser beams permit to monitor the mechanical movements of the 7 layers of the internal tracker. To minimize absorption and reflection of the laser beams, special windows have been implemented on the shielding of 20 ladders along their path, the corresponding sensors have been produced with a reduced strip metallization width and their surface treated with an anti-reflective coating.

2.2.3 The Transition Radiation Detector (TRD)

On the top of the instrument, just below the first layer of the Silicon Tracker, a Transition Radiation Detector is used to identify electrons and positrons within the overwhelming background of protons and nuclei.
The AMS TRD has truncated octagonal pyramidal shape (see Fig. 2.12) and is divided in 20 layers along the vertical (z) coordinate. Each layer is made by 20 mm irregular polypropylene/polyethylene 10 µm fiber fleece as radiator and Xe/Co_2 filled proportional wire straw tubes. The straws are made of double layer aluminized kapton foils with an inner diameter of 6 mm. A centered 30 µm gold plated tungsten wire is operated at $\approx$ 1300 V for a gas gain of 3000. The tubes

(a) (b)

Figure 2.13: The upper (a) and the lower (b) part of the ToF system. The PMT inclinations and directions are designed to minimize the effect of the magnetic field.

are arranged in modules of 16 straws for a total of 328 units that cover an area of $2 \times 2\,m^2$ [52]. Using a likelihood selection to combine the 20 measurements of the transition radiation emitted by the ultra-relativistic electron/positron component it possible to obtain a proton/electron rejection at the level of 10^2-10^3 with an efficiency for electrons at the level of 90% up to few hundred GVs. The energy deposition due to minimum ionizing nuclei can also be used to infer the magnitude of their charge up to carbon.
The TRD has also tracking capabilities with a resolution at the mm level. The tubes in the 12 central TRD layers are oriented along the y axis to provide a coarse reconstruction of the particle trajectory in the non bending plane and contribute to solve the ambiguity arising from the bonding scheme in the tracker. The tubes in the first and last four layers of the detector are oriented along the x axis, sampling the particle trajectory in the bending direction between the inner tracker and the upmost layer of the external tracker.

2.2.4 The Time Of Flight (ToF)

Scintillations counters are placed at both ends of the inner tracker to measure the time of flight (i.e. the particle velocity) and to provide a trigger for the whole experiment.
The ToF system [15] is composed by four planes of segmented scintillators disposed in pairs above (Upper TOF) and below (Lower TOF) the magnet (see Fig. 2.13).
The four planes contain, from the top to bottom, 8, 8, 10 and 8 scintillator paddles. Each counter is made by 1 cm thick polyvinyl-toluene scintillators of trapezoidal (18.5-26.9×117-$134\,cm^2$) or rectangular (12×117-$134\,cm^2$) shape. Each end is coupled by means of plexiglass guides either to 3 (trapezoidal) or 2 (rectangular) photo-multiplier (PMTs). The paddles are alternatively positioned along x and y to provide a bi-dimensional measurement with a granularity of $12 \times 12\,cm^2$. To ensure full geometrical coverage in the trigger, adjacent paddles are partially overlapping providing a better position measurement (≈ 1 cm) in that TOF region. Since the PMTs have to work very close to the magnet, where the residual mag-

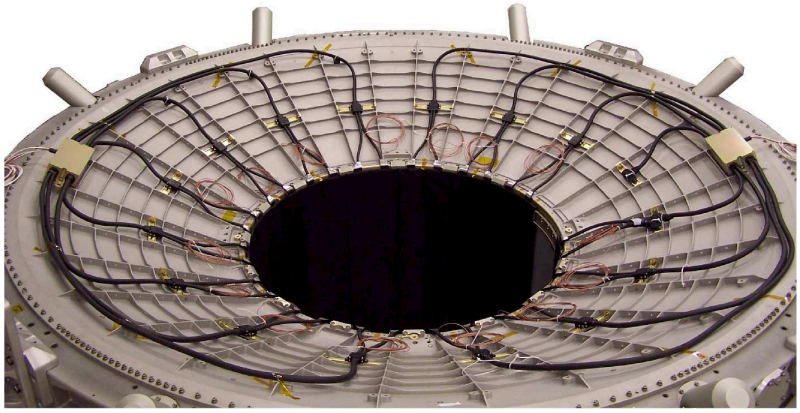

Figure 2.14: The upper conical flange of the case containing the magnet and in which the inner tracker is installed. The signals from the 16 scintillators panels, arranged on the cylindrical shape of the case, to surround the inner tracker, are guided outside the volume by wavelength shifter fibers. The signals are read by 8 PMTs for each side of the case (to provide redundancy).

netic field is not negligible, a particular class of PMTs was chosen. The *fine mesh* PMTs, with a compact dynodes structure and operating at high voltages ($\approx$ 1600 V) guarantee the reduction of the effect of the magnetic field on the electrons multiplication. The magnetic field effect is, additionally, decreased optimizing the angle between the PMTs and the magnetic force lines (see Fig. 2.13).
A low threshold (called *LT*) signal (i.e. very fast and only weakly function of the shape of the rising signal) is used for the velocity measurement. From the time difference between the two ends of the same paddle is possible to determine the impact point along the panel. The timing resolution of the ToF is $\approx$ 180 ps for Z=1 particles and $\approx$ 100 ps for Z$\geq$2. The resulting resolution on velocity β is $\sigma_\beta/\beta \approx 4\%$ (at β =1) for Z=1 and $\approx$ 1% for ions. This time-of-flight resolution gives a distinction power between upward-going and downward-going nuclei $> 10^{10}$. This is an important requirement for the anti-matter search.
A high threshold (called *HT*) signal from the ToF paddles is inserted into the Level-1 trigger logic and the coincidence of the signals from the various planes gives the charged particles trigger for the whole experiment (see Sec. 2.2.10).
Since the energy deposition in a scintillator counter scales with the charge of the incident charged particle ($\propto Z^2$), the ToF system is capable to give 4 independent charge measurements. A very high threshold (called *SHT*, super high threshold) signal ($\approx$ 1.5 times the signal given for a Minimum Ionizing Particle) is inserted into the Level-1 logic to permit a different trigger condition in case of nuclei (see Sec. 2.2.10).

2.2.5 The Anti-Coincidence Counter (ACC)

The inner tracker is surrounded by 16 scintillators panels (dimensions: 220 $\times$ 830 $\times$ 8 mm^3) inserted in the internal bore of the magnet. The light coming from both ends of each scintillator is collected by wavelength shifter fibers of 1 mm

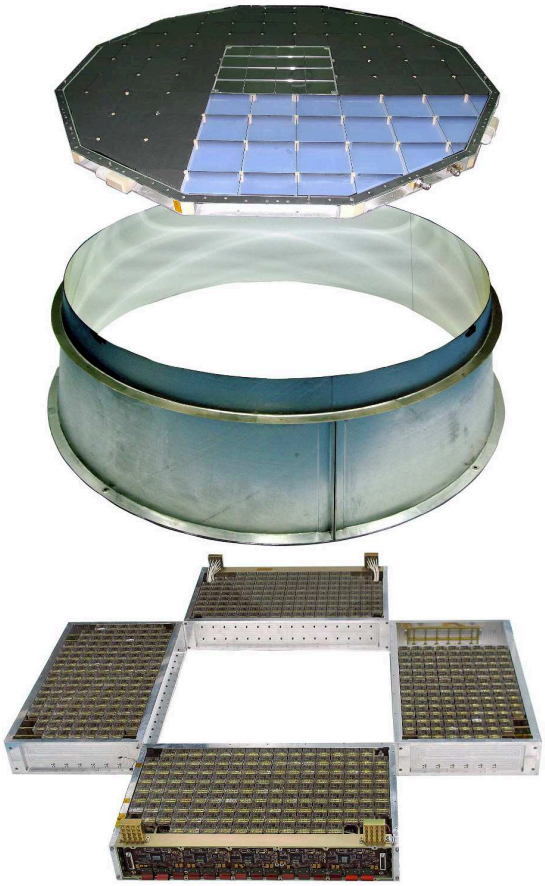

Figure 2.15: Exploded view of the RICH system. The radiators layer, the conical mirror and the detection plane are shown.

diameter, embedded in grooves milled into the scintillation panels. The fibers are arranged in bunches of 37 fibers and brought outside the magnet bore where are read by 16 PMTs (8 in the upper part of the magnet and 8 in the lower, see Fig. 2.14, to provide redundancy), similar to the ones used for ToF. The system is designed to have a very low inefficiency (below 1/300.000) and the high degree of homogeneity of the scintillating fibers ensures a reliable and fast signal for the high inclination particles with also some impact point determination capabilities [18]. The signals from the 8 segments of the ACC system are inserted into the Level-1 trigger logic (see Sec. 2.2.10).

2.2.6 The Ring Imaging Čerenkov (RICH)

A velocity measurement at the per-mille level is mandatory to perform the particle mass measurement needed to remove the low energy background (pions) generated in the interactions with the detector material and to measure the light nuclei isotopic composition. To improve the mass measurement capabilities, a Ring Imaging Čerenkov is inserted just below the lower ToF to system.
The RICH has a truncated conical shape (see Fig. 2.15) with a top radius of 60 cm,

Figure 2.16: The ECAL before the PMTs installation on the lateral slots (visible on the detector sides).

a bottom radius of 67 cm, and a total height of 60.5 cm. The system has a radiator plane, a $\approx$ 47 cm high expansion volume and a detection plane made of 680 multi-pixelized PMTs. To avoid extra-material in front of the calorimeter, the detection plane has a central hole matching the calorimeter shape and dimensions. The radiator plane is made of silica aerogel (n = 1.05) tiles with a thickness of 2.5 cm substituted with sodium fluoride (NaF) crystals (n = 1.334), 0.5 cm thick in the central region to maximize the Čerenkov light collection above the hole. The NaF radiator, furthermore, extends the velocity measurement range. The detector is completed by a conical mirror surrounding the expansion volume, improving the detection efficiency of 33%.
The system has a resolution $\sigma_\beta/\beta = 1.4 \cdot 10^{-3}$ for single charged particles and at the level of 10^{-4} for nuclei.
Furthermore the RICH system gives an independent measurement of the Z of the incident particle with a resolution of $\approx$ 0.3 charge units up to the iron region [8].

2.2.7 The Electromagnetic calorimeter (ECAL)

The ECAL, placed at the bottom of the AMS-02 detector, is a fine grained sampling calorimeter providing a tridimensional imaging of the longitudinal and lateral electromagnetic shower development. It has also tracking capabilities with an angular resolution of $\sim 1^\circ$ [20] .
Made of lead and scintillating fibers, the calorimeter is a square parallelepiped with a 65.8×65.8 cm^2 basis and a 16.5 cm height (see Fig. 2.16). It is divided into 9 superimposed *superlayers*. Each superlayer, 18.5 mm thick, consists of 11 grooved lead foils, 1 mm thick, interleaved with layers of 1 mm diameter scintillating fibers. In each superlayer fibers run along the same direction: the 3-D imaging capability is obtained by stacking superlayers with fibers alternatively parallel to Y-axis (4 layers, X-view) and X-axis (5 layers, Y view). The resulting composite structure has a lead-fiber-glue volume composition of 1:0.57:0.15 and an average density of 6.8 g/cm^3. Total calorimeter thickness corresponds to almost 18 radiations lengths. The high granularity permits a high rejection power between electrons and hadrons: each square element (9 mm side) corresponds to half Molière radius in traverse dimensions and one radiations length in depth. The fibers bring the signal outside the calorimeter volume where is read by 324 four anodes PMTS.

(a) (b)

Figure 2.17: StarTracker single camera: a CAD model (a) and a picture of the device installed on the conical flange of the magnet case (b).

The resolution for vertical particles was measured [23] with 6-250 GeV electron beams to be:

$$\frac{\sigma(E)}{E} = \frac{9.9\%}{\sqrt{E(\text{GeV})}} + 1.5\% \tag{2.3}$$

In combinations with the TRD, the ECAL makes possible a $\approx 10^6$ electrons/hadrons discrimination.
A fast recognition of possible showers is made by a dedicated board (*ETRG*) inserted in the Level-1 trigger logic (see Sec. 2.2.10). Being self-triggering, the ECAL can be used as a standalone detector (in particular for photons).

2.2.8 The Star Tracker

AMS-02 has two different γ-rays measurement possibilities. By the direct measurement with the ECAL, with a $\sim 1°$ pointing precision, and by conversion (i.e. a photon produces a e^+e^- pair on the upper part of AMS and the two charged particles are reconstructed by the tracker) with an angular expected resolution of $\sim$ µrad, at high energies.
To identify γ-rays sources, the AMS-02 orientation with respect to the fixed stars should be known with an angular resolution comparable to that achievable in the photon measurement in the detector [42]). AMS-02 has been equipped with a pair of CCD cameras which constitute the Star Tracker system. The 512 × 512 pixelized cameras are oriented at 40° (see Fig. 2.17) with respect the AMS-02 zenith and take pictures of the sky with a 10 hz rate. From the pattern recognition of groups of stars in the sky and the comparison with stellar maps is possible to determine the detector orientation in the sidereal reference frame with the required accuracy.

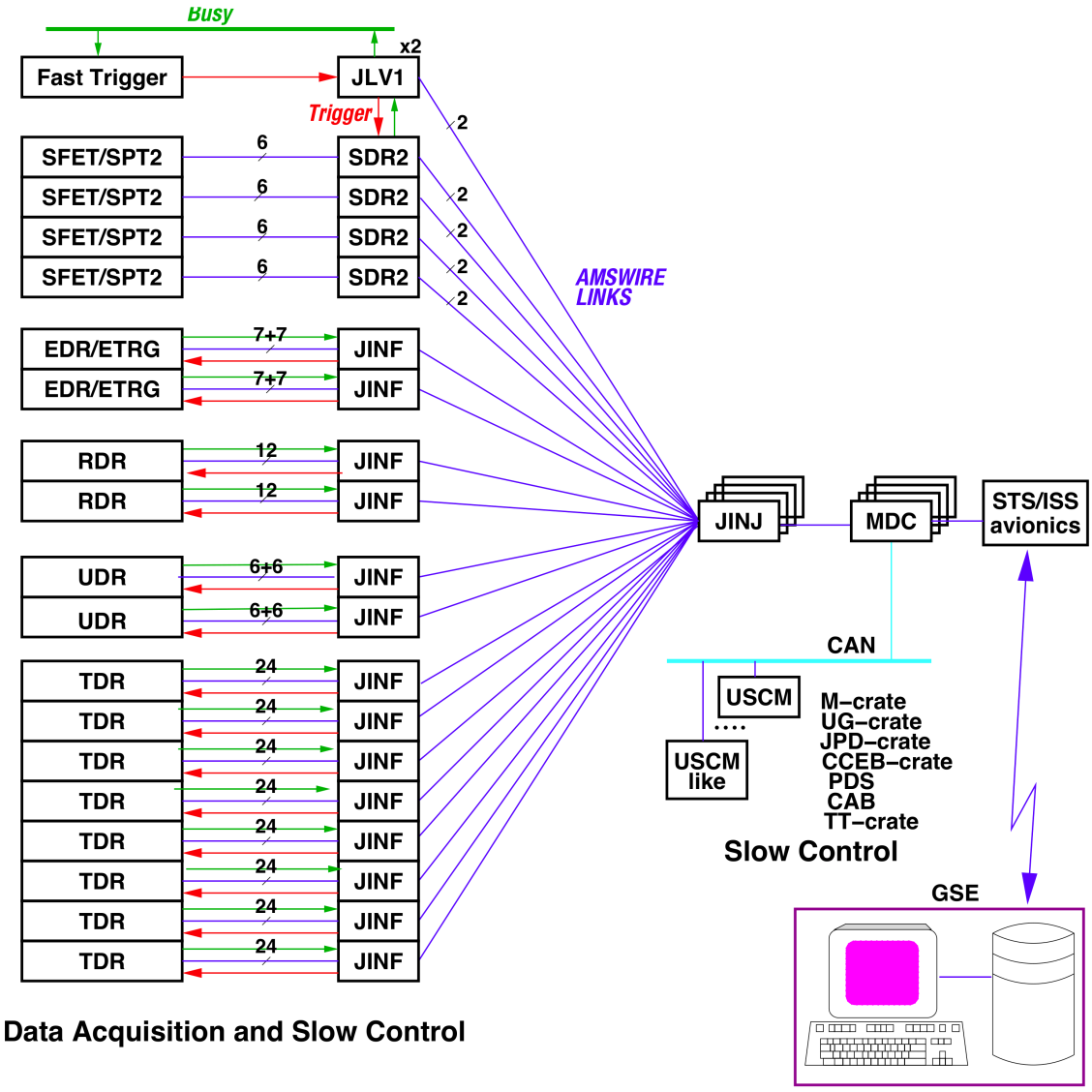

Figure 2.18: The AMS-02 DAQ block diagram. The DAQ has a tree-like structure with full redundancy.

2.2.9 The DAQ chain

AMS-2 Data Acquisition System collects data from over 200K analog channels of the various AMS-2 sub-detectors: TRD (abbrev. U, from german word *übergangsstrahlungsdetektor*, i.e. transition radiation detector), TOF and Anti-Coincidence Counters (abbrev. S, from scintillators), Tracker (abbrev. T), RICH (abbrev. R), Electromagnetic Calorimeter (abbrev. E) and Level-1 Trigger module (abbrev. LV1). It consists of nearly 300 computational nodes based on ADSP-2187L Digital Signal Processors (DSP) and a Main DAQ Computer based on PPC750 processor (JMDC) [37].
DAQ architecture has a tree-like structure (see Fig. 2.18):

- 264 xDR nodes (DR -Data Reduction, "x" specifies a sub-detector: T, U, R or E) collect data from analog electronics Front-Ends;

- 28 JINF nodes collect data from xDR nodes;
- 8 SDR nodes collect data from TOF/ACC and produce trigger signals and 2 JLV1 nodes collect analog and digital information to produce LV1 trigger;
- 4 JINJ collect data from JINF+SDR2+JLV1 nodes.

All the nodes (electronics boards) are hosted in two radiators (vertical panels on the two sides of AMS-02 in Fig. 2.22) to allow the exchange of heat with the outer space. The nodes are interconnected with point-to-point LVDS serial links and a dedicate protocol (AMSWire) is used for communication. The data throughput per link is 100 Mbits/s.
The software for the DSP is designed with a sub-detector independent framework where a set of detector dependent data processing routines are inserted. The general framework has the responsibility for:

- AMSWire protocol for communication between nodes;
- data protection based on CRC algorithm;
- event building routines for physics event assembly.

Beside the general framework common to all the nodes, specific procedures, to process the raw physics events and to monitor and configure the hardware status, are implemented in both xDR and JINF nodes.
The raw physics events are digitized and a compression (*zero-suppression*) is performed by the xDR nodes. With its $\sim$ 200k read-out channels the Silicon Tracker is the sub-detector where the more efficient compression is needed: the Tracker Data Reduction board (TDR) will be detailed below as xDR example.
The AMS experiment operates at input trigger rates up to 2 kHz with an average event size of about 2 KBytes. In order to minimize the dead time due to data processing, event buffering is used at every level of DAQ hierarchy (4 raw and 4 compressed for the xDRs, 4 for JINFs, 4 for JINJs and 2 in the JMDC).

2.2.9.1 Tracker Data Reduction board (TDR)

Signals from the 192 Tracker ladders are processed by 192 Tracker Data reduction (TDR) boards (shown on Fig. 2.19) grouped in 8 crates (T-Crate), each readout by a dedicated JINF. In each T-Crate, 2 boards (TBS) provide the bias to the silicon devices and 4 boards (TPFSE) provide all the power lines needed by the Front-End electronics hosted on the hybrids.
For each ladder a TDR:

- digitizes the strip signal,
- performs the calibration,
- performs the on-line data reduction (zero-suppression).

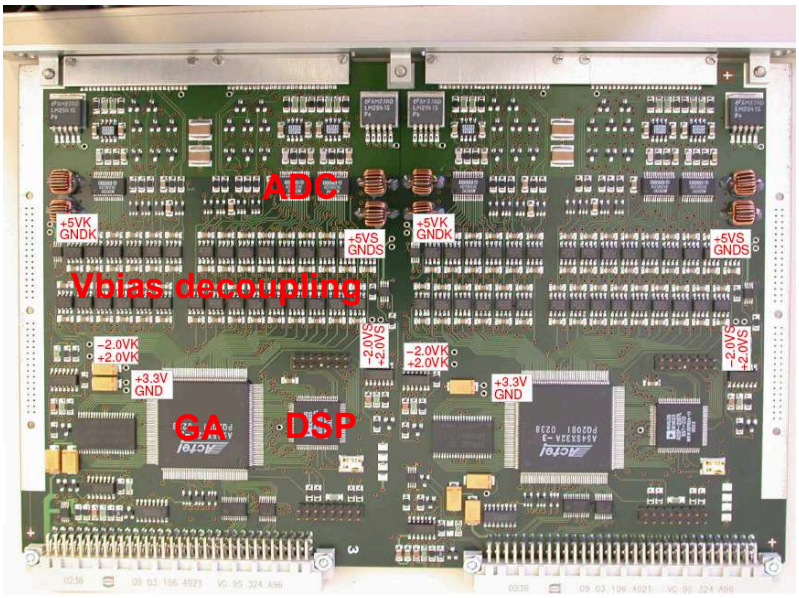

Figure 2.19: The Tracker Data Reduction board (TDR2). The board is divided into two sides (TDR) and is able to read two ladders. Each side is equipped with 3 ADCs and a Digital Signal Processor. An FPGA provides the command interface.

The analog signal is multiplexed into three streams and sent from the hybrid to three (2 for the *p*-side strips and 1 for the *n*-side) 12-bit ADCs that, in parallel, digitize it.
The signal amplitude registered by the ADC will be the sum of the pedestal (a bias characteristics of each channel), the noise (the gaussian fluctuation around the pedestal), the common noise (a noise common to all the channels of the same VA) and of the signal due to the ionization of an incident particle. Sampling some events in absence of ionization (random trigger) the TDR is able to measure the pedestal and the noise of each single readout channel. The mean and the RMS of the calibration events signals are computed by the DSP and the first is used as an estimation of the pedestal and the second of the noise.
A fast on-line data reduction is needed to avoid the transmission to ground of the values of amplitudes for the strips without a ionization signal [53]. The DSP removes the pedestal and the common noise (averaging the amplitudes of a whole VA) from the acquired signal and if the signal/noise ratio is greater than a fixed value the strip is considered as interested by a particle ionization. The candidate strip defines the *seed* for a *clustering* process. The seed and its neighbor strips having a signal/noise ratio greater than a pre-defined threshold are packed together in a *cluster* transmitted to the hierarchically higher DAQ node (JINF). Typical value of the signal/noise threshold to define the *seed* and the cluster channels are $\sim$ 4 ADC and $\sim$ 2 counts respectively, however these thresholds can be re-configured from ground control if higher compression factors are needed. A typical number of 20 clusters per event is found after zero-suppression, for an average size transmitted to ground equivalent to the information from $\sim$ 100 strips, considering the overhead needed for the packaging of the cluster information: this corresponds to a compression factor of $\approx$ 1000 when compared to the raw

readout of the 196608 channels in the whole tracker.

2.2.10 The Trigger

The trigger of the whole detector is built from signals coming from ToF, ACC and ECAL, inside a dedicated electronics board, the *JLV1* [40]. To generate a trigger in the LVL1 logic is necessary to latch the various input signals to get rid of the differences in their arrival times. Moreover there are some signals which need some pre-processing, as ECAL-A signals, which inhibit the readout of the corresponding electronics. The time needed to latch signals and to process them in the LVL1 logic results in a dead time of 1 µs. To minimize this dead time, a Fast Trigger (FT) technique is used: a loose trigger condition is first evaluated with a dedicated logic which does not introduce dead time in the system. Only if the Fast Trigger logic condition is satisfied, the LVL1 is activated and the acquisition inhibited during the 1 µs needed to take the trigger decision.

2.2.10.1 The Fast Trigger

Every 40 ns (25 MHz) the signals coming from ToF and ECAL are sampled and sent to fast and simple logics. The complete set of signals used in the Fast Trigger are detailed below.

The ToF produces six signals for each plane:

- `CP-(1...4)-p`: Charged Particle signal from *p*-side (positive side) of ToF plane (1...4). The signal is the *OR* of all the digital signals (i.e. above the HT) from the paddles (from 8 to 10) on one plane side. In normal conditions all ToF paddles are used in the OR, however specific configuration can be loaded in the logic for dedicated studies;

- `CP-(1...4)-n`: Charged Particle signal from *n*-side (negative side) of ToF plane (1...4). As above but for negative side;

- `CT-(1...4)-p`: Charged particle in Tracker acceptance signal from *p*-side (positive side) of ToF plane (1...4). Identical to the `CP` signal but only the paddles corresponding to the Tracker acceptance are normally used;

- `CT-(1...4)-n`: Charged particle in Tracker acceptance signal from *n*-side (negative side) of ToF plane (1...4). As above but for negative side;

- `BZ-TOF(1...4)-p`: Big Z signal from *p*-side of TOF plane (1...4). As the `CP` but with the digital signals produced using the SHT;

- `BZ-TOF(1...4)-n`: Big Z signal from *n*-side of TOF plane (1...4). As above but for negative side.

The *p* and *n* signals are combined in *OR* to generate a `CP`, a `CT` and a `BZ-TOF` for each plane:
The ECAL, instead, produces two signals:

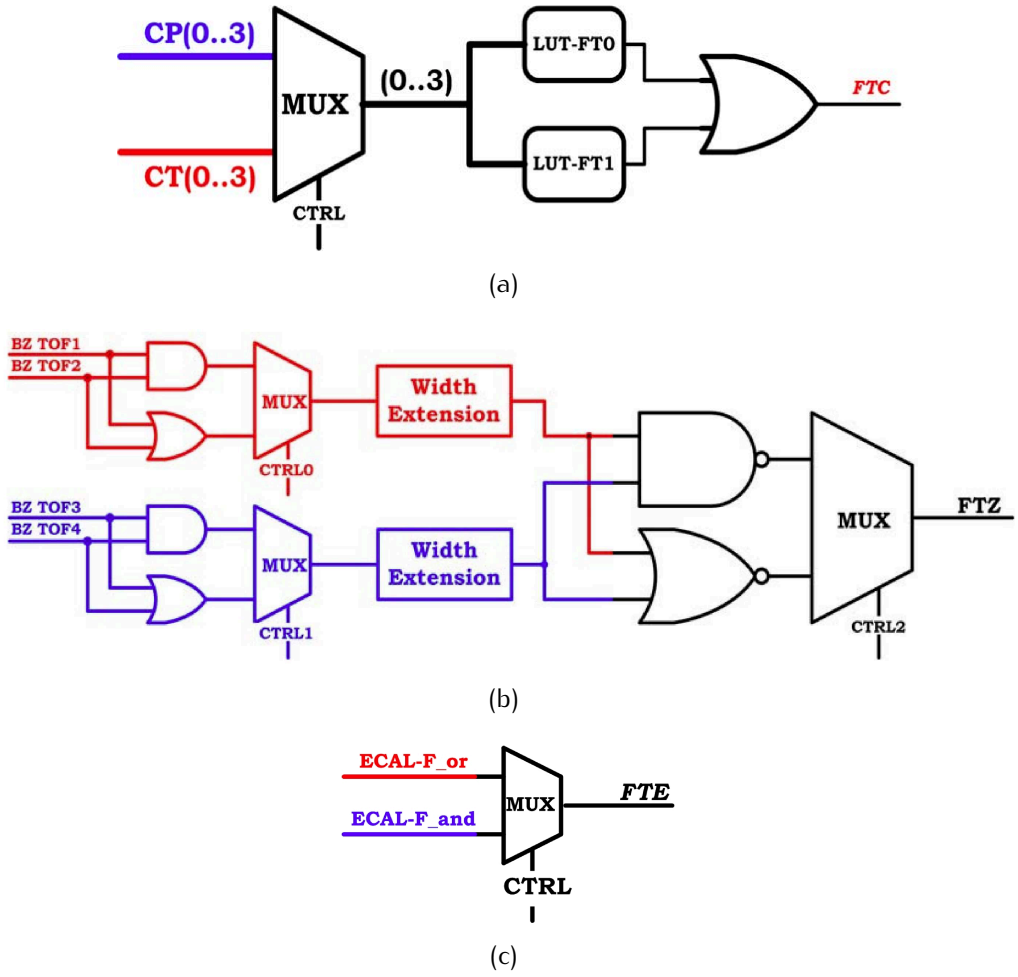

Figure 2.20: Schematic to generate the three FTs. (a) FTC from charged particle signals from TOF, (b) FTZ from big Z particle signals from TOF, (c) FTE from ECAL-F signals from ECAL.

- `ECAL-F-x`: ECAL Fast signal from *x* superlayers: a given number (typically 3) of near cells in the *x* view of the ECAL have a signal over threshold;
- `ECAL-F-y`: ECAL Fast signal from *y* superlayers: as above.

The signals from the two views are *OR*ed and *AND*ed giving `ECAL-F_or` and `ECAL-F_and` signals.

The signals described above are used to produce three different Fast Triggers:

- `FTC`: fast trigger for charged particle. CP and CT signals from the 4 planes are multiplexed and fed into two look-up tables (LUT-FT0 and LUT-FT1). If one of the 4 conditions is satisfied a Fast Trigger Charged (`FTC`) is generated (see Fig.2.20(a));
- `FTZ`: this fast trigger is meant to alert the system to trigger strangelets. The strangelet is a particle expected to have a high charge and to be very

slow, with respect to ions of the same charge and rigidity. This is because strangelets are expected to have an exotic m/z ratio ($\gg 2$, that is the typical ratio for ions). The BZ-TOF signals from the 2 top (bottom) planes are multiplexed. The two resulting signals, BZ-TOP and BZ-BOTTOM are extended up to 640 ns (slow particles) and multiplexed again. If the condition is satisfied a "strangelet" Fast Trigger (FTZ) signal is generated (see Fig.2.20(b));

- FTE: ECAL-F_and and ECAL-F_or are multiplexed to generate a Fast Trigger ECAL (FTE) signal (see Fig.2.20(c)).

The three FTs are *OR*ed to produce a general Fast Trigger signal. Up to the generation of the FT signal all the multiplexing, *OR*ing and *AND*ing are done continuously and no dead time is introduced.

Every time a Fast Trigger is produced, it is delivered to all the interested sub detectors[1] to allow the computation of specific quantities.

2.2.10.2 Level 1

After the generation of FT the JLV1 starts the LVL1 evaluation. This will take exactly 1 µs, independently from the result of the LVL1 evaluation and during this time the system will be busy. The signals produced after a FT, used in the Level 1 logic, are the following:

- Charged particle signals: these signals are used to build the charged particle trigger. After the FT a 240 ns gate is opened to latch charged particles signals, CP and CT. The latched signals are fed into look-up tables, LUT-FT0 and LUT-FT1, to produce signals, FTCP0, FTCP1, FTCT0 and FTCT1. The logic is similar to the one shown in Fig.2.20(a). The same CP and CT signals used above are latched till the end of the gate. The coincidence for FTCP0, FTCP1, FTCT0, FTCT1 is evaluated independently within the opened gate. For the flight the LUT-FT0 is set to accept events with 3 out of 4 TOF planes (meant for unbiased triggers) and LUT-FT1 to 4/4;

- Big Z signals: these signals are used to build the trigger for ions, allowing in the LVL1 logic to loose conditions on ACC with respect to the "standard" charged particle trigger. A 240 ns gate is opened to latch BZ-TOF signals. The latched signals are fed into a LUT, LUT-BZ, to produce a signal, BZ. For the flight the LUT-BZ is set to accept 4/4 events;

- ACC signals: these signals are used to veto triggers produced by particles passing out of the detector acceptance but inducing a trigger due to secondaries produced in the interactions with the materials. A 240 ns gate is opened to latch ACC signals. The latched signals are used to count number of ACC signals. This number is compared to two adjustable thresholds to

[1] The FT is delivered, for example, to the ECAL and the DSP of a dedicated board (ETRG), will search for an energy deposit in the cells of the calorimeter. A $\approx$ triangular (compatible with a shower) deposit is searched in both the views and if found a ECAL-A (ECAL Angular) is produced

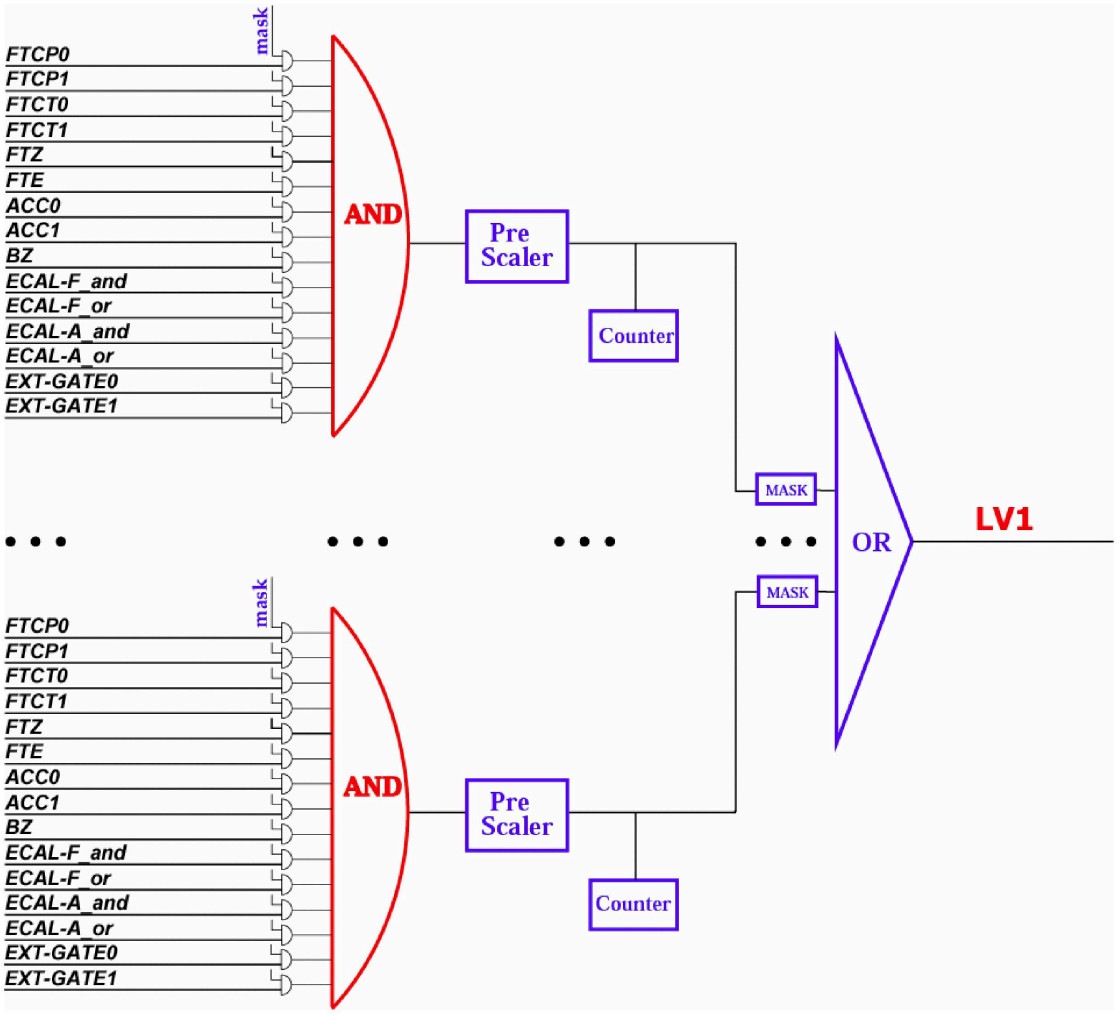

Figure 2.21: Schematic of the LVL1 logic. 15 signals are multiplexed to evaluate 8 different LVL1 sub-triggers that are *OR*ed to give the LVL1 to the experiment.

produce signals, `ACC0` and `ACC1`. For the flight the thresholds are set to 1 and 5. This gives a `ACC0` signal when the number of ACC fired is 0, and `ACC1` when is, at maximum, 4;

- `ECAL-F` signals: these signals are used to build the unbiased electromagnetic trigger. A 240 ns gate is opened to latch `ECAL-F` signals. The latched signals, `ECAL-F_or` and `ECAL- F_and`, are used in LV1 logic;

- `ECAL-A` signals (see footnote 1): these are used to build ECAL standalone triggers dedicated to non converting photons. A 640 ns gate is opened to latch `ECAL-A` signals. The latched signals, `ECAL-A_or` and `ECAL-A_and`, are used in LV1 logic;

- `EXT-GATE` signals: A 240 ns gate is opened to latch external gate signals. The latched signals, `EXT-GATE0` and `EXT-GATE1`, are used in LV1 logic. They are not used during flight.

The produced signals (plus FTE and FTZ), for a total of 15 signals, are multiplexed to evaluate 8 LVL1 sub-triggers under different conditions (see Fig. 2.21). Each sub-trigger can be pre-scaled (from 1:1 to 1:1024). The 8 sub-triggers are *OR*ed to give the LVL1 trigger to the experiment.

2.2.10.3 Flight trigger

For the flight, 7 sub-triggers were designed and implemented:

- Unbiased charged: TOF 3/4 (HT), pre-scaling factor 128. Is produced by the FTCP0;
- Single charged: TOF 4/4 (HT), N_{ACC}=0. Is produced by the coincidence of FTCT1 and ACC0;
- Normal ions: TOF 4/4 (SHT), N_{ACC}<5. Is produced by the coincidence of BZ and ACC1;
- Slow ions: TOF 4/4 (SHT), gate extended to 640 ns. Is produced by the FTZ;
- Electrons: TOF 4/4 (HT), ECAL signal over threshold on both views. Is produced by the coincidence of FTCT1 and ECAL-F_and;
- Photons: ECAL shower. Is produced by the ECAL-A_and;
- Unbiased EM: ECAL signal over threshold, pre-scaling factor 1024. Is produced by the ECAL-F_or;

2.2.10.4 The Live-Time scaler

For an absolute flux measurement is necessary to know the exact time the detector is ready to accept events. This time, called *exposure time*, is the fraction of the nominal data taking time to be evaluated taking into account the dead time of the system.
Possible dead time sources in AMS-02 are the following:

- Every time a FT is produced the system is busy for 1 µs till the end of the LVL1 decision. This is a fixed amount of time.
- Every time a LVL1 is produced and delivered to the subdetectors a finite amount of time will be needed by the front-end electronics for the signal digitization. This operation is carried in parallel for all sub-systems and introduces 200μs of dead time, which includes the 90μs needed for the digitization of the tracker signals and an additional delay introduced to optimize the noise performances in the detector.
- The compression of the events by the DSP, in xDRs, takes a variable amount of time ($\sim$ 300 µs). To reduce the corresponding dead time, up to four "raw" events can be buffered in the xDRs: compression of a given event can be then carried in parallel to the digitization of the following event. Dead time

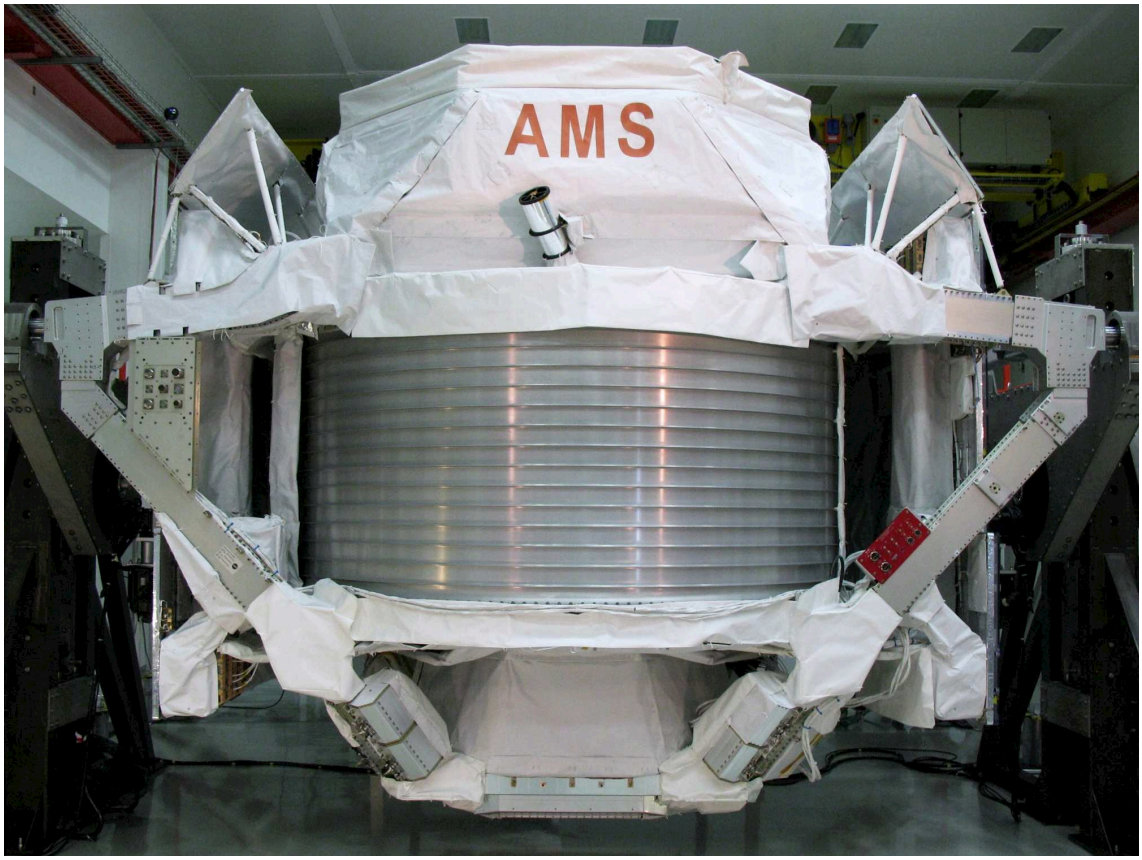

Figure 2.22: The AMS-02 completely integrated, at CERN on July 2010, ready to be shipped to KSC.

will be introduced only when the xDRs buffer is full: this is a source of variable dead time, usually depending on the DAQ rate.

A 20 ns fine scaler continuously samples the status of the DAQ within a time window of 2 seconds and counts the number of times the system was found ready to accept new events. The system *Live-Time* is defined as the ratio between the accumulated number of counts and the maximal number (10^8) in the sampling window. The exposure time is then evalutated by multiplying the raw acquisition time by the corresponding Live-Time.

2.3 Integration and data taking on the ground

The detector has been integrated (see Fig. 2.22) in its final configuration between the May and July 2010 in a dedicated clean room at CERN. In August 2010 a beam test with up to 400 GeV/c momentum protons, positrons, electrons and pions was performed in the SPS H8 beam line. The purposes of the test were:

- to check the alignment of the Silicon Tracker. AMS was moved and inclined on the 400 GeV/c momentum protons beam in more than 500 positions (see Fig. 2.23), allowing the study of alignment for all the combinations of ladders in the 9 layers;

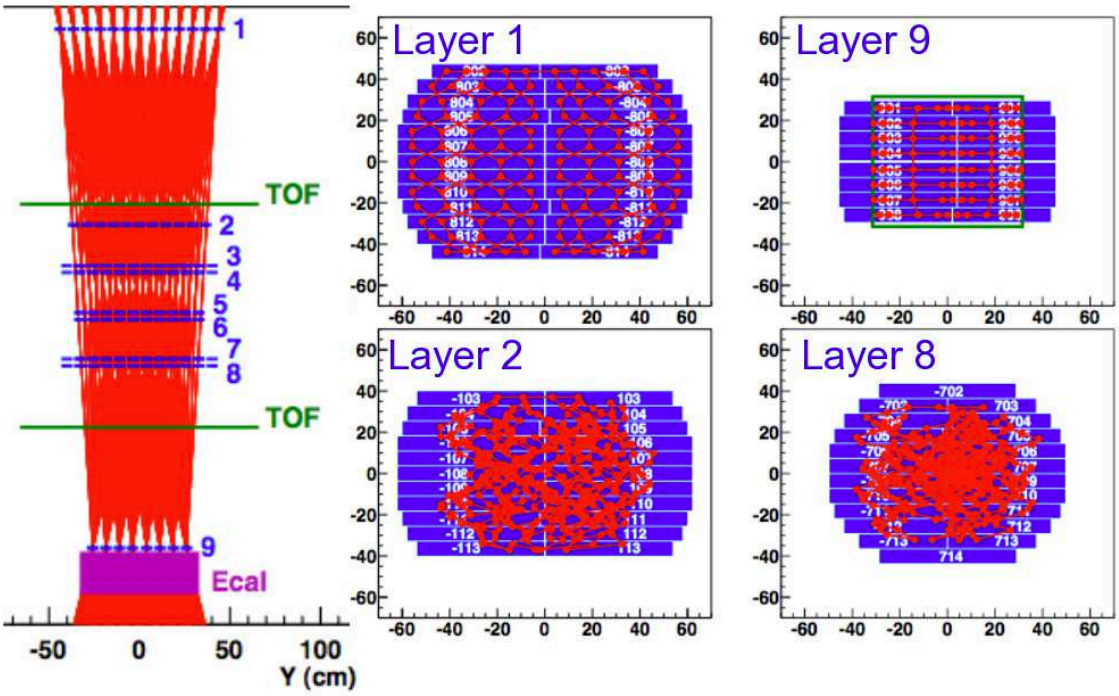

Figure 2.23: The beam positions explored in the August 2010 beam test. On the left a sketch of the beam positions in the $z-y$ view of the detector. The 9 layers of the tracker, the 4 planes of ToF and the ECAL are shown. On the right the beam positions as seen by the *external layers* (1 and 9) and by the more external layers of the *inner tracker* (2 and 8).

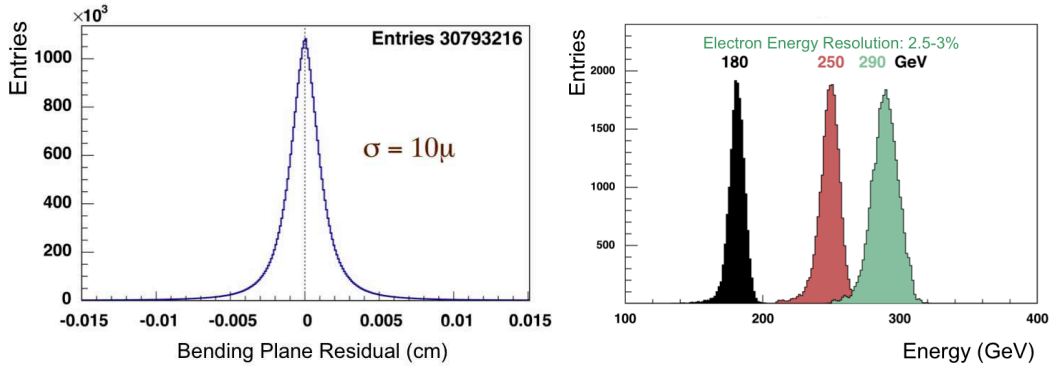

(a) (b)

Figure 2.24: Examples of the sub-detectors performances verified in the August 2010 beam test. (a) the spatial resolution of the Silicon Tracker on the bending direction. (b) the ECAL resolution for three different energy electrons beams.

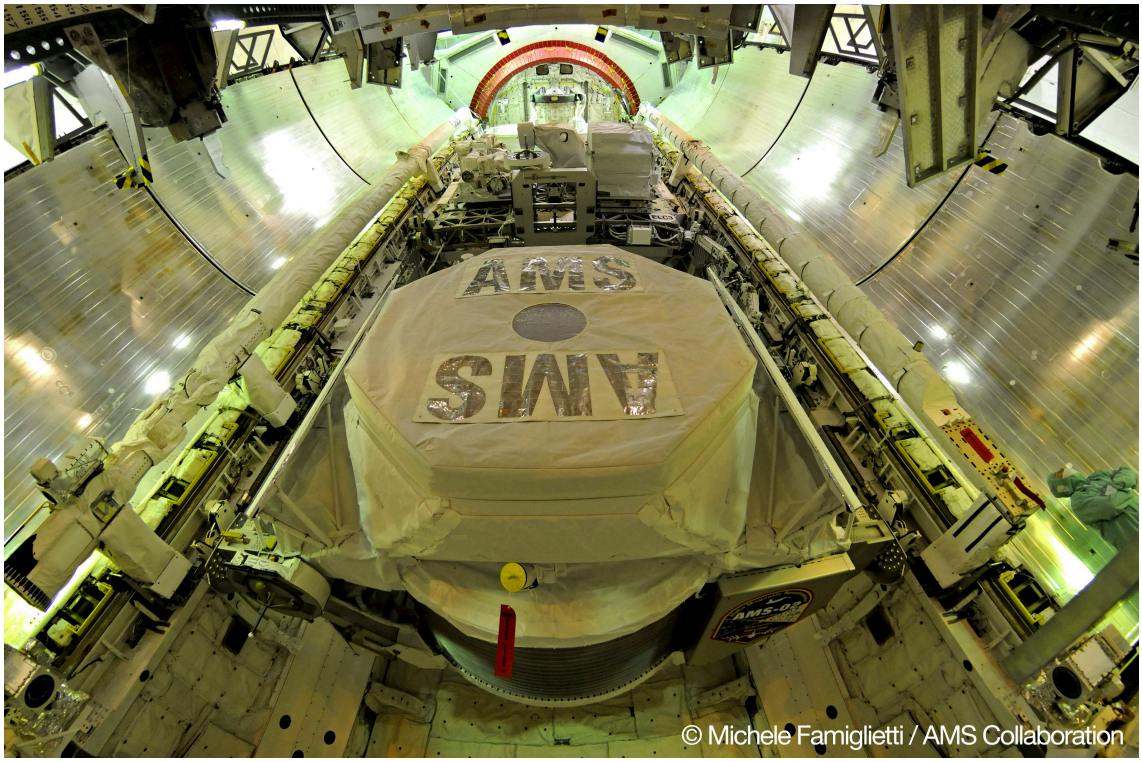

Figure 2.25: The AMS-02 detector installed on the Space Shuttle Endeavour Cargo Bay, ready for the launch.

- inter-calibrate the various sub-detectors with known rigidity beams. The performances of the various sub-detector has been verified (see Fig. 2.24) and in particular the electrons/hadrons rejection power has been investigated.

On August the 28^{th} the detector was shipped to the NASA Kennedy Space Center in Florida. AMS-02 was hosted in the High Bay of the Space Shuttle Processing Facility (SSPF).
The period between September and February was devoted to the mechanical integration with the Shuttle/ISS interface. In parallel the DAQ chain final commissioning was performed. All the DAQ procedures were tested simulating the whole complete chain, from the acquisition in AMS up to the transmission to ground. A period of some weeks has been devoted to the measurement of muons on ground in a stable configurations, This data taking period, that will be discussed in Sec. 4.2 with more details, has been used to check the alignment of the Silicon Tracker with μ^+ and μ^-.

2.4 Launch and installation on ISS

At the end of February 2011 the instrument was installed into the space Shuttle Endeavour Cargo Bay (see Fig. 2.25) on the Launch Pad 39A, ready for the launch.

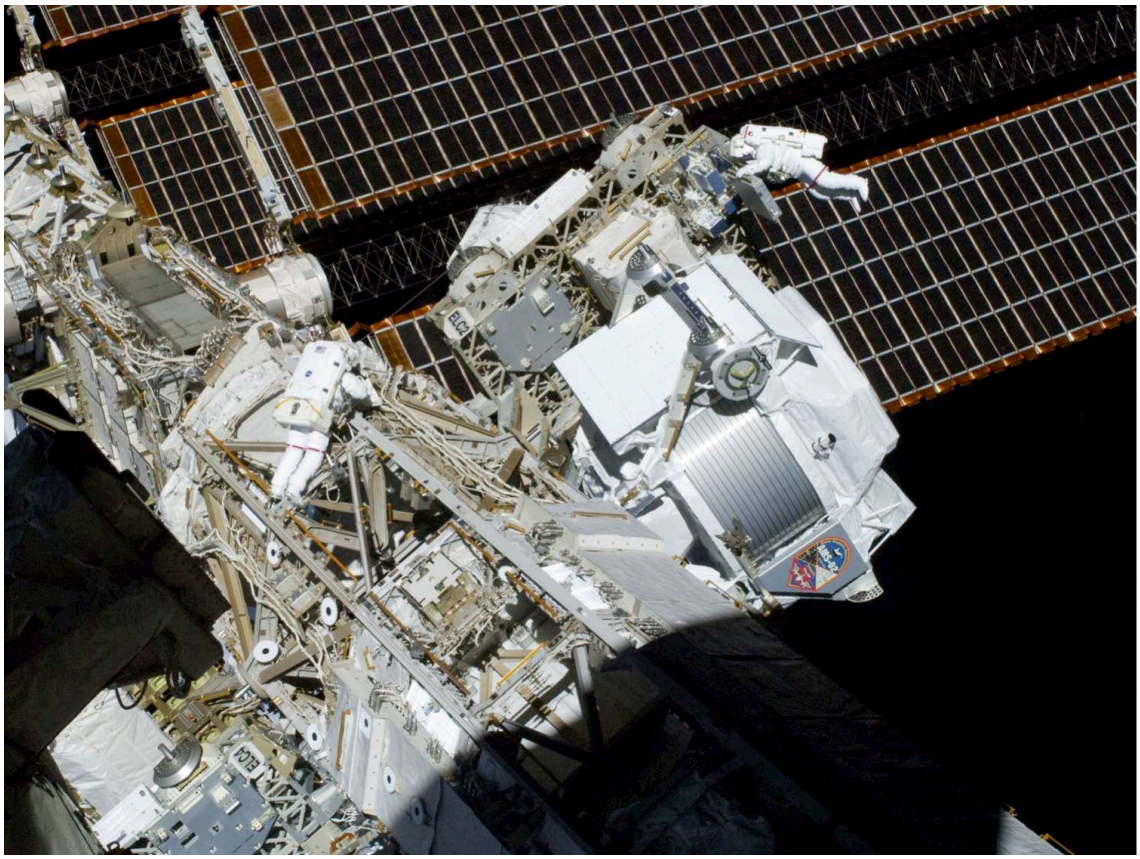

Figure 2.26: The AMS-02 detector installed on the main truss of the International Space Station. Two astronauts in an Extra Vehicular Activity (EVA) around the AMS-02 are visible. In the background the ISS solar panels.

On May 16^{th}, 2011, at 8.56 AM (Cape Canaveral time) the Space Shuttle Endeavour was launched for its STS-134 mission. Approximately 2.5 hours later the electronics of the AMS-02 was powered on and the first slow control data (temperatures and currents) were sent to the ground. The behaviour of the detector electronics was monitored up to the May 19^{th} when AMS-02 was powered off to allow the installation on the ISS.
On May 19^{th}, at 4:46 AM (Houston time) the detector was installed on the main truss of the ISS, where it will be for all the ISS life-time (see Fig. 2.26).
After less than an hour the first activation in the space was performed and the first science data started to be sent on ground. All the detectors were working as expected and no damage due to the launch was found. From then AMS-02 is continuously collecting data at a steady rate of 10^{10} per month. Up to January 2011 $\approx 10^{10}$ events were triggered and 25 TB transmitted to ground.

2.5 The 10 years AMS mission

The main goal of the AMS experiment is to search for antimatter of primordial origin looking for the presence of anti-nuclei into the cosmic rays flux. Another

interesting discover potential for AMS concerns the indirect dark matter detection. Thanks to the large acceptance, the long exposure time and the excellent particle identification capabilities AMS can measure the $\bar{p}$, e^+, γ fluxes with a great accuracy over a never explored energy range. The high statistic AMS-02 measurements of all the charged species of the cosmic rays, including chemical species up to Iron and isotopes up to Carbon, will largely improve our knowledge of the cosmic rays and will help to solve several astrophysics fundamental questions. The unique opportunity offered by the space environment allows the AMS-02 detector to be sensible also to exotic particles, such as strangelets.

2.5.1 Indirect Dark Matter Detection

The actual cosmological model, called ΛCDM, has been formed as the convergence of many independent results. In this model the universe, now in expansion, has a euclidean geometry and is formed of three types of energy: ordinary baryonic matter, dark matter and dark energy. The baryonic matter add up less than the 5%. The dark energy is a sort of repulsive force that makes $\approx$ the 72% of the universe energy. The remaining 23% of energy is constituted by the dark matter. The dark matter evidence comes from different experimental observations. The clearest and intuitive evidence is in the spiral galaxies rotational dynamics. The spiral galaxies, as for example the Milky Way, have a central core surrounded by a rotating disk made of stars and gas. Using Netwon's dynamics to calculate the rotational velocities of stars and gas we have:

$$F = \frac{GmM}{r^2} = \frac{mv^2}{r} \tag{2.4}$$

from which we have the velocity as function of the distance from the center of the galaxy:

$$v(r) = \sqrt{\frac{GM}{r}} \tag{2.5}$$

where G is the gravitational constant, m ed r respectively the mass and the radius of the star or gas, and M is the total mass of the galaxy, inside a disk of radius r.
The experimental observations show a flat velocity for big radii (see Fig. 2.27). This is consistent with a spiral visible galaxy surrounded by a dark matter halo, bigger and with a spherical symmetry.
Observing elliptical dwarf galaxies, again, more mass than the visible one is needed to explain how such structures can be gravitationally bound.
Another evidence is in the Cosmic Microwave Background (CMB). Both the peaks in the power spectrum of the temperature and the fluctuations in terms of CMB polarization gives us precise measurements of the cosmological model parameters: $\Omega_b = 0.0456 \pm 0.0015$, $\Omega_\chi = 0.228 \pm 0.013$ e $\Omega_\Lambda = 0.726 \pm 0.015$ (with Ω_b baryon energy density, Ω_χ dark matter energy density and Ω_Λ dark energy density, in critical density units) [35].
From numerical simulations on the Big Bang Nucleosynthesis (BBN) and on the

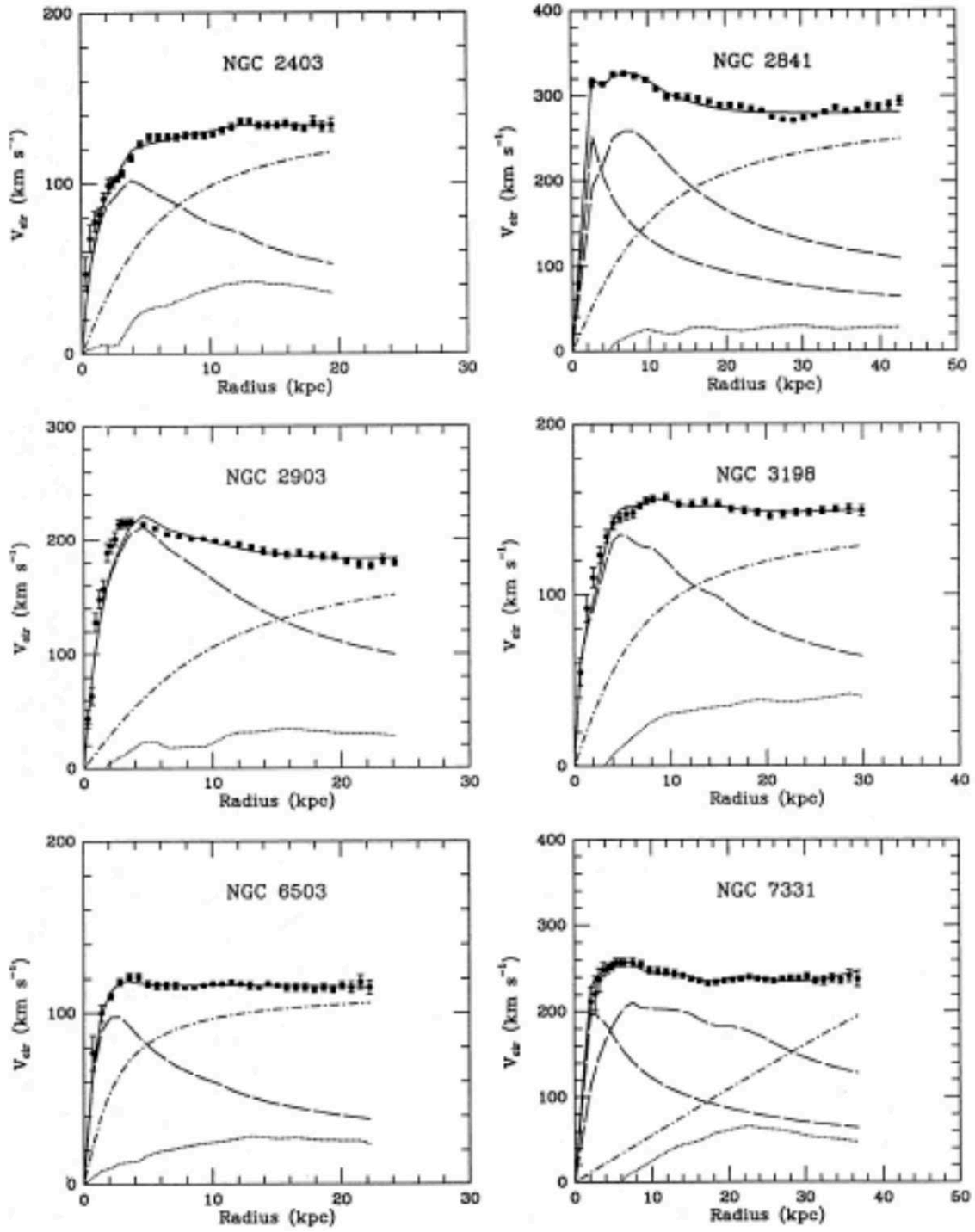

Figure 2.27: Rotational curves for 6 spiral galaxies. Dotted, full and dashed curves are respectively gas, disk and dark matter contributions.

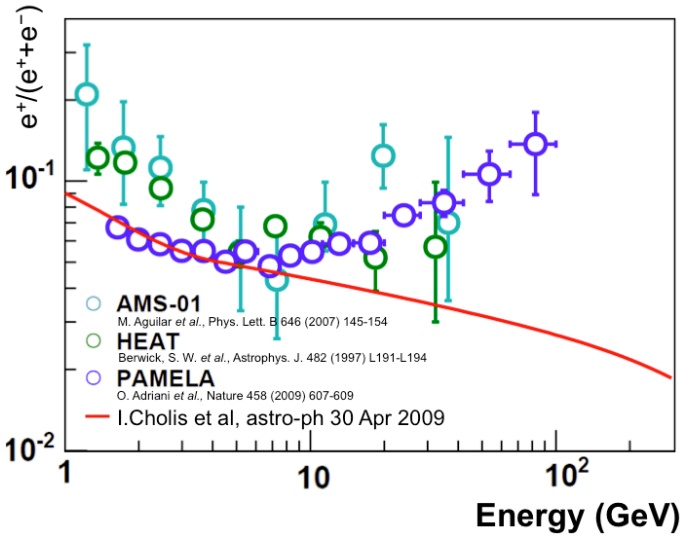

Figure 2.28: The positrons/electrons ratio. The measurements made by AMS-01, Pamela and HEAT are shown. A ratio prediction is superimposed.

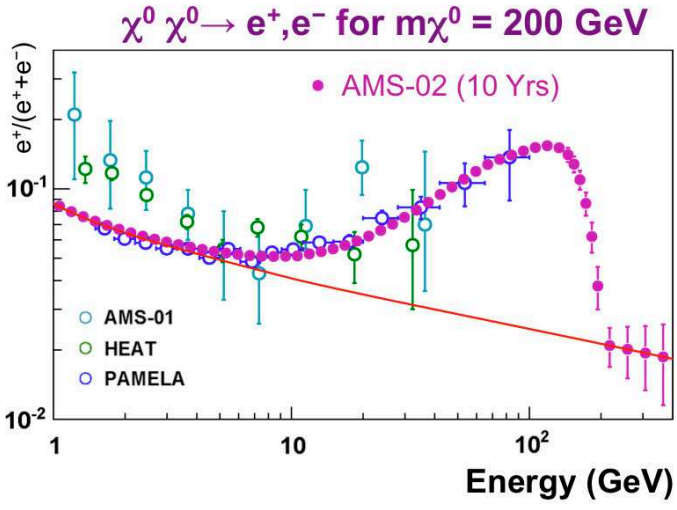

Figure 2.29: The positrons/electrons ratio. The measurements made by AMS-01, Pamela and HEAT are shown. The measurements possible for AMS-02 in a m_{χ^0} = 200 GeV scenario are superimposed.

large scale structures formation, is possible to put limits on the baryon energy density and on the average dark matter energy (a not relativistic dark matter is favoured).
From the previous evidences a dark matter candidate has to be:

- not baryonic: from the discrepancy between Ω_b and Ω_χ from CMB and BBN measurements;
- cold (not relativistic) during the structures formation: to create the observed structures starting from the initial fluctuations observed in the CMB;
- not (or weakly) interactive: from the absence of electromagnetic signals coming from this kind of matter;
- stable: must have a long mean life time, with respect to the Universe age.

Even if also neutrinos and Massive Astrophysical Compact Halo Objects (MACHOs) are consistent with the requests above, they are not sufficient to explain the whole amount of dark matter [24].
An interesting candidate for dark matter is the neutralino. The neutralino, χ^0, is an hypothetical particle with mass between 10 GeV/c^2 and 10 TeV/c^2, and a coupling typical of weak interactions. Neutralinos are stable (i.e. don't' decay) but they could annihilate with each other and giving and excess of *matter* particles. Any excess in antiparticles[2], such as positrons and antiprotons, or in the gamma rays flux could signal the presence of neutralinos. AMS can measure the spectra of the CR rare components ($\overline{p}$, e^+, $\overline{D}$, γ) with a great accuracy and, moreover, over a never explored energy range. In particular the positron channels is very promising as suggested by HEAT and AMS-01 [7, 12] and confirmed by the Pamela and Fermi experiments [3, 50]. In Fig. 2.28 the measurements from AMS-01, HEAT and Pamela are shown, while in Fig. 2.29 the capabilities of the AMS-02 detector are superimposed for a $m_{\chi^0} = 200$ GeV scenario.

2.5.2 Direct Antimatter Detection

Experimental evidences indicate that out galaxy is made of matter. However, there are more than hundred million galaxies in the Universe and the Big Bang theory of the origin of the universe requires equal amounts of matter and antimatter. The process that could create a matter/antimatter asymmetry is called *baryogenesys*. In 1967 A. D. Sakharov [46] formulated the ingredients needed for the baryogenesys:

- direct violation of baryon number conservation;
- C and CP-violation;
- period out of thermal equilibrium.

[2] the excess in particles is more difficult to be revealed from the background of "standard" cosmic rays

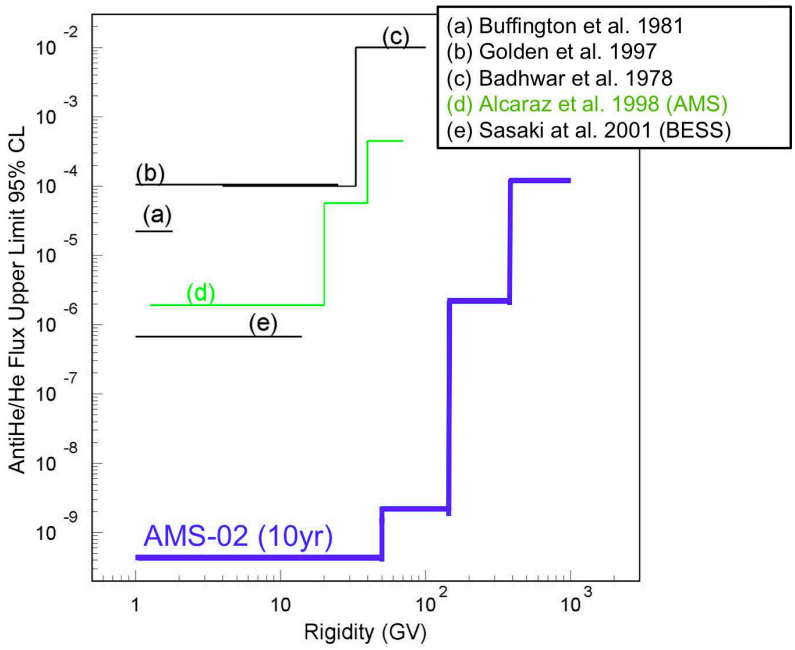

Figure 2.30: The sensibility accessible to AMS-02 in the $\overline{\text{He}}$ search. Here it is compared to the sensibilities reached by previous experiments.

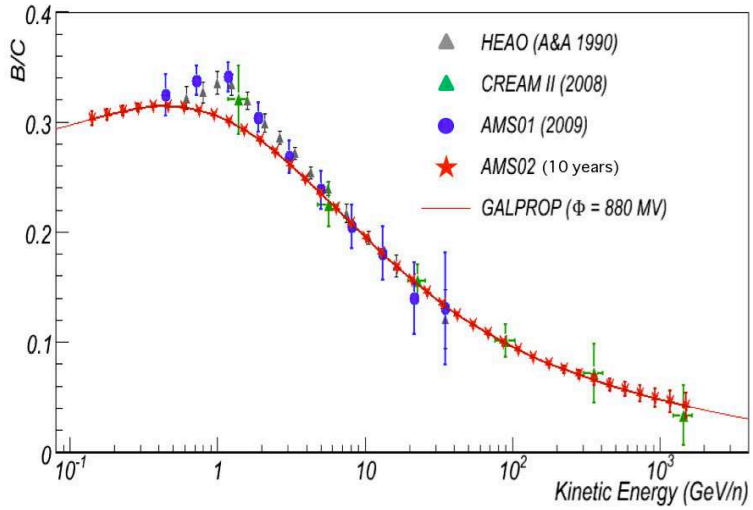

Figure 2.31: The measurement capabilities on the B/C ratio. Some recents measurements and a model are shown.

Even if C and CP-violation were observed (e.g. NA48 in the K system) and several phase transitions are possible for the primordial universe, a baryon number violation has not been never observed. Furthermore also the CP-violation appear too small to explain the baryogenesys.
The probability to produce antinuclei through high energy interactions falls drastically with the amount of antinucleons [27]. The discovery of an antinucleus (e.g. antihelium) would be the evidence of cosmologically significant amounts of antimatter. A discovery of just one anticarbon nucleus would reveal the existence of antistars.
The spectrometric measurement of the rigidities of the particles traversing AMS-02 allows the identification of the charge sign. Thanks to the detector outstanding particle identification capabilities, AMS-02 is able to find an $\overline{\text{He}}$ nucleus between more than 10^9 He nuclei (see Fig. 2.30).

2.5.3 Cosmic Rays Physics and Propagation Models

The AMS-02 high statistics measurements of all the charged species of the cosmic rays, from protons to Iron, including the isotopic separation, will largely improve the knowledge of the cosmic rays physics (see Sec. 1.1.2). The measurement of the nuclear and isotopic composition of cosmic rays (see Fig. 2.31) will be useful to validate or discard the various particle propagation models.

Chapter 3

The Monte Carlo Simulation and the Analysis Qualification

3.1 Introduction

A complete simulation of the AMS-02 detector has been used to evaluate the detector geometrical acceptance and sub-detector efficiencies, to study measurement resolution and to qualify our selection criteria. The AMS-02 detector response to the passage of charged CR is evaluated by means of a simulation program, based on the GEANT4 package [5]. Mechanical drawings and measurements during the assembly are used to describe in details the detector geometry. The GEANT4 package is then used to simulate the energy deposit and interactions of incident particles within AMS-02 active (sub-detectors) and passive (structures and electronics) materials. Physical signals on detecting volumes are then converted in the equivalent experimental signals through the electronics simulation. Eventually the event reconstruction proceeds as it would for real data. The final output of the full simulation is a compressed data file containing the original Monte Carlo record of the generated particle, the kinematical parameters of the particle reconstructed in the different sub-detectors, as well as the relevant sub-detector signals registered in the event.
The simulation software has been developed and is maintained by the Collaboration. Monte Carlo data sample productions are carried in parallel in the separated regional data centers (CERN, Geneva; CIEMAT, Madrid; KIT, Karlsruhe; IN2P3, Lyon; CNAF, Bologna; NLAA, Beijing; SEU, Nanjing; Academia Sinica, Taipei). For this analysis muons, both μ^+ and μ^-, in the energy range 0.1 – 10000 GeV have been generated, simulated and reconstructed.
In this chapter, we will review the different topics of the AMS Monte Carlo simulation which are relevant for our analysis and discuss specific studies performed on the Monte Carlo samples.

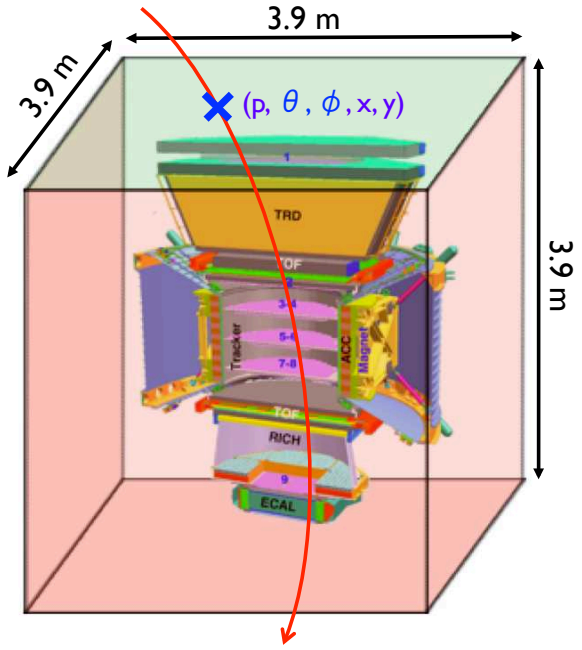

Figure 3.1: A sketch of the AMS-02 Monte Carlo production. The detector is inserted in a 3.9 m side cube. From the top plane an isotropic flux is generated. The particles transport and interactions are simulated with the Geant4 [5] toolkit.

3.2 The Monte Carlo Event Generation

The first step in the simulation consists in the random generation of the particle momentum according to the expected energy and spatial distribution for the physics channel under study. To sample with significant statistics the full energy spectrum observable with AMS, the generation process has to be carefully planned in order to prevent the total number of events to grow beyond a manageable size. The possible optimizations are connected with the choice of the spectrum to be generated and of the generation volume.

3.2.1 The Generation Volume

To simulate a cosmic particles flux the detector is inserted into a l side cube, see Fig. 3.1. From the top plane is generated an isotropic particle flux. The isotropy is obtained generating the particle uniformly over the cube surface and generating uniformly the azimuthal angle ϕ and as $\cos^2$ the zenithal angle θ [49]. The choice of the volume is arbitrary, so a cube both concentric and coaxial with AMS-02 was used. The geometric factor of one face of the cube is easily evaluated as:

$$A_{\text{gen. pl.}} = \int_{S,\Omega} d\vec{\sigma} \cdot d\vec{\omega} = l^2 \int_{\Omega} \sin\theta \cos\theta d\theta d\phi = -\pi l^2 \int_1^0 d\cos^2\theta = \pi l^2 \quad (3.1)$$

The AMS-02 acceptance, the term that includes the geometric factor and all the detection efficiencies, is obtained multiplying the cube geometric factor by

the detection efficiency $N_{rec}(E, \omega)/N_{gen}(E, \omega)$, estimated as the ratio between detected and generated particles [49]. This will be discussed in more details in §5.
The cube side has been set in such a way (3.9 m) that its top plane covers the entire field-of-view of AMS. This leads to a cube top plane acceptance value of 47.78 m^2 sr. To increase the saving in terms of computational time required for the simulation only events with $\theta \leq 45°$ (the maximum angle in Time-of-Flight acceptance, that defines the AMS-02 field-of-view) are propagated.

3.2.2 Energy Spectrum

The acceptance of a complex detector can be evaluated both using a continuous momentum spectrum or a discrete (beam-like) one. The former case is more suitable for a direct comparison of the properties of the reconstruction algorithm and of the analysis workflow. So we chose to generate a continuos energy spectrum. As shown in §1.4 the muon differential energy spectra can be described, at high energies, by a power law with index $\sim$ -3.7. This would imply that to generate a significant statistics at energies above O(100 GeV), according to its natural shape, the corresponding number of events generated in the low energy part should be several orders of magnitude larger. With this approach the total number of generated events can easily grow out of scale. However the detector response may be studied with a probe spectrum and the results for a different input spectrum obtained just weighting the events accordingly.
The chosen probe spectrum follows an inverse law with energy $dN/dE \propto E^{-1}$: this provides an enhancement in the event production at high energies, while keeping a larger statistical weight for the low energy part of the spectrum. As a further optimization of the process, the generation range was split into two sub-ranges, namely $0.1 - 2500$ GeV and $2500 - 10000$ GeV, where the MC production took place separately. In our analysis, we have considered the data produced over the whole energy range, studying separately the two energy intervals and combining the results according to the different statistical weights of the two samples. In the following we will always refer to these combined results.
However the use of the probe spectrum in the comparison Data/MC on the variables used in the analysis cuts makes no sense. For the reliable comparison and the acceptance estimation, the probe spectrum (power law index -1) has to be modified to be similar to the real muon spectrum (about power law index -3.7). This can be done in two ways:

Reweighting: the events are reweighted keeping the statistical significance of the generated ones. The weight factor (W) is function of the generation momentum ($W = W(p_{\text{gen}})$);

Hit&Miss: not all the produced events are used and part of the production is rejected. The rejection factor (W) is function of the generation momentum (p). With this approach all the statistic fluctuations present in the data are kept but greater is the momentum and more are the unused produced events.

In both approaches the rejection/reweighting factor is proportional to the physical spectrum $\varphi(p)$, determined in our case from BESS and L3+C vertical muon spectrum measurement [1, 31], and to the inverse of the generated one (p^{-1}):

$$W(p_{\text{gen}}) \propto \frac{\varphi(p_{\text{gen}})}{p_{\text{gen}}^{-1}} \tag{3.2}$$

3.3 Event reconstruction

The event is propagated into the magnetic field and into the materials. Interaction of particles in matter and with magnetic field are simulated using the GEANT4 toolkit and, starting from the energy deposits into the various detectors, the signal formation, digitization and data compression are simulated. The latter part of simulation has been written directly by the Collaboration and has been tuned to describe, as best as possible, the real detector features.
Once the signals are produced and the complete read-out event has been built the generated event is fed to the event reconstruction algorithm and analyzed just as a real one: the trigger is evaluated and, if the case, the high-level sub-detector quantities are evaluated.
Each sub-detector is first treated as a stand-alone system and its raw data are searched to identify simple patterns (e.g. groups of nearby read-out channels above a threshold). When a pattern is found, it is stored internally in a C++ object containing all the relevant information carried by the pattern itself. Those objects are used in turn to identify higher level patterns, specific to the particular detector, that carry additional information and so on. In this way data are organized into hierarchical structures that allow to easily recover the low level information used to evaluate the characteristics of the top level objects. These object hierarchies are eventually stored on disk using the ROOT [19] TTree data structure, which contain the full MC data along with the results of the reconstruction.
When the first phase of the reconstruction is completed, the top level structures from each sub-detector, namely - TRDTrackR from the TRD, BetaR for the TOF, TrTrackR from the TRACKER, RichRingR from the RICH and EcalShowerR from the ECAL - are further combined into the highest level structure of the reconstruction, the ParticleR. To build the ParticleR, the spatial information of each candidate data structure is extrapolated towards the other detectors and a geometrical matching is performed, and the other available informations are also checked against huge inconsistencies and are possibly refitted using the additional information now available from the other detectors.

3.4 Momentum Resolution Evaluation

The Monte Carlo is used also to evaluate the spectrometer resolution. A $(1/R_{\text{rec}} - 1/R_{\text{gen}}) \cdot (1/R_{\text{gen}})^{-1}$ as function of R_{gen} distribution is used, where R_{rec} is the reconstructed rigidity and R_{gen} the generated one. The bi-dimensional distribution

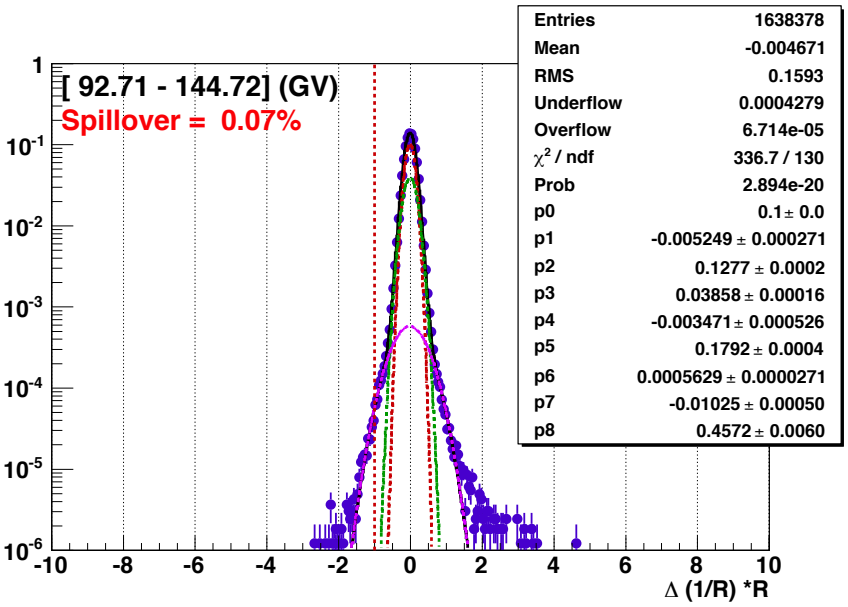

(a)

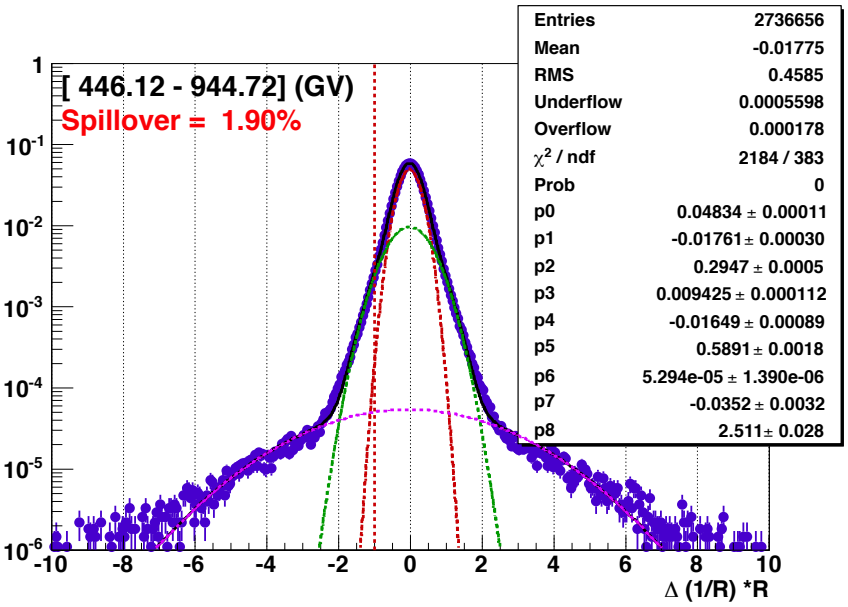

(b)

Figure 3.2: Distribution of $(1/R_{\text{rec}} - 1/R_{\text{gen}}) \cdot (1/R_{\text{gen}})^{-1}$ in the Max Span configuration (see Sec. 4.4.7), for two different rigidity ranges (a) 92.71 – 144.72 GeV, b) 446.12 – 944.72 GeV). The spectrometer resolution is the weighted mean of the 3 gaussian σ's. The line (Δ(1/R)*R=-1) below the which the particles are reconstructed with a wrong sign of charge and the amount of spillover is reported.

is divided in several rigidity range slices. Each slice is fitted with a sum of three gaussians. The weighted - the gaussian area is used as weight - mean of the gaussians means is how the effective resolution is evaluated: higher is the true generated rigidity, worst is the resolution. The distribution used is the difference of the inverse rigidities since $1/R$ is the gaussian quantity for a magnetic spectrometer. All the three gaussian means should be equal to zero, except at very low rigidities (below 200 MV) where the energy losses into the detector material make systematically a lower reconstructed rigidity with respect to generated one.
The three gaussian fit is needed to describe properly also all the tails of the distributions. Events reconstructed below -1 are reconstructed with the wrong sign of rigidity and constitute the *spillover*.
In Fig. 3.2 an example of resolution evaluation, for two different rigidity ranges, is reported. The amount of spillover is reported as well.

3.5 Efficiency Analysis

The aim of the analysis workflow and of the cut chain is to increase the signal quality, rejecting background and mis-reconstructions. A good selection should have the following properties:

1. maximum efficiency for signal: events of the specie under study must survive the cut;
2. maximum rejection on mis-reconstructed events: events without the required quality on detection and off-line reconstruction have to be rejected. These events are potentially dangerous. They can be due to background or, even if due to signal, they can contaminate the measure;
3. maximum rejection of background: the events of different species have to be rejected completely by the cut.

In real cases one single cut is devoted to satisfy, more efficiently as possible, point 2 or point 3.
To evaluate the efficiency on background, with respect to signal, the background should be simulated. This means make a MC production for all the species, that can contaminate the measure, each with its own spectrum. A good cut is the one that has the maximum efficiency on signal and minimum on other species.
In our analysis the principal background contamination comes from low energy protons. This contamination is limited at % level and can be cross-checked with the negative sign muons, for which this background is absent.
To evaluate the efficiency against mis-reconstructions is necessary to define what corresponds to a "well detected" event. For this analysis the MC sample has been divided into 4 sub-samples based on the spectrometric quality of the reconstruction:

Wrong Charge (WC): events reconstructed with the wrong sign of the charge. This events can be due to spillover or to anomalous deflection in the detector;

Good: all the events within $3\,\sigma$ of AMS-02 resolution. The resolution is function of Rigidity and has been evaluated, in MC, after all the cuts used in the analysis;

Low Reco (LR): all the events with a low measured (≤ 4 GV) but high generated (≥ 40 GV) rigidities. These events are generally due to interactions into the detector. Typical cases are the pair production from muon, muon decay, muon interaction with δ rays production;

Bad: all the remaining events.

These categories are shown in Fig. 3.7. The "Wrong Charge" particles are mainly at high rigidities, due to the spillover effect.
For all the cuts developed for this analysis the efficiency was evaluated. If the efficiency for "Good" events is greater than for other categories the cut is kept: this guarantees a response function of the detector (i.e. the resolution matrix) more diagonal (see Fig. 3.8).

3.6 Monte Carlo Flux

The flux measurement has been tested using only Monte Carlo information. Monte Carlo data have a known spectral shape, and applying to the reconstructed quantities the selection chain and the flux computation procedure is possible to observe possible systematics deviation of the reconstructed MC flux from the injected spectrum. This is particularly important for the understanding of the effect of the finite experimental resolution.
The procedure is to start from the probe Monte Carlo spectrum muon sample, i.e. distributed as a momentum power law of spectral index -1, then modify the spectral shape to match with the best known muon spectrum on-ground measurement, namely derived from L3+C and BESS measurements [1, 31]. The shaping procedure has been implemented in two ways: using a reweighted spectrum technique or with a Hit&Miss method. In the former case every event has an associated weight used to fill reconstructed variables histograms. This flux determination will have a very small error at high energies and will point out more clearly systematic effects of the finite experimental resolution. In the latter case the muon spectrum expected statistics for the given exposure time is simulated. This correspond to a more realistic flux measurement simulation, and will reveal also the statistics effect fluctuation.
Then the selection applied on Data is applied also on Monte Carlo sample, and the raw number of counts derived. Then acceptance is applied to the measurement and a Monte Carlo flux is derived. Another ingredient to obtain the Monte Carlo flux is to calculate the equivalent exposure time, this is not strictly needed since represents only a scaling factor.
An important caveat is connected to the fact that the acceptance, derived from Monte Carlo, and the MC flux are derived from the same simulated events, and some systematic effects could be suppressed.

3.6.1 Reweighting

Every simulated event has an associated weight given by $p_{gen}\varphi(p_{gen})$ where φ is the spectral shape derived by BESS and L3+C data. The MC sample, that has different components of each sign, has randomly divided in μ^+ and μ^- simulating an injected $\mu^+/\mu^- = 1.5$ ratio, independently from rigidity. In particular every five produced muons, randomly, two has been considered as μ^- (the generated rigidity, R_{gen}, has been considered negative and the reconstructed one, R_{rec}, with the sign taken from $-R_{gen}R_{rec}/|R_{gen}R_{rec}|$) and three as μ^+ (R_{gen} positive and R_{rec}, with the $+R_{gen}R_{rec}/|R_{gen}R_{rec}|$ sign).
Dividing the raw number of reweighted counts shown in Fig. 3.3 by the acceptance and an arbitrary exposure time the flux shown in Fig. 3.4 is obtained. The reconstructed flux looks quite similar to the injected one. At very low ($\sim 100\,\text{MeV}$) and very high ($\sim 1\,\text{TeV}$) energies the spectrum starts to be deformed, but mainly by so called Good events. Very low rigidity (below 0.5 GV) part of the spectrum is enriched by the energy losses inside the detector material. High rigidity part is contaminated, instead, by lower energy particles. This is due to the worsening of rigidity resolution in conjunction with a power law falling spectrum. Approaching Maximum Detectable Rigidity particles have a such large rigidity resolution that spillover should be considered as a straightforward effect. No further selection can be applied to remove mis-reconstructions from the sample.

3.6.2 Hit&Miss

In additions to the reweighted sample an Hit&Miss MC sample has been produced. The sample has been obtaining extracting randomly events from the MC sample. The extraction has been performed using the Hit&Miss technique following the known spectrum of muons. The Hit&Miss probability has been tuned to have a statistics comparable to the Data one (~ 20 muons in the last bin useful for analysis, $\sim 1\,\text{TeV} - 2.5\,\text{TeV}$). The μ^- and μ^+ separation has been produced following the same rule exposed in the previous section. The MC sample generated with this has the following features:

- statistically comparable to the Data: positive and negative spectra are similar to the Data ones;
- know injected spectrum and ratio: the injected spectrum is the combination of L3+C and BESS spectra [1, 31], the ratio is 1.5;
- statistically independent from the sample used to calculate acceptances and resolution matrix: this is needed to use the sample to the unfolding (see Sec. 3.7).

The same procedure followed for the reweighted MC sample has been applied to obtain the Hit&Miss flux, see Fig. 3.6 where flux is scaled by $R^{3.71}$. As in the previous case, the reconstructed flux is deformed at low rigidities by energy losses in detector materials and at high rigidities due to the worsening of rigidity

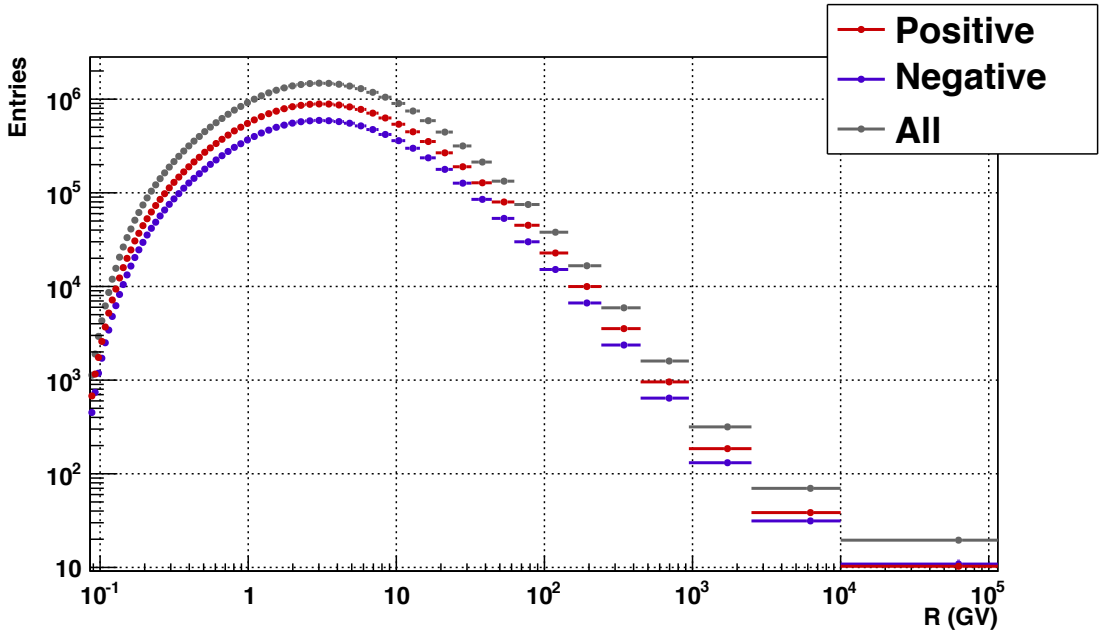

Figure 3.3: Raw number of counts in Reweighted MC sample after applying the same selection used in Data. Positive (red) and negative (blue) reconstructed particles are shown. Overall number of counts (grey) is shown as well. Errors on y are statistical and, given the extremely abundant MC production, negligible.

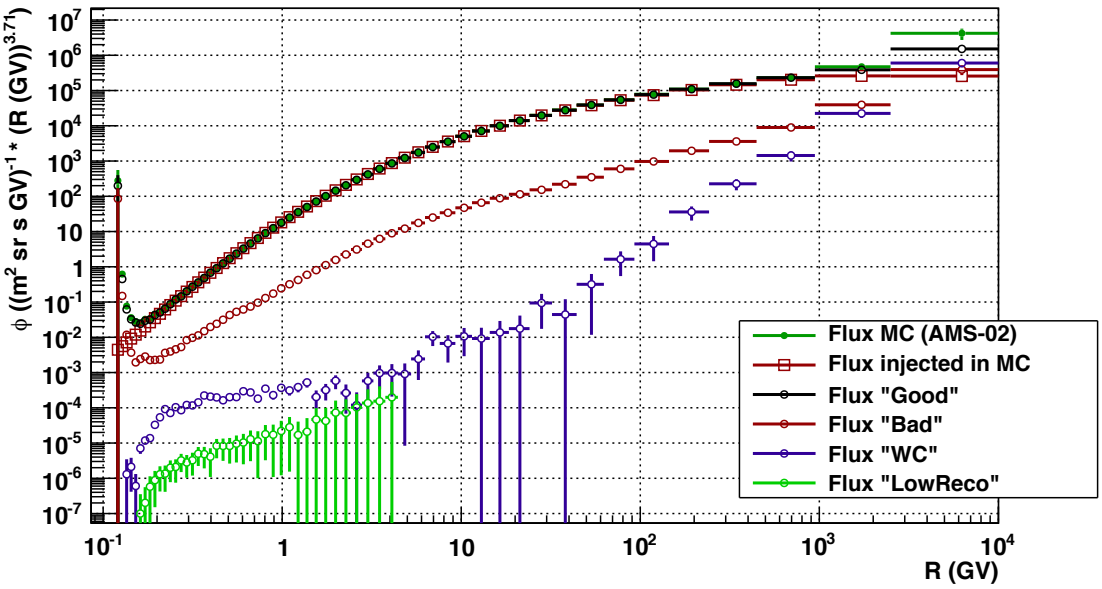

Figure 3.4: Flux obtained applying the selection on a Reweighted MC sample and dividing by the acceptance and an arbitrary ΔT (a free scale factor). The reconstructed flux (green) and the injected one (square red) are shown. The various components of the reconstructed flux are superimposed: "Good" (black), "Bad" (red), "Wrong Charge" (blue) and "Low Reco" events. Fluxes have been scaled by $R^{3.71}$.

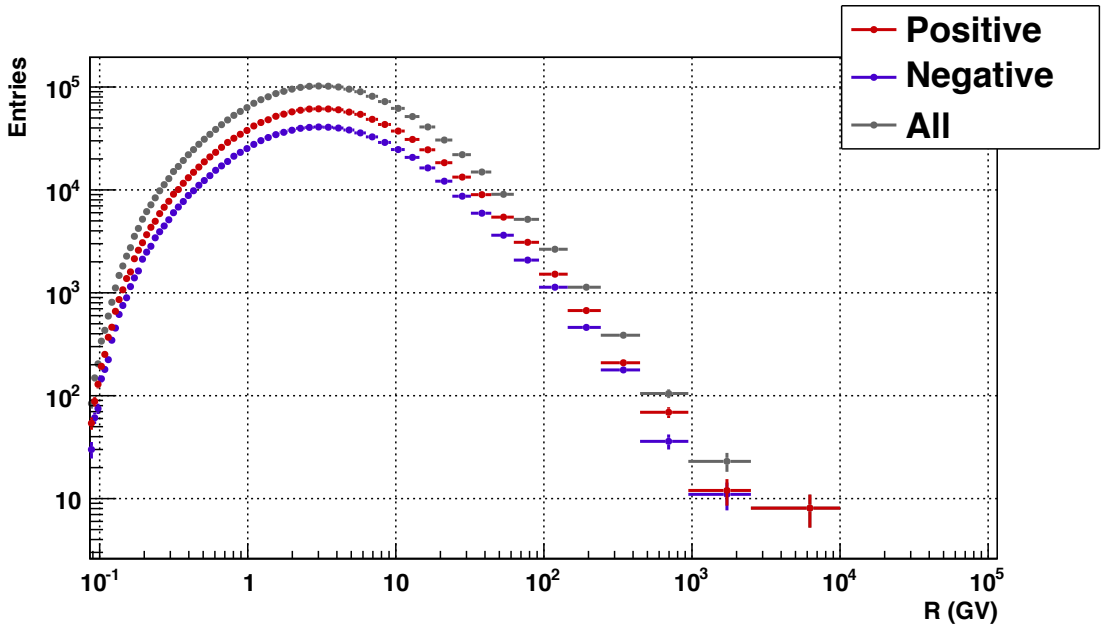

Figure 3.5: Raw number of counts in Hit&Miss MC sample after applying the same selection used in Data. The MC sample has been extracted obtaining $\sim$ the same statistics of Data (see Fig. 5.1). Positive (red) and negative (blue) reconstructed particles are shown. Overall number of counts (grey) is shown as well. Errors on y are statistical.

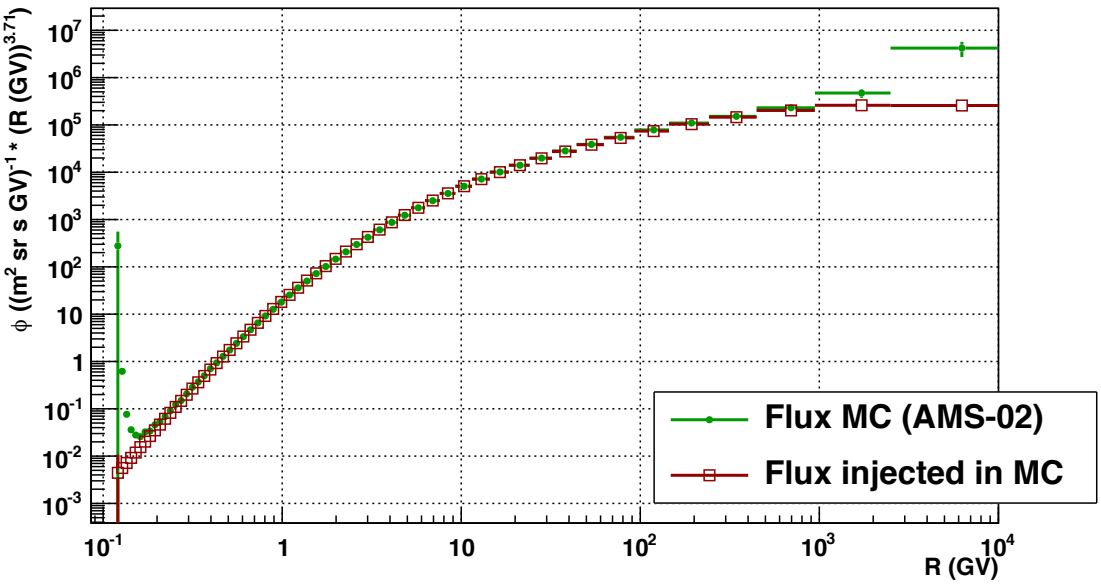

Figure 3.6: Flux obtained applying the selection on a Hit&Miss MC sample and dividing by the acceptance and an arbitrary ΔT (a free scale factor). The reconstructed flux (green) and the injected one (square red) are shown. Reconstructed flux is deformed at low rigidities by energy losses in detector materials and at high rigidities for worsening of rigidity resolution. Fluxes have been scaled by $R^{3.71}$.

resolution.
Is clear that for achieve the correct spectral shape, especially at high energies, an unfolding procedure is needed. The unfolding, that will be discussed in details in next section §3.7, has been tuned with the reweighted MC sample and tested for systematics on the Hit&Miss one.

3.7 Unfolding

Knowing the response function of the instrument (i.e. resolution matrix, see Fig. 3.8) is possible to correct the deviations induced in the measured spectrum by the finite resolution. This procedure is called unfolding. In an ideal way of treating the problem the response function can be seen as the matrix that multiplied by the array of causes (i.e. binned "true" spectrum) gives the array of effects (i.e. binned measured spectrum). In this simplified picture is sufficient to mathematically invert the matrix and apply it on effects to obtain the causes. In real life effects are a probabilistic quantity and also our knowledge of the matrix is achieved in a probabilistic way (i.e. a MC sampling). The inversion of the matrix has to be performed with a probabilistic approach.
The algorithm chosen for this analysis is the unfolding developed by Giulio D'Agostini [22]. The software used is a D'Agostini's algorithm implementation contained in the RooUnfold package [4]. The algorithm has been customized for this analysis as explained below.
The D'Agostini method uses a Bayesian approach. The core of the algorithm is the use of the Bayes's theorem:

$$P(C_i|E_j, I) = \frac{P(E_j|C_i, I) \cdot P(C_i|I)}{\sum_i P(E_j|C_i, I) \cdot P(C_i|I)} \tag{3.3}$$

where $\mathbf{C} = \{C_0, C_1, ...\}$ are the causes (i.e. C_n is a "true" rigidity in bin n), $\mathbf{E} = \{E_0, E_1, ...\}$ the effects (i.e. E_0 is a "measured" rigidity in bin n) and I is the state of information under which the analysis is performed (for example that 1 TeV muon is less probable than a 1 GeV one).
One can use the Eq. 3.3 to invert the resolution matrix ($\lambda_{ji} \equiv P(E_j|C_i, I)$) obtaining:

$$\theta_{ij} = \frac{\lambda_{ji} \cdot P(C_i|I)}{\sum_i \lambda_{ji} \cdot P(C_i|I)} \tag{3.4}$$

having defined $\theta_{ij} \equiv P(C_i|E_j, I)$ in analogy with the resolution matrix λ_{ji}. To evaluate the θ_{ij} one needs the resolution matrix (evaluated by MC sampling) and the *a priori* knowledge of the "true" spectrum ($P(C_i|I)$). The latter term, called *prior* (while instead the left side of Eq. 3.3 is referred as *posterior*), reflects our state of information (i.e. the probability for 10 TeV muons to contaminate the 1 GeV ones has to be very small even if the corresponding resolution matrix term is wide). A flat prior ($P(C_i|I) = k$), in this case, means that we suppose a flat spectrum (and is not our case) as the most probable. The number of counts in each effect-bin can be shared in the cause-bins as:

$$x(C_i)|_{x(E_j)} \approx P(C_i|E_j, I) \cdot x(E_j) = \theta_{ij} \cdot x(E_j) \tag{3.5}$$

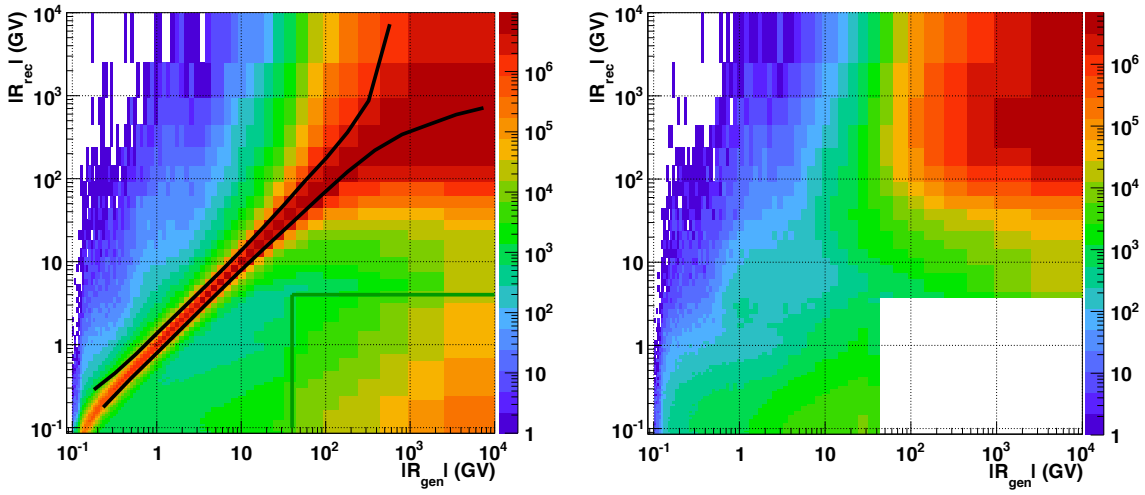

(a) (b)

Figure 3.7: Response function (i.e. resolution matrix) of the AMS-02 detector before the selection of this analysis. a) "Good" events (inside the black curves), "Low Reco" (inside the green box), "Bad" (the others). b) "Wrong Charge" events. The matrix is deeply not diagonal, due to mis-reconstructions.

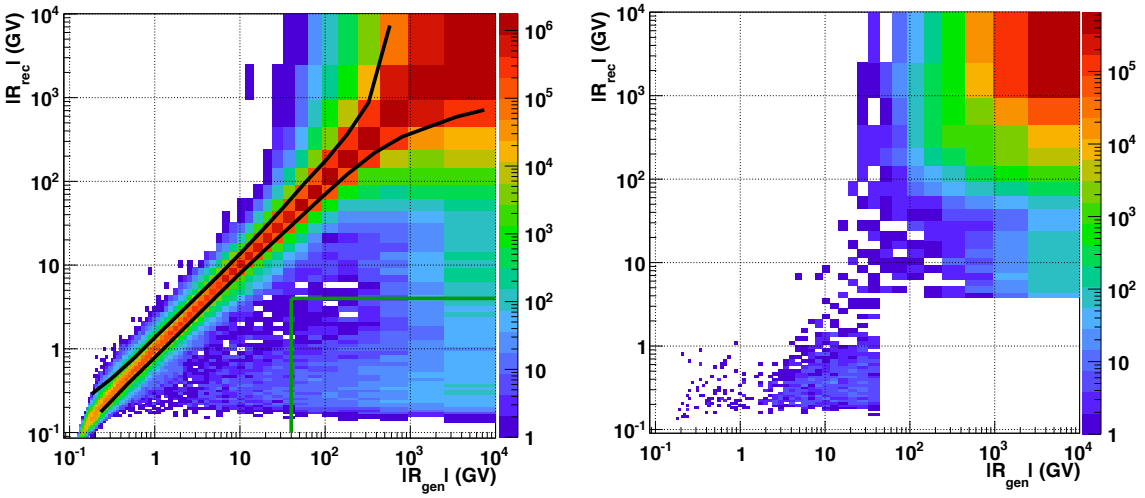

(a) (b)

Figure 3.8: Response function (i.e. resolution matrix) of the AMS-02 detector after the selection of this analysis. "Good" events (inside the black curves), "Low Reco" (inside the green box), "Bad" (the others). b) "Wrong Charge" events. The matrix has been made almost diagonal (with respect the one in Fig. 3.7) by selection. At very low energies (below $\sim$ 0.5 GV) are really visible the energy losses bending the matrix. Increasing the rigidities the resolution worsen and the matrix becomes wider. The wrong charge particles are mainly at high rigidities, due to the spillover effect.

considering only the E_j. The spectrum due to all observation (i.e. the complete observed spectrum):

$$x(C_i)|_{\mathbf{x}_E} \approx \sum_{j=1}^{n_E} P(C_i|E_j, I) \cdot x(E_j) = \sum_{j=1}^{n_E} \theta_{ij} \cdot x(E_j) \tag{3.6}$$

The unfolded spectrum ($\mathbf{x}_C$) can "remember" the prior used. This can be cured iterating the procedure, inserting the posterior as prior in another step of unfolding.
The naive idea of iterating up to complete forgetfulness of the prior, unfortunately, fails since a kind of positive feedback makes the unfolded spectrum asymptotically 'crazy'. This can be cured using the concept of *regularization*: the posterior is smoothed before being used as prior in the next iteration. The two effects will be shown below.
The original RooUnfold package has been modified, for this analysis, both in the prior and in the smoothing features. The original algorithm had not the possibility to insert a prior (a flat one was used) and the smoothing was too heavy for our case. A very simple smoothing algorithm has been used for this analysis. The content of bin i (BC_i) is obtained from:

$$BC_i = 0.99BC_i + 0.005BC_{i-1} + 0.005BC_{i+1} \tag{3.7}$$

This is a very slow smoothing and was chosen having to deal with power law spectra.
The unfolding is applied to raw number of counts and a corrected number of counts (bins content becomes not integer) is produced. Then acceptance and ΔT are applied in the standard way to produce the physical flux.
The unfolding has been tested on Hit&Miss MC sample and the result is shown in Fig. 3.9.
The unfolding acts both at high and low rigidities: at low rigidities it corrects energy losses and at high one it reduces the contamination due to lower rigidities particles. Above the MDR, the unfolding is however correcting the flux in the right direction but the measurement capability is completely lost: this leads to an error (how it is evaluated will be discussed later) that is greater than 100%. The flux measurement will be quoted only up to 2.5 TV.
The convergence of the algorithm has been granted looking at the χ^2 of changes between iterations and the flux unfolded with different priors. Three different priors have been used and compared: the really measured flux (not unfolded), the flux measured by BESS [31] and a flat spectrum. The flux that will be quoted has been unfolded using, as prior, the flux measured without the unfolding. In Fig.3.10(a) is shown the value of χ^2 of changes in flux with respect the previous iteration. In the first $\sim$ 5 iterations the flux is changed copiously while later iterations are useful to forget completely the knowledge of the used prior. In Fig. 3.10(b) is shown, instead, the ratio between the three fluxes unfolded with different priors. After 100 iterations the flux is the same, independently from prior, within the errors.
In Fig. 3.11(a) is shown the flux unfolded with 100 iterations and without smoothing. The procedure becomes driven by positive feedbacks and the unfolding acts

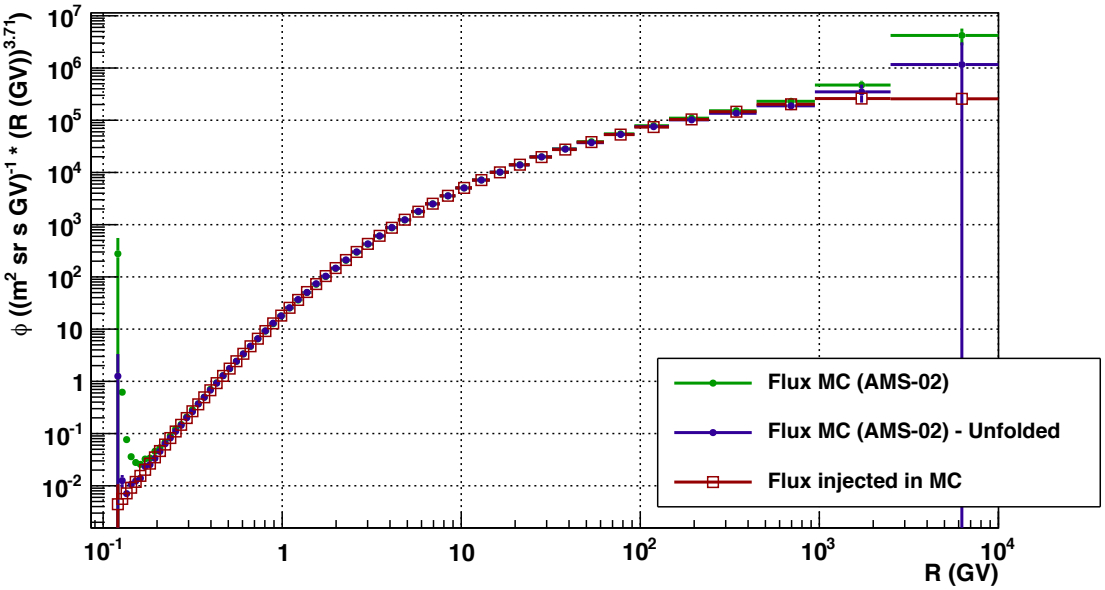

Figure 3.9: MC flux unfolded (blue). MC flux without unfolding (green) and injected flux (red) are superimposed for comparison. Unfolding acts both at high and low rigidities. Fluxes have been scaled by $R^{3.71}$.

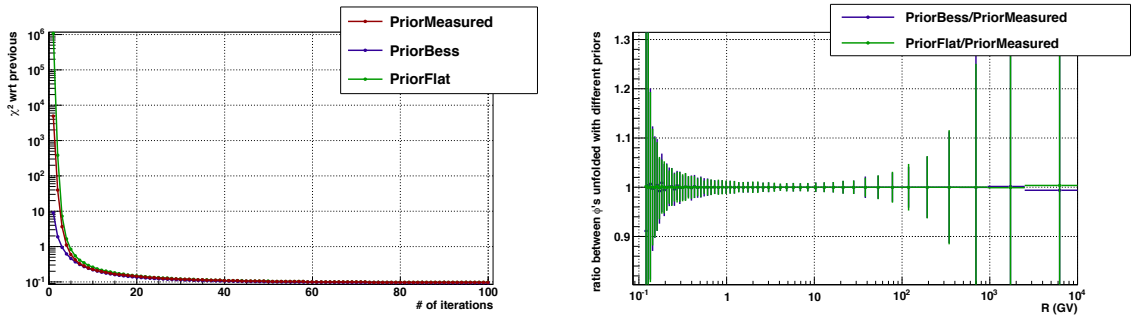

(a) (b)

Figure 3.10: a) Value of χ^2 of changes in flux with respect the previous iteration. In the first $\sim$ 5 iterations the flux is changed copiously while later iterations are useful to forget completely the knowledge of the used prior. b) Ratio between the three fluxes unfolded with different priors. After 100 iterations the flux is the same, independently from prior, within the errors. Three different priors has been used and compared: the really measured flux (not unfolded), the flux measured by BESS [31] and a flat spectrum.

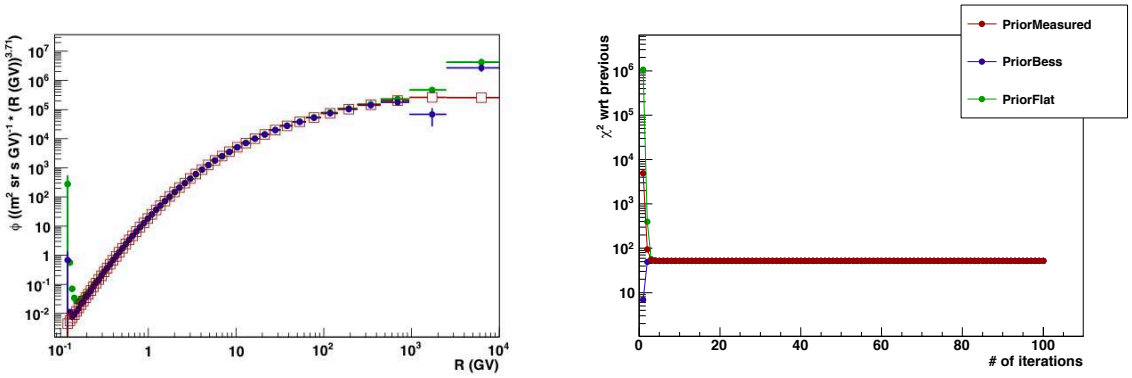

(a) (b)

Figure 3.11: a) Flux unfolded (blue) after 100 iterations without smoothing. Not unfolded (green) and injected (red) fluxes are superimposed for comparison. The procedure becomes driven by positive feedbacks and the unfolding acts too much. Errors are only statistics. b) Value of χ^2 of changes in flux with respect the previous iteration. The smoothing applied is too much heavy and the posterior is changed after an iteration before being inserted as prior in the next iteration: the smoothing makes negligible the unfolding itself.

too much. In Fig. 3.11(b) is shown the value of χ^2 of changes in flux with respect the previous iteration. The applied smoothing applied changes too much the posterior after an iteration before inserting as prior in the next step: the smoothing makes ineffective the unfolding itself.
With the Hit&Miss MC sample, having the same statistics, and so the same fluctuations, than in Data, the unfolding has been tuned and validated for this analysis. The error on the algorithm itself has been evaluated unfolding several times the spectrum. The initial raw number of counts is smeared following a Poisson distribution[1], with the observed number of entries used as mean value μ[2]. The fluctuated raw number of counts is unfolded and the result compared with the main unfolded flux. Repeating this toy MC 50 times one can construct a complete covariance matrix and evaluate the variance of each single bin. The output error will contain all the statistical part of the error and, in addition, the systematic error due to unfolding.
The discrepancy between the flux injected in MC and the flux reconstructed and unfolded has been evaluated and is shown in Fig. 3.12. The residual error, not removed by unfolding, is well contained in the error coming from the unfolding procedure: the procedure gives an error that contains the statistic error and the residual systematic due to the finite resolution.

[1] the error on each bin is considered multinomial combined with a Poisson distribution for the total number of entries: this gives a Poisson distribution for each bin.

[2] the statistical correct way of treating the problem is using the conjugate of the Poisson distribution, the Γ function: the observed number of entries is not the mean value but simply comes from a Poisson distribution with unknown parameter μ.

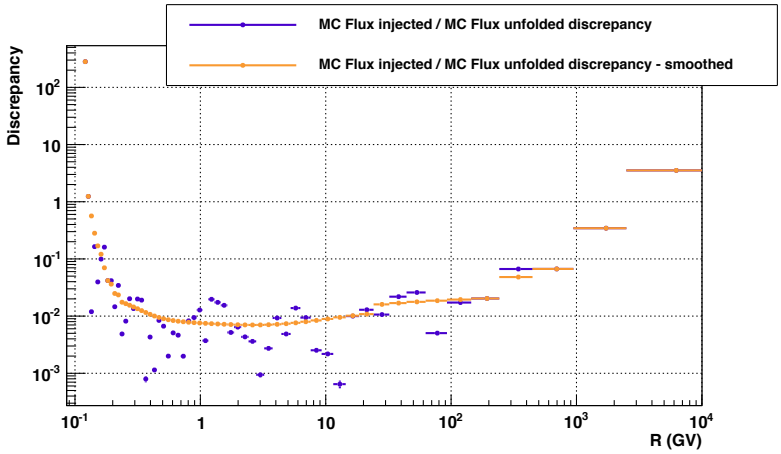

Figure 3.12: Discrepancy between flux injected in MC and flux reconstructed and unfolded (blue). The distribution has been smoothed to remove punctual fluctuations (orange).

3.8 Monte Carlo Ratio

The evaluation made, for "vertical" flux, on a purely MC base, has been repeated also for the μ^+/μ^- ratio. The result is shown in Fig. 3.13. In the MC has been injected a 1.5 value of ratio, independently from rigidity. The reconstructed ratio fits well the injected one. At high rigidities, above 100 GeV, the poor statistics and the finite resolution induce some fluctuations on the measurements.
For the ratio the errors has been evaluated considering a Binomial probability $r{=}\mu^-/\mu$, in a certain rigidity bin, to have $n{\cdot}r$ μ^- muons within a sample of n muons. In each rigidity bin:

$$\sigma\left(\frac{\mu^+}{\mu^-}\right) = \sigma\left(\frac{\mu^+ + \mu^-}{\mu^-} - 1\right) = \sigma\left(\frac{\mu^+ + \mu^-}{\mu^-}\right) = \sigma\left(\frac{\mu}{\mu^-}\right) \tag{3.8}$$

From propagation of error:

$$\sigma\left(\frac{\mu}{\mu^-}\right) \Big/ \frac{\mu}{\mu^-} = \sigma\left(\frac{\mu^-}{\mu}\right) \Big/ \frac{\mu^-}{\mu} \rightarrow \sigma\left(\frac{\mu}{\mu^-}\right) = \sigma\left(\frac{\mu^-}{\mu}\right)\left(\frac{\mu}{\mu^-}\right)^2 \tag{3.9}$$

And applying the binomial error to μ^-/μ:

$$\sigma\left(\frac{\mu^-}{\mu}\right) = \sqrt{\frac{\frac{\mu^-}{\mu}\left(1 - \frac{\mu^-}{\mu}\right)}{\mu}} = \frac{1}{\mu}\sqrt{\frac{\mu^-\mu^+}{\mu}} \tag{3.10}$$

that leads to:

$$\sigma\left(\frac{\mu^+}{\mu^-}\right) = \frac{1}{\mu}\sqrt{\frac{\mu^-\mu^+}{\mu}}\left(\frac{\mu}{\mu^-}\right)^2 = \frac{1}{\mu^-}\sqrt{\mu\frac{\mu^+}{\mu^-}} \tag{3.11}$$

The discrepancy between the ratio injected in MC and the ratio reconstructed and has been evaluated and is shown in Fig. 3.12. The distribution has been smoothed to remove punctual fluctuations and will be added to the ratio systematics.

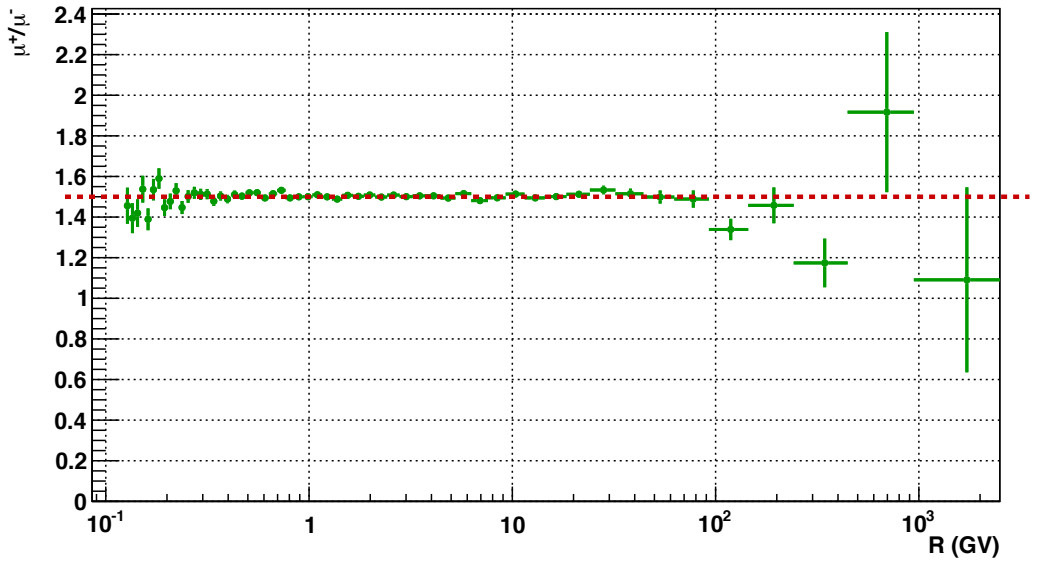

Figure 3.13: MC μ^+/μ^- ratio as function of rigidity. The injected ratio (1.5) line has been superimposed for comparison. Errors are only statistical (binomial).

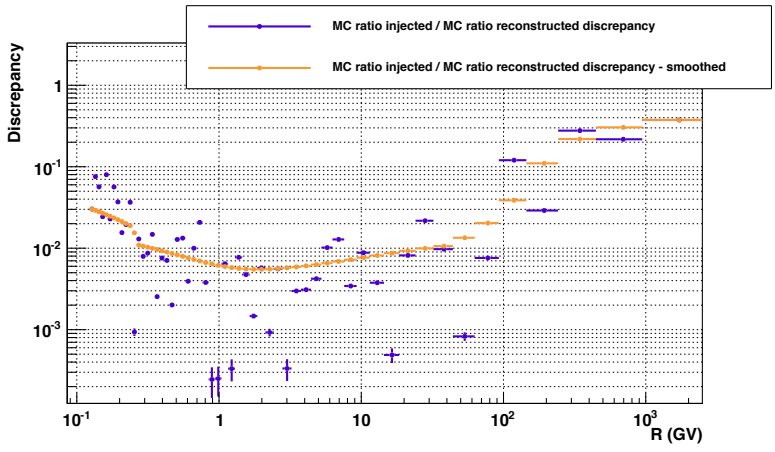

Figure 3.14: Discrepancy between ratio injected in MC and ratio reconstructed (blue). The distribution has been smoothed to remove punctual fluctuations (orange).

Chapter 4

Muon Measurements on Ground: The Data Selection

4.1 Introduction

As mentioned in § 2, the pre-flight AMS-02 commissioning was performed at KSC during the ≈ 7 months spent in the Space Shuttle Processing Facility. During that period, the integration of mechanical and electrical interfaces with the Shuttle and ISS was performed and the thermal blankets installation finalized. The DAQ commissioning proceeded in parallel to the integration activities and extended periods of data taking were planned to collect a robust statistics of muon events for calibration purposes, reaching a total of $\sim 10^3$ data taking hours with $\sim 0.3 \cdot 10^9$ registered triggers.
Due to the on-going tests, not all the collected statistics could be effectively used for muons physics analysis: in the Sec. 4.2 we will introduce in details the different data taking conditions and the criteria to pre-select the data sample used in our measurements. The event analysis will be then presented in terms of the selection criteria applied to optimize the reconstruction quality and the background rejection.

4.2 Data Period Selection

AMS-02 was delivered at KSC on August 26th. It was installed on the FP7 support structure of the SSPF and starting from August 28th there were several periods of data taking up to April 8th, when the final checkout of AMS in the payload bay of the Endeavour was performed on the launch pad. The detector was then declared *ready for launch*.
The data taking periods and the corresponding collected statistics during the KSC final integration phase are summarized in Fig. 4.1 and Fig. 4.2. Different data taking conditions were present along time as integration activities and DAQ commissioning tests were performed:

- August 28th - September 28th, 2010: the detector was switched off on a daily basis to allow for the mechanical integration activities. This corresponds

to short data taking periods, with a maximum of $\sim$ 10 hours of continuous operation. As a consequence, the running conditions were not stable. For example in Fig. 4.3 shows the tracker temperature and the corresponding distribution of clusters in a period of short data taking sessions;

- September 30th - October 7th, October 8th - November 1st, 2010: the detector was installed on the rotating structure (FP5), see Fig. 4.4 to finalize the installation of the mechanical interface to the ISS. This corresponds to data taking with AMS pointing to the horizontal direction ($\sim$ 30 hours) and at 12° ($\sim$ 330 hours) from the zenith;

- after the re-installation of AMS on the FP7 structure, two main periods of operations with continuous data taking were scheduled between November 9th and December 6th, 2010. Detectors were continuously powered with quite stable working conditions. We therefore concentrated our analysis on the statistics accumulated in this period, selecting in this time frame the sub-sample with stable DAQ conditions as described later. In this period 649 runs were collected, corresponding to $\sim$ 250 hours of data taking and $\sim 7.5 \cdot 10^7$ triggers;

- data taking in December and January 2011 and during the final checkout on April 8th was specifically devoted to DAQ tests and verification of communication through the Shuttle and ISS interfaces. Even if extremely important for final commissioning of the run procedures, the data were collected under different conditions and only marginally useful for physics analysis.

4.2.1 Run selection

The selection of a data sample with stable detector conditions and uniform data taking settings has been the first step of the analysis. The AMS data taking is subdivided in the so called "runs", $\approx$ 30 minutes of continuous acquisition interleaved by calibrations runs and adjustments of the detector and data taking parameters when needed. The strategy implemented for this objective has been to identify a set of quantities representative of the overall quality of the data taking at the level of single runs and to create a list of bad runs to be discarded for physics analysis. Figures 4.5, 4.6, 4.7, 4.8, 4.9 and 4.10 show the behavior, as a function of the run number, of the different quantities used to create the bad run list. The corresponding selection criteria are summarized in the following:

1. Missing events: during the power on periods the complete DAQ chain from the ISS to ground was tested for the final commissioning. This introduced a seldom loss in the acquisition of triggered events, partially due to desynchronization of the DAQ nodes during the event building. Only the runs where a fraction $> 99\%$ of the triggered events was correctly dispatched were pre-selected for our analysis. This requirement reduced the sample from 649 to 621 runs.

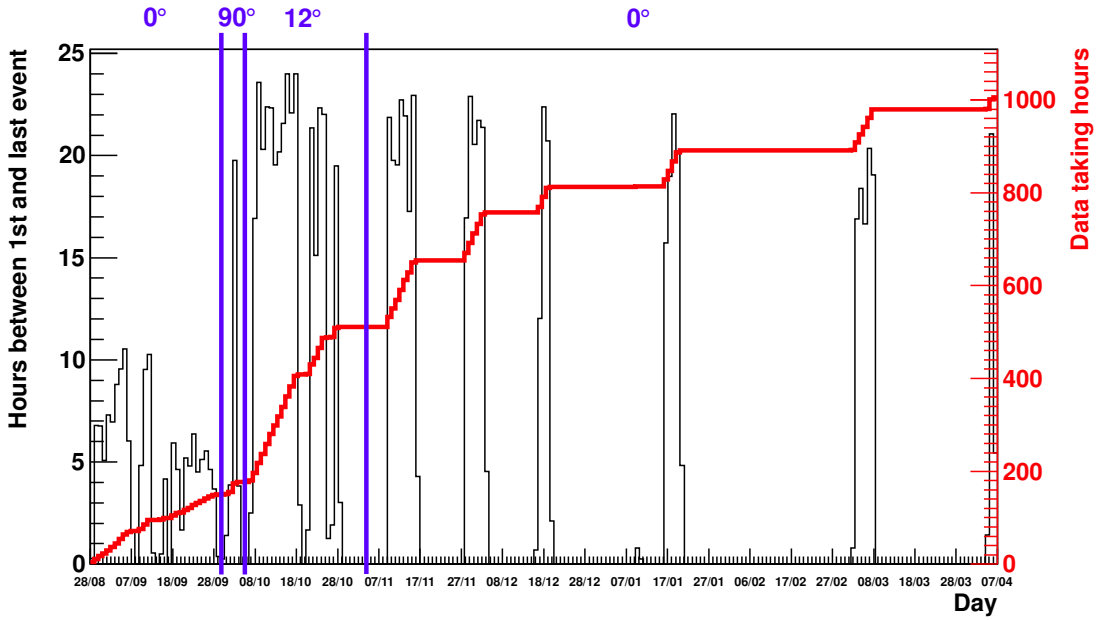

Figure 4.1: Total amount of data taking hours per day (black) and cumulative (red, vertical scale on the right) in the period August 28th August, 2010 - April 08th, 2011. For the whole period, AMS-02 was pointing toward the zenith except for two periods in September and October (horizontal and 12° w.r.t the zenith). The total amount of data taking is $\sim 10^3$ hours.

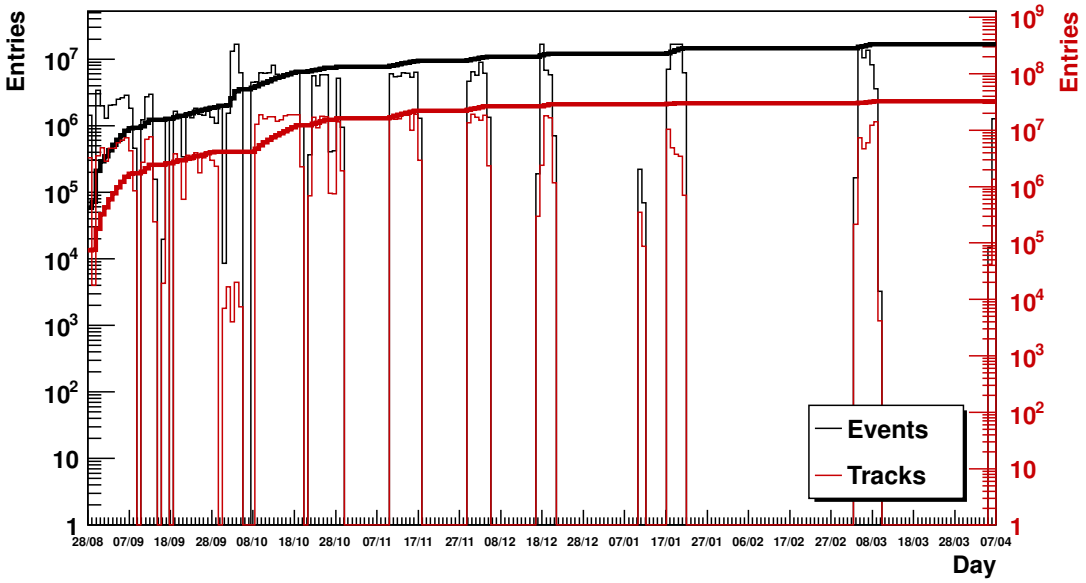

Figure 4.2: Total amount of events triggered (black) and with a Tracker track (red) per day and cumulative (vertical scale on the right) in the period August 28th, 2010 - April 8th, 2011. The total amount of triggers in the whole period is $\sim 0.3 \cdot 10^9$.

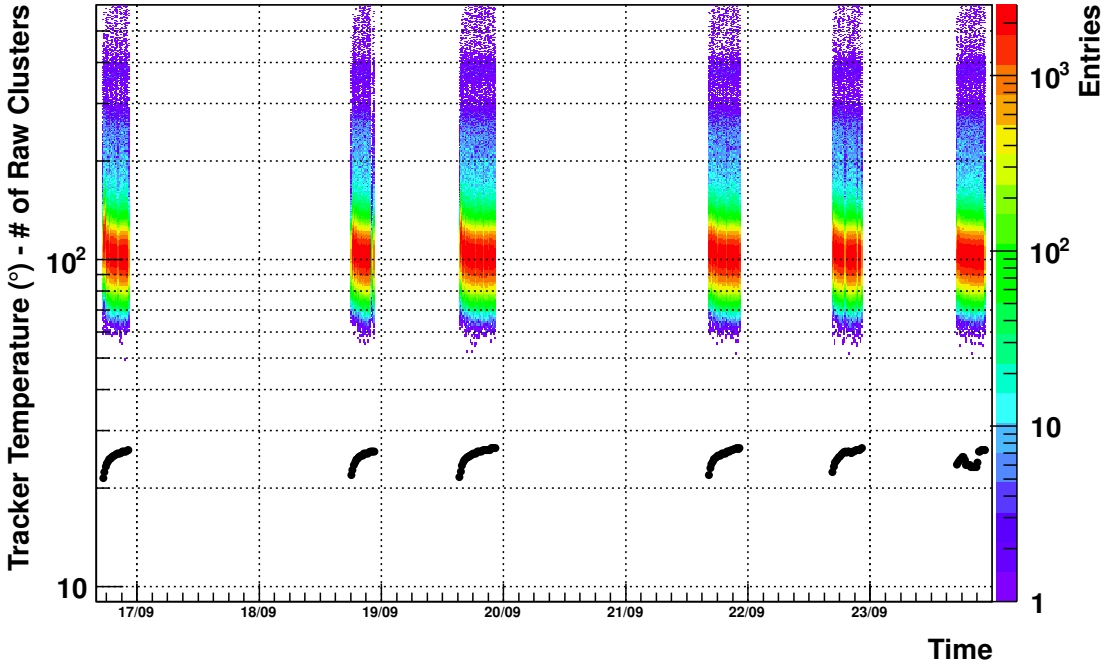

Figure 4.3: Distribution of the tracker raw clusters number (colored) and Tracker internal temperature (black line, superimposed) as a function of time. During short data taking periods the temperature is not stable inducing a variation on the average number of raw clusters

Figure 4.4: AMS-02 installed horizontally on the rotating structure FP5 in the SSPF at KSC, in the October 2010.

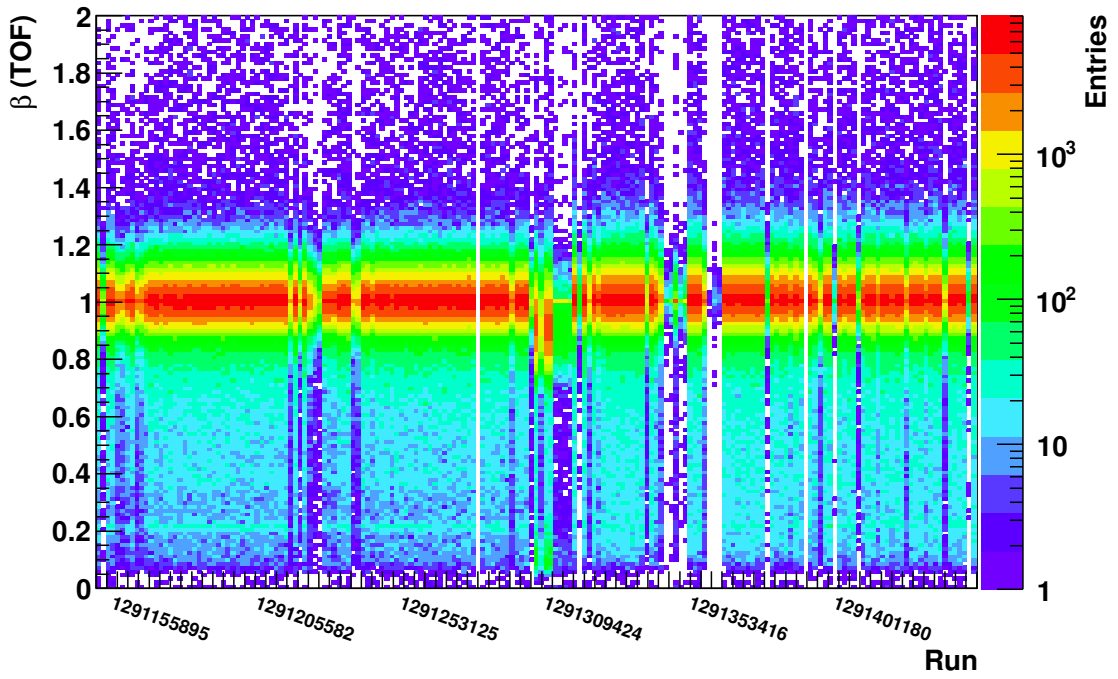

Figure 4.5: Distribution of the β measured by TOF for downward-going particles as function of the run number. Runs with a not calibrated TOF are easily recognizable (for example few runs around the 1291309424) and have been removed from the analysis sample.

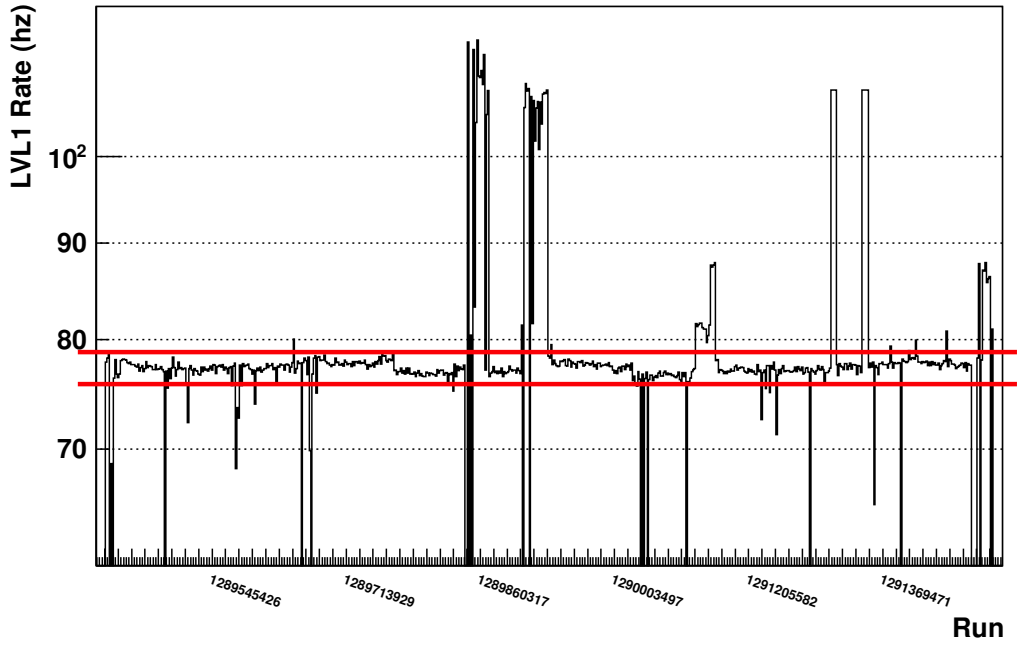

Figure 4.6: Distribution of the LVL1 Rate, averaged over the run, as a function of the run number.

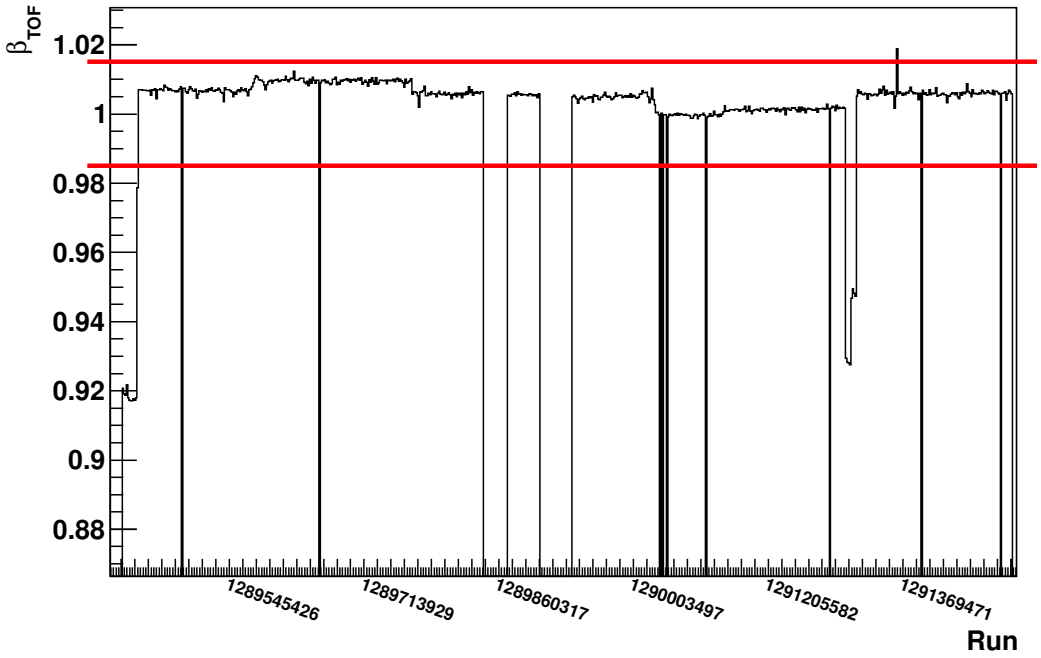

Figure 4.7: Distribution of the β measured by TOF for downward-going particles, averaged over the run, as a function of the run number.

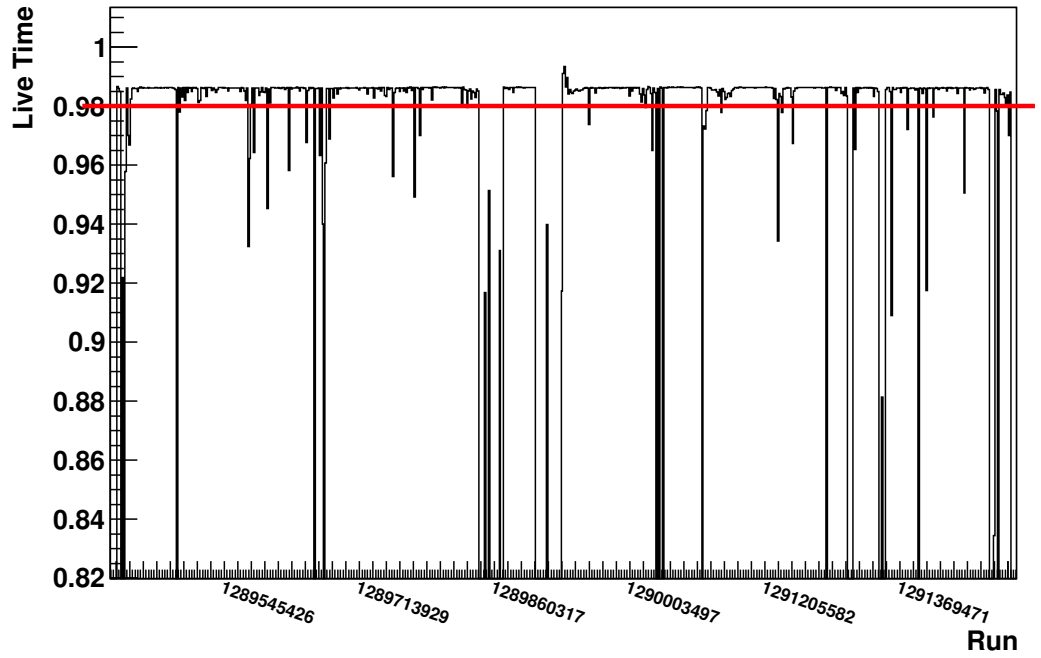

Figure 4.8: Distribution of the Live Time, averaged over the run, as a function of the run number.

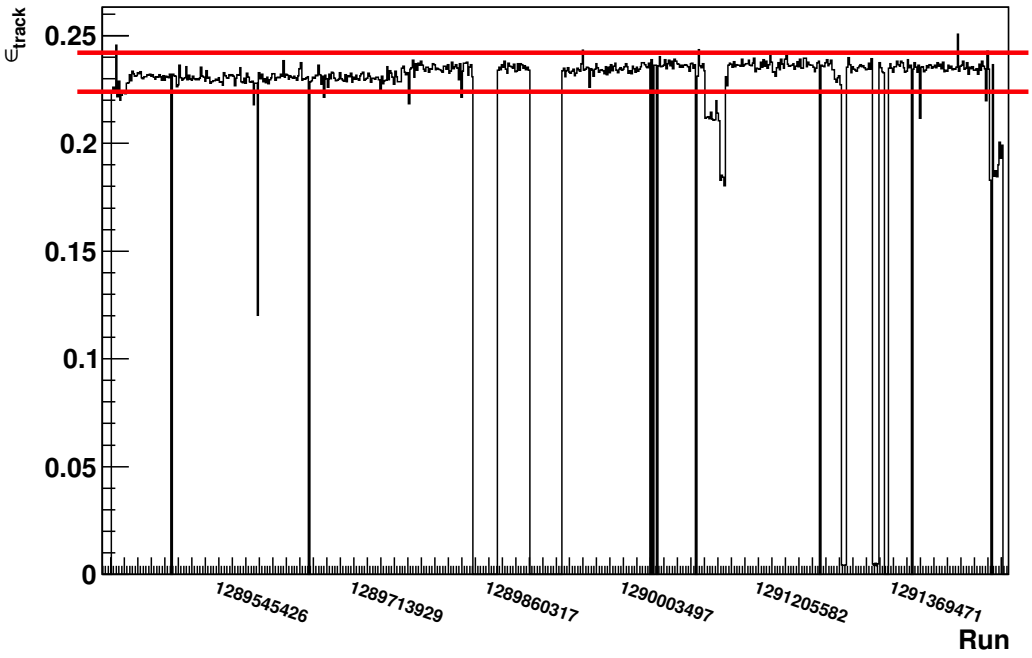

Figure 4.9: Distribution of particles with track reconstruction efficiency, averaged over the run, as a function of the run number.

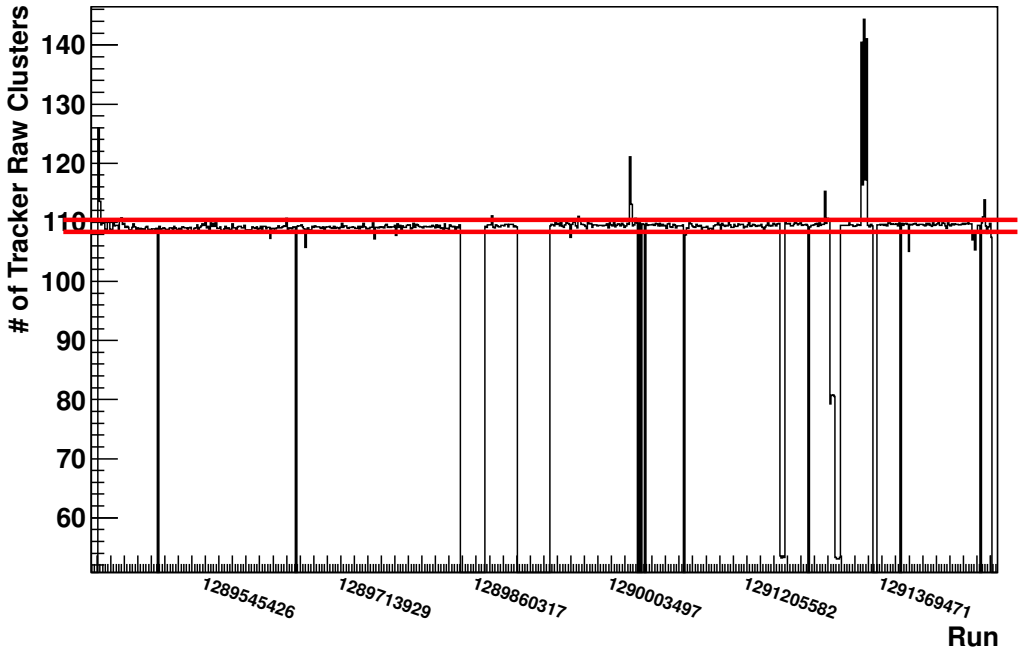

Figure 4.10: Distribution of the number of Raw Clusters in Tracker, averaged over the run, as a function of the run number.

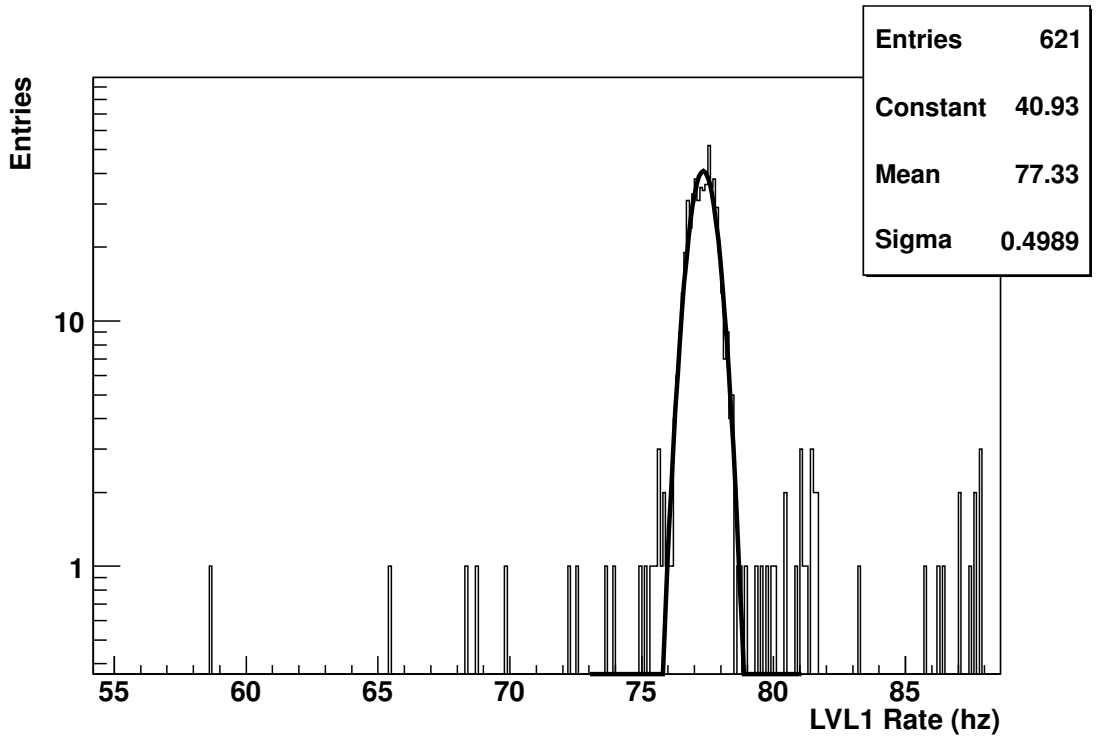

Figure 4.11: Distribution of the LVL1 Rate in the run sample. Only the runs with a LVL1 rate of 77.3 ± 1.5 Hz are kept for the analysis. This reduces the sample from 621 to 530 runs.

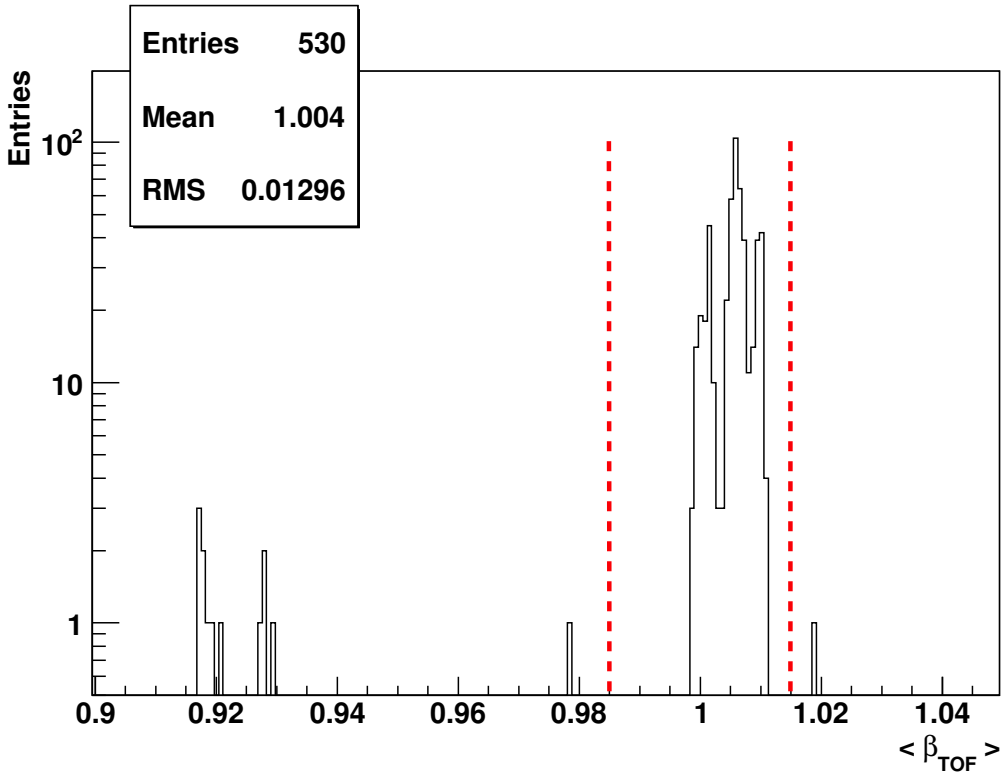

Figure 4.12: Distribution of the β measured by TOF and averaged over the run. Only the runs with a $< \beta_{TOF} >$ of 1 ± 0.015 are kept. This reduces the sample from 530 to 512 runs.

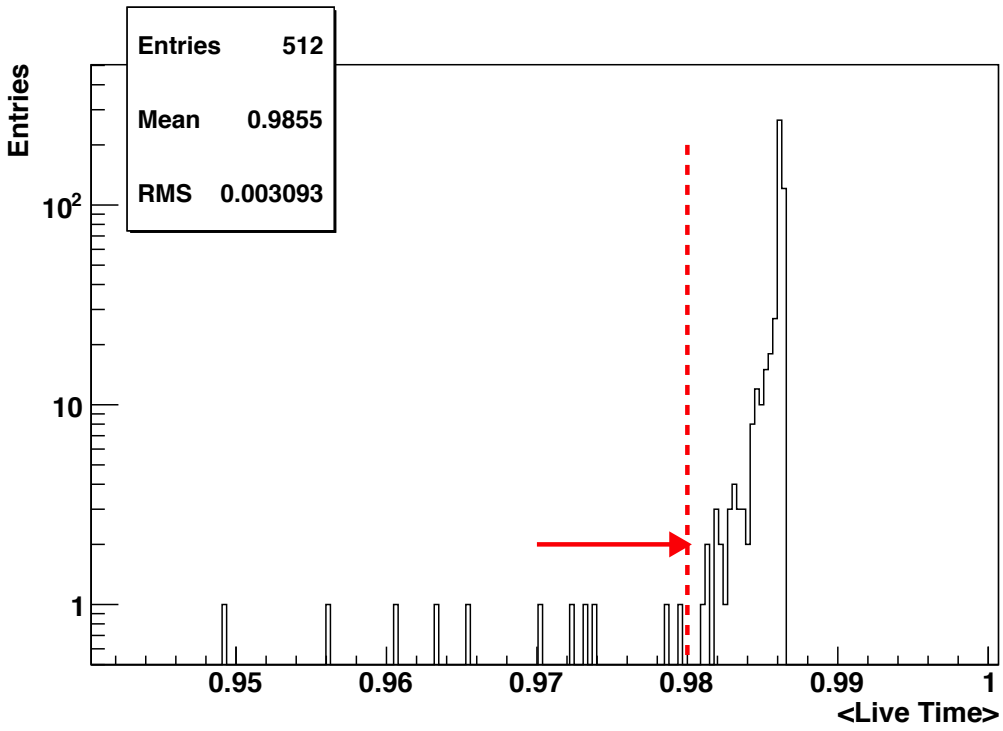

Figure 4.13: Distribution of the LiveTime measured by JLV1 and averaged over the run. Only the runs with a <LiveTime> greater than 0.98 are kept. This reduces the sample from 512 to 501 runs.

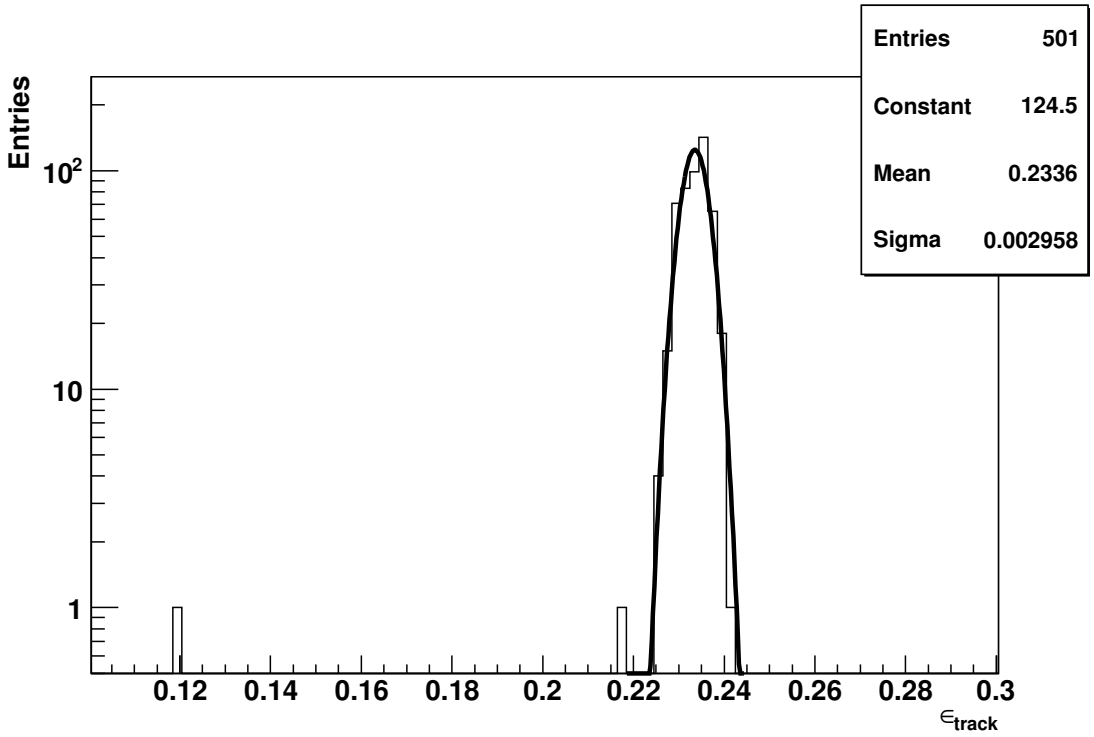

Figure 4.14: Distribution of the ratio between the number of particle with a track and the number of trigger. Only the runs with a particle with a track efficiency of 0.234 ± 0.009 are kept. This reduces the sample from 501 to 498 runs.

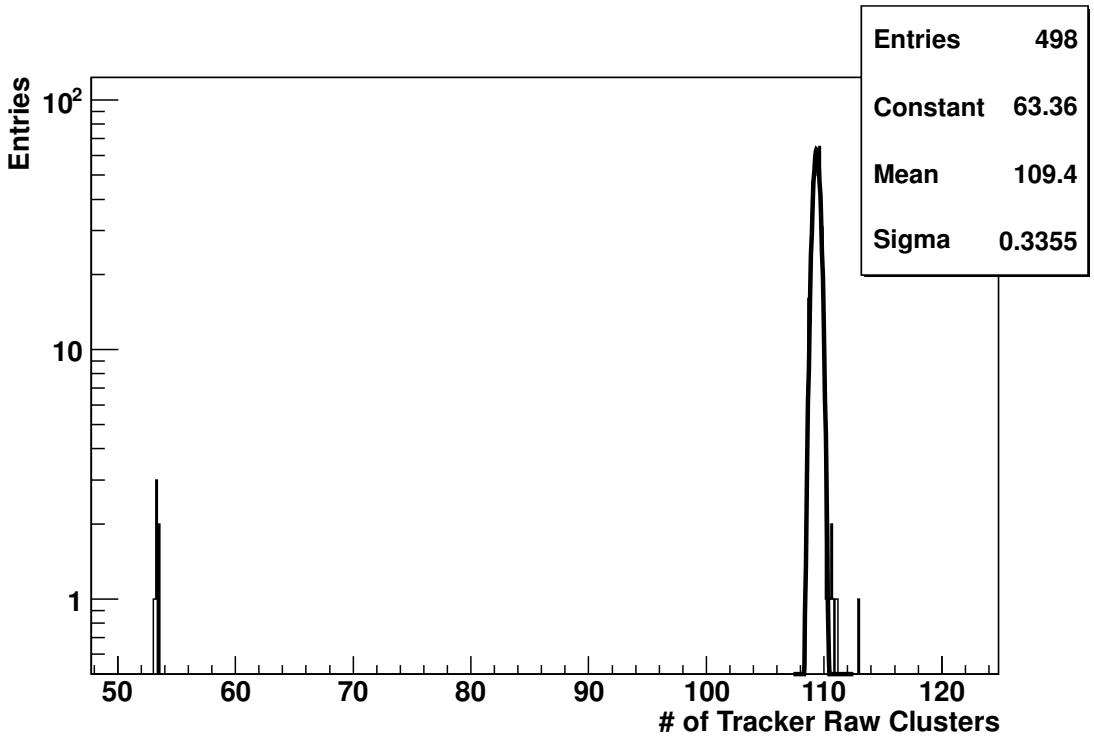

Figure 4.15: Distribution of the number of Raw Clusters in Tracker, averaged over the run. Only the runs with a mean of 109.4 ± 1 are kept for analysis. This reduces the sample from 498 to 484 runs.

2. LVL1 rate: during the data taking, the trigger configuration was sometimes changed for short periods to perform particular tests. Only the runs with the same trigger conditions (i.e. the same LVL1 rate, see Figs. 4.11 and 4.6) have been kept. This requirement reduced the sample from 621 to 530 runs.

3. $< \beta_{TOF} >$: due to the varying HV configurations along the different tests, the Time of Flight response was not calibrated over the whole period. This produced a sizeable bias on the measurement of the particle velocity. The average β distribution for high rigidity particles in the different runs was used to identify and discard the periods with a β measurement not compatible with the unity (see Figs. 4.12 and 4.7). This selection reduced the sample from 530 to 512 runs.

4. <LiveTime>: part of the tests on the DAQ procedures at the level of the AMS main computer (JMDC) were affecting the experiment LiveTime. Only the runs with an average LiveTime greater than 0.98 have been selected (see Figs. 4.13 and 4.8) reducing the sample from 521 to 501 runs.

5. Particle reconstruction efficiency: runs with tracker tests could potentially affect the track reconstruction. The distribution of the average track efficiency, defined as the fraction of events with a reconstructed particle with track over the total number of triggers in a run, was used to identify and

discard test runs. Figs. 4.14 and 4.9 show the track efficiency distributions and the applied selection which reduced the sample to 498 runs.

6. Tracker raw clusters: to guarantee homogeneous tracker data taking conditions against different settings of the TDR compression thresholds, the average number of raw clusters per event as a function of the run was finally verified and 14 runs further rejected as depicted in Figs. 4.15 and 4.10).

4.3 The event selection guidelines

The identification of well measured muons in the detector and the rejection of background particles are the objectives of the event selection. As will be shown in details in §5 , the flux measurement implies a detailed knowledge of the detector acceptance which results from the combined effect of the geometrical acceptance, the reconstruction and selection efficiency. The geometrical acceptance of a complex detector as AMS-02 can be assessed only by Monte Carlo techniques; however the approach followed through all the data analysis has been to choose, whenever possible, selection criteria whose efficiency could be safely estimated in the data sample.
The efficiency of each single cut has been studied on both DATA and MC both as a function of Rigidity (R) and of the zenithal incidence angle θ as reconstructed with the Silicon Tracker according to the following definition:

$$\varepsilon(R_{Tk}, \theta_{Tk}) = \frac{N_{cut}(R_{Tk}, \theta_{Tk})}{N(R_{Tk}, \theta_{Tk})} \tag{4.1}$$

where N_{cut} are the events passing a given selection criteria over the sample of N events.
The average discrepancy between MC and DATA has been used to correct the MC estimation of efficiency, whereas dependencies of the efficiencies ratios on R and θ have been used to assess the systematic error associated to the applied corrections.

To study the track reconstruction efficiency itself an independent estimator of a particle crossing through the detector is needed. Based on the fact that all charged triggers have a signal in the TOF system, a coarse indication of the particle path build from the TOF signals - called in the following "TOF Road" - has been used to verify the tracker performance.

TOF Road: Charged particles passing through the TRACKER acceptance should be accompanied by four TOF clusters, one per layer. A 3D measurement of the particle crossing point can be associated to each cluster. Coordinates along x (y) are determined in planes 1,4 (2,3) from the TOF paddles segmentation with a resolution of $\sim 3\,\mathrm{cm}$[1] which is reduced to $\sim 1\,\mathrm{cm}$ in the overlap regions. Coor-

[1] it is defined as the standard deviation related to an uniform distribution over the paddle width

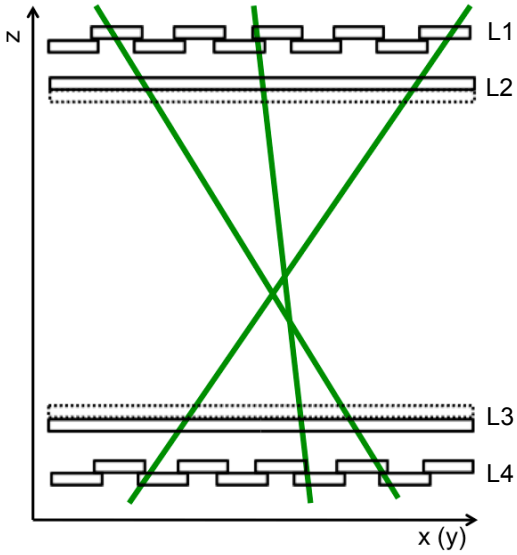

Figure 4.16: The information from the 4 TOF planes (positional from 2 planes and temporal from the other 2) are used to build a "road" for the particles just using TOF signals.

dinates along the paddle length are measured from the difference in time of the signals collected at the two ends of the paddle, with a typical resolution of $\sim$ 3 cm. The z coordinate is defined by the nominal position of the paddle center in the AMS-02 reference system, with an error assumed to be negligible (0.3 cm) in the definition of the TOF Road.
Neglecting the curvature in the magnetic field, which gives a sagitta well within the spatial resolution of the TOF, a least squares straight line fit was used to define the particle trajectory for the $x-z$ and $y-z$ views independently. In the events where multiple clusters were found in TOF planes, the "road" was reconstructed choosing the combination of the 4 clusters that gave the minimum χ^2's sum on the two views.

The angular matching between TOF roads and tracks fully reconstructed with the silicon TRACKER has been verified on DATA and with the generate particle direction in MC, allowing to estimate a resolution $< 2^\circ$ in the zenithal angle θ measurement with TOF, as shown in Figs. 4.17, 4.18.

The TOF road has been used to evaluate as a function of the zenithal angle the efficiency of track reconstruction (see 4.4.5) as :

$$\varepsilon(\theta_{TOF}) = \frac{N_{cut}(\theta_{TOF})}{N(\theta_{TOF})} \tag{4.2}$$

being N_{cut} the number of events having a reconstructed TRACKER track in the sample of N events where a TOF road could be defined at a given step of the analysis.

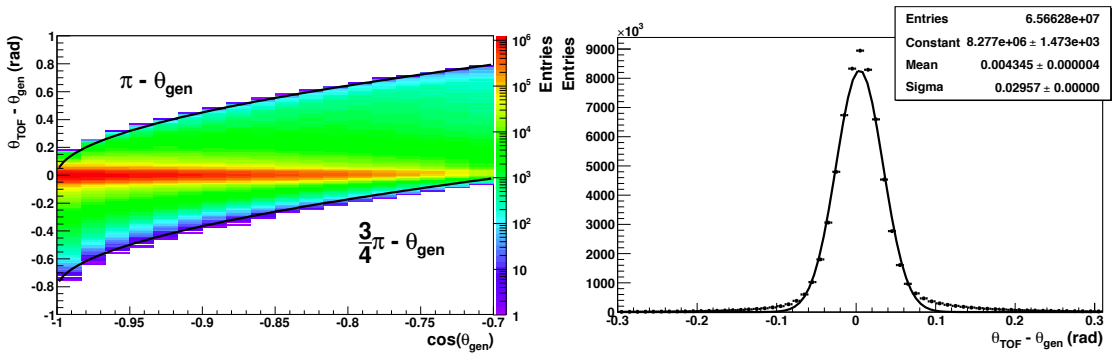

(a) (b)

Figure 4.17: Difference between the incidence angle θ of the particles reconstructed by TOF road and generated in MC. (a) As function of cos(θ_{gen}): the bad reconstructed trajectories with TOF are constrained between π and $\sim \frac{3}{4}\pi$, being approximately the dimension of the sides of the TOF planes equal to the distance between the Upper-TOF and the Lower-TOF. (b) Cumulative: the resolution is $\sim$ 30 mrad (1.72°).

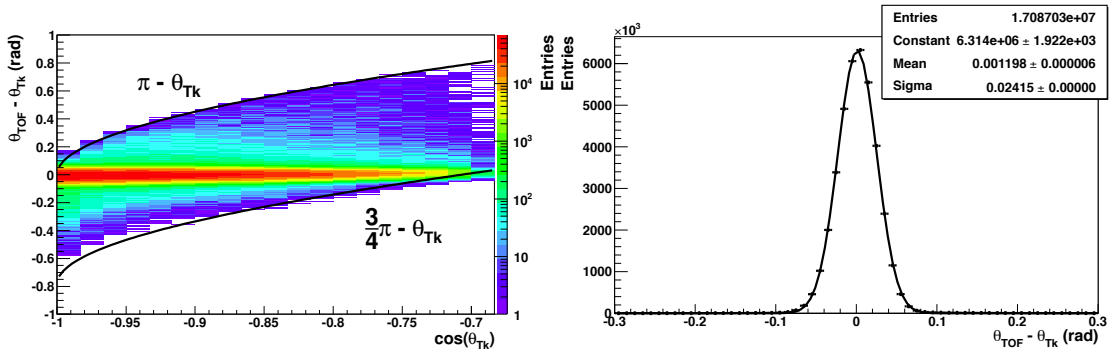

(a) (b)

Figure 4.18: Difference between the incidence angle θ of the particles as determined with the TOF road and Tracker. (a) As function of cos(θ_{Tk}): the bad reconstructed trajectories with TOF are constrained between π and $\sim \frac{3}{4}\pi$, being approximately the dimension of the sides of the TOF planes equal to the distance between the Upper-TOF and the Lower-TOF. (b) Cumulative: the resolution is $\sim$ 24 mrad (1.38°)

4.4 The Event selection criteria

In the following all the criteria used in the muon sample selection will be described in the detail. They may be grouped in three main categories involving different aspects of the analysis:

Pre-selection cuts: tightening of the trigger condition at the very beginning of the data selection has been applied in order to get rid of events either related to background atmospheric particles (electrons, interacting protons) or marginally contained in the tracker acceptance. Even if these cuts were not strictly needed, these events would be anyhow discarded at later stages of the analysis, this step allowed to *clean* the sample and to have a better comparison of the efficiencies with the MC sample.

Reconstruction quality: only events where one single particle with a velocity measurement from TOF well matched with a single reconstructed track in the TRACKER have been considered for the muon analysis (see 4.4.6). Both for the TRACKER and the TOF measurements, specific requirements on the particle pattern in the detectors were required in order to keep events with the maximal resolution (see Secs. 4.4.7 and 4.4.8).

Background rejection: particle interactions in the upper part of detector are a source of "internal" background whenever the reconstructed particle is not the primary muon but a secondary pion or electron. Most of this background is efficiently removed by the pre-selection and reconstruction quality cuts. Additional requests on the activity in the TRD (see Sec. 4.4.9) and on the reconstructed particle mass (see Sec. 4.4.10) were applied to further reduce this component. The mass cut was also effective to cope with the "external" physical background, O(1%) of protons and O(‰) of electrons/positrons, up to $\sim$ 1 GeV.

4.4.1 Trigger

The trigger conditions used during the KSC data taking were varying along time, depending on the input trigger rate needed in the DAQ commissioning tests. However, in the preselected run sample, all data were registered by one of the trigger conditions listed below (see Sec 2.2.10):

SUBLVL-0 Charged particles: TOF 3/4 (HT), any number of ACC fired;

SUBLVL-1 Electromagnetic particles (ECAL standalone): `ECAL-A_or`

For the selected KSC data taking period the $\sim$ 99.6 % of triggers was taken exclusively by the SUBLVL-0 and just a $2.7 \cdot 10^{-6}$ % by both the triggers inclusively. The remaining part (exclusive SUBLVL-1) has been removed from the analyzed sample. The exclusive ECAL standalone trigger is designed to select photons but is also sensitive to electrons and energetic protons entering the calorimeter out of the charged trigger acceptance. The background selected by the ECAL standalone trigger is not simulated in the MC and its rejection in the early stage of

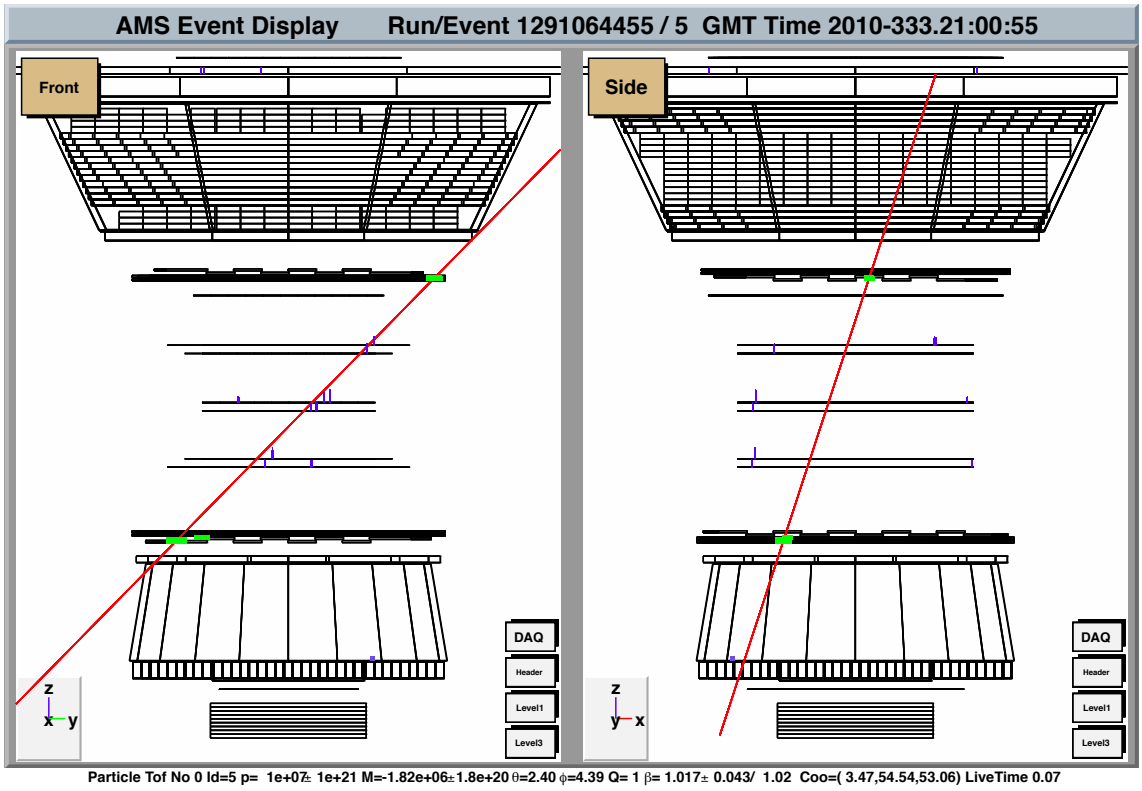

Figure 4.19: A Time of Flight 3 out of 4 event. These events, usually, are very inclined events. The fraction of 3 out of 4 events due to Time of Flight inefficiency are less then 3‰.

the analysis is convenient for the DATA-MC comparison of selection efficiencies. In fact, all SUBLVL-1 exclusive events would have been rejected in the other steps of the selection process as verified by applying the same request as "Last Cut" in the selection process.

4.4.2 Number of Time of Flight planes giving trigger

The SUBLVL1-0 trigger condition was tightened in this analysis by selecting only the events where all the four TOF planes were fired in the trigger. Nearly 25% of the triggered events were rejected by this request. These events correspond to inclined particles, out of the tracker acceptance and not simulated in the main MC sample, where as the fraction of events rejected due to TOF inefficiency is expected to be at the few permille level. A typical event with only 3 out of 4 TOF planes fired in the trigger is shown in Fig. 4.19.
The effect of this request was checked both on DATA and MC as "Last Cut" in the selection chain. In Fig. 4.20 the relative abundances of every single combination of TOF layers giving trigger are shown after all the other selection requests have been applied: the 4 out of 4 TOF planes request removes less than 3 ‰ of events in both DATA and MC.

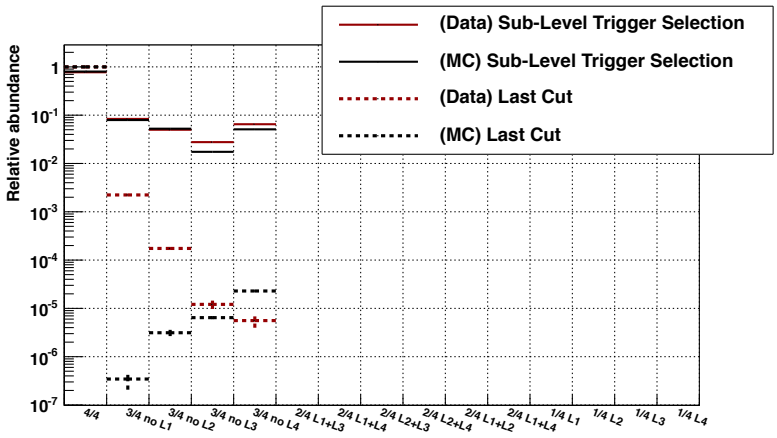

Figure 4.20: Relative abundances of every single combination of TOF layers giving trigger. DATA (red) and MC (black) are shown. The abundances are presented as they are after the sub-level trigger selection (full lines) and at Last Cut (dotted lines). As Last Cut the 4 out of 4 request removes less than 3‰ of events in both DATA and MC.

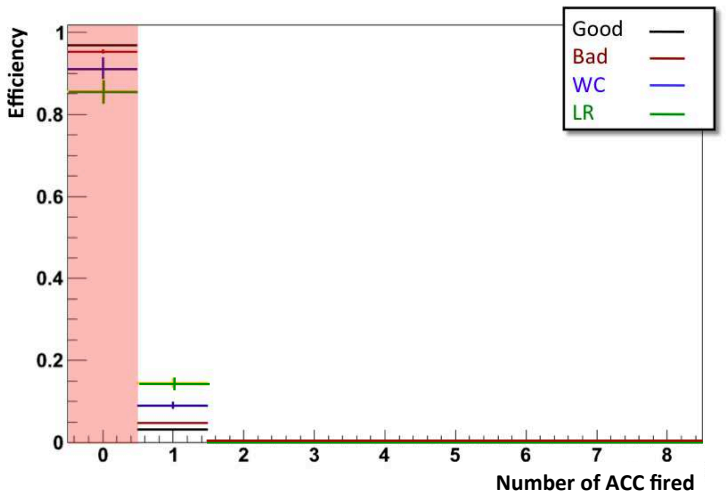

Figure 4.21: Cut efficiency on MC categories with respect to number of ACC fired. Asking for 0 ACC fired removes less than 5% of "Good" events but $\sim$ 10% for "Wrong Charge" and "Low Reco".

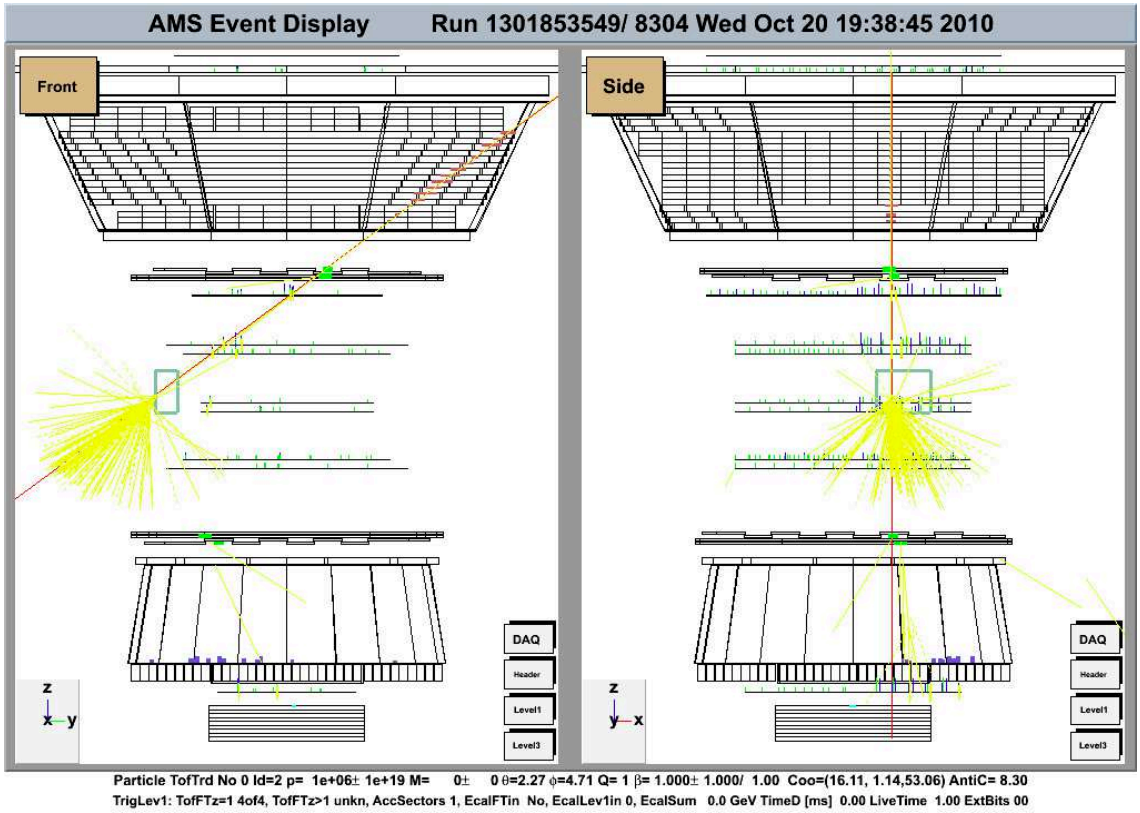

Figure 4.22: A 1 ACC fired event. The events shown is taken from a dedicated MC (θ not limited to 45°). A very inclined muon interacts in the tracker side after firing the ACC. Some of the secondary particles go towards the lower Time of Flight and the 4 out of 4 trigger condition is satisfied. The event is not accompanied by high activity in TRD or TOF. Even in the Silicon Tracker the activity is quite normal.

4.4.3 Number of ACC fired

The Anti Coincidence system for AMS-02 has been designed mainly to remove particles entering laterally the Silicon Tracker but is useful also to remove "spurious" events due to interactions. An event of this kind, as example, is shown in Fig. 4.22. The event has been observed in a dedicated MC production (θ not limited to 45°). A very inclined muon interacts in the tracker side after firing the ACC. Some of the interaction particles produced in the interactions reach the lower Time of Flight planes allowing the generation of a 4 out of 4 trigger. The event is not accompanied by high activity in TRD or TOF. Even in the Silicon Tracker the activity is quite normal.
To perform a first removal of the events with interactions all the events with a number of fired ACC greater than 0 has been removed. $\sim$ 25% of triggered events were discarded by this request, however, most of them were not good candidates for physics analysis. The effect of the cut on MC has been evaluated with the technique described in Sec. 3.5 and is shown in Fig. 4.21: asking for 0 fired ACC removes less than 5% of "Good" events but $\sim$ 10% for "Wrong Charge" and "Low Reco".

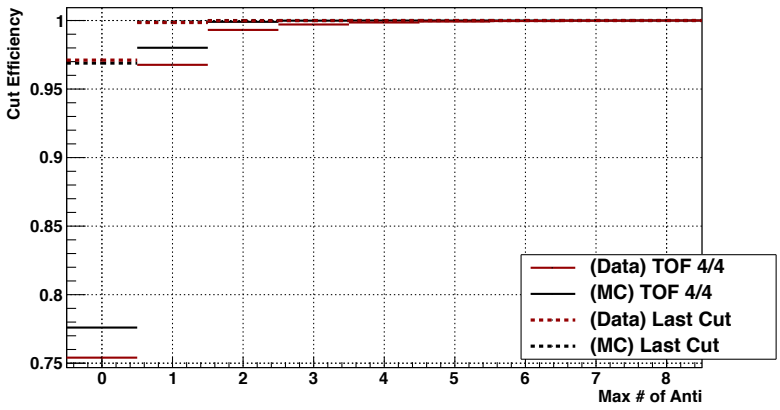

Figure 4.23: Cut efficiency as function of max number of ACC sectors fired. Efficiency in DATA (red) and MC (black) are shown. Efficiencies are presented as they are after the TOF 4 out of 4 selection (full lines) and at Last Cut (dotted lines). The DATA - MC discrepancy at Last Cut is $\sim 2\,‰$.

The cut efficiency has been evaluated as "Last Cut" to be 97%, with an agreement between DATA and MC at the $\sim 2\,‰$ level.

4.4.4 Number of velocity measurements in Time of Flight

The measurement of β with the TOF is made with a linear fit on the temporal information given by the TOF paddles. The number of clusters reconstructed in the TOF can be different from the number of planes fired in the trigger, in particular it can be larger than four when multiple hits are found in the same TOF layer. Due to the differences in term of requests between the reconstruction software and the hardware trigger logic, it can also happen that no reconstructed clusters are found on paddles which contributed to the trigger.
During the event reconstruction, the β reconstruction algorithm performs the temporal linear fit for each combination of TOF recorded clusters selecting the β candidates based on the χ^2. First the combinations matching geometrically the tracks given by Tracker and/or TRD (when available) are considered and then all the other combinations. For very low β (below 0.4) only the internal planes of TOF (2,3) are used to avoid the energy losses into the plastic scintillator.
Several β candidates can be found in each event. In this analysis only the events with one single β candidate are kept. The efficiency of this requirement has been investigated in the MC and DATA samples within the angular range matching the geometrical acceptance of the full tracker with the technique described in Sec. 3.5.
The effect of this request on the events having one single track reconstructed in tracker (see 4.4.5) is reported in Figs. 4.24, 4.25(a) as a function of the rigidity and the incidence angle respectively. Overall, the single β request shows an efficiency larger than 99.9%, both on DATA and MC samples, however at rigidities below 1 GV different behaviors are observed in DATA and MC.

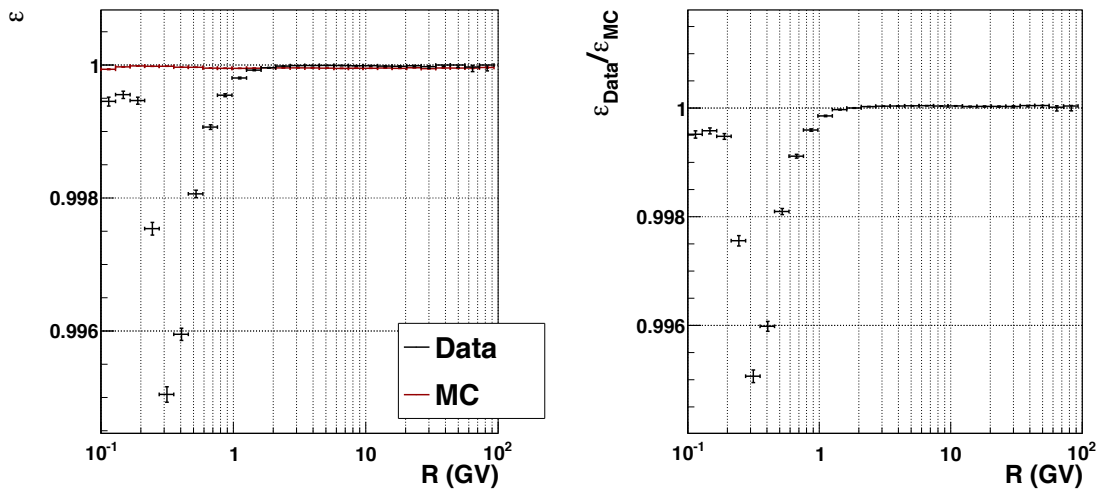

(a) (b)

Figure 4.24: a) Efficiency of the "1 single β" request in DATA (black) and MC (red). b) Ratio between DATA and MC efficiencies. At low rigidities the DATA efficiency is not flat and the discrepancy DATA - MC reaches 0.5%.

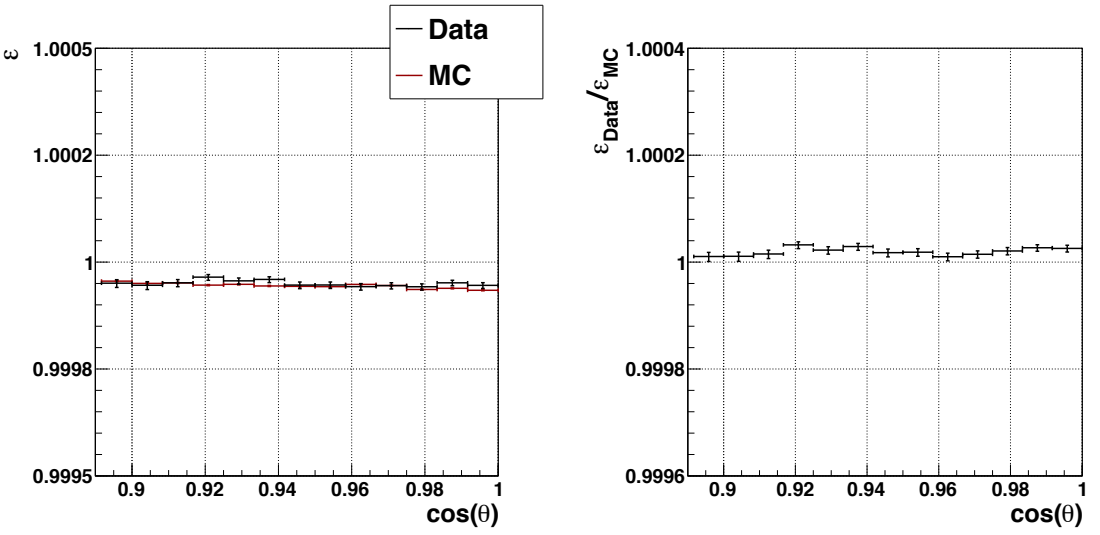

(a) (b)

Figure 4.25: a) Efficiency of the "1 single β" request in DATA (black) and MC (red). b) Ratio between DATA and MC efficiencies.

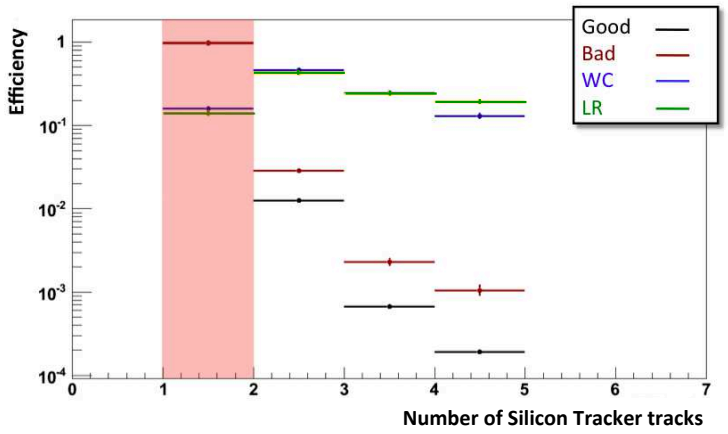

Figure 4.26: Cut efficiency on MC categories with respect to number of reconstructed Tracker tracks. Asking for 1 Tracker track removes $\sim$ 85% of "Wrong Charge" and "Low Reco" events keeping $\sim$ 99% of "Good" ones.

Both as function of rigidity (above 1 GV) and as function of incidence angle the DATA - MC discrepancy has a value of:

$$C_{OneBeta} = 1.00001 \pm 0.00001$$

At low rigidities the DATA efficiency is not flat and the discrepancy DATA - MC reaches 0.5%.

4.4.5 Number of tracks in Silicon Tracker

The basic signature of a single charged particle passing through AMS-02 is to have one single track reconstructed in the Silicon Tracker associated to a β measurement in the TOF. Before any requirement on the track pattern, i.e. on the number of layers used for the reconstruction, the effect of requiring a single track reconstructed was studied, on DATA and MC.
The largest effect in the track reconstruction efficiency comes from the large geometrical acceptance of the TOF system with respect to the tracker: a $\sim$ 25% of the trigger events are expected not to be reconstructed in the tracker, i.e. to give 0 tracks in the detector, with a strong dependence on the particle incident angle. A few percent of the events is also expected to have more than one reconstructed track, due to interactions in the detector. The behaviour of this cut against misreconstructions has been investigated on the MC sample with the technique described in Sec. 3.5: asking for only 1 Tracker track removes $\sim$ 85% of "Wrong Charge" and "Low Reco" events keeping $\sim$ 99% of "Good" ones, as shown in Fig. 4.26. The events removed by this cut (i.e. "Low Reco") are due to interactions inside the upper part of the detector and will be shown clearly in Sec. 4.4.10.
To study the efficiency of the cut, on both DATA and MC, the TOF has been used to perform an independent evaluation of the particle direction and momentum. From

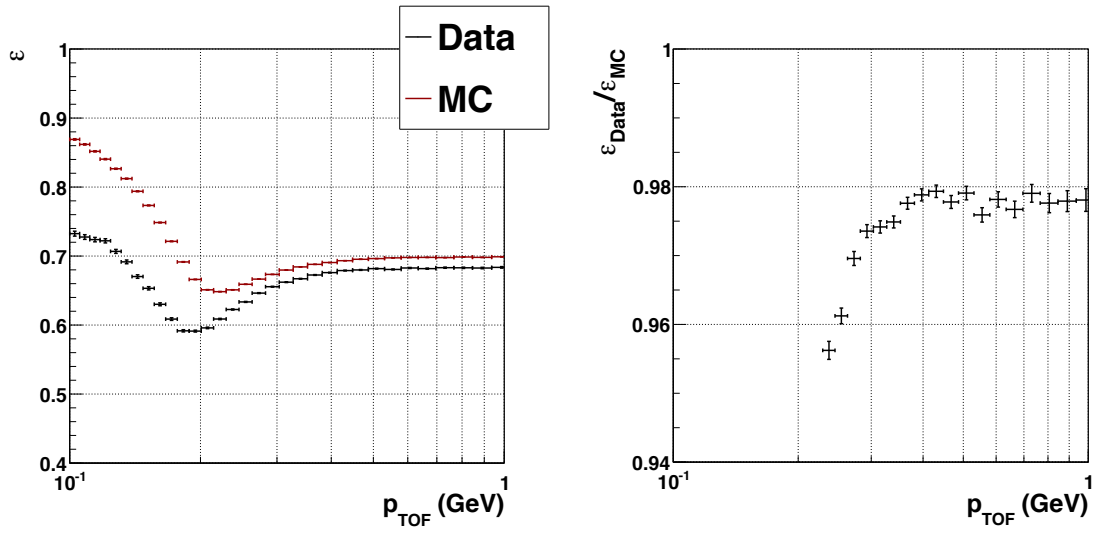

(a) (b)

Figure 4.27: a) Efficiency of the "1 single track" request in DATA (black) and MC (red) as function of momentum (evaluated from the β measured in the TOF). b) Ratio between DATA and MC efficiencies. Below 0.4 GeV the DATA - MC discrepancy grows up.

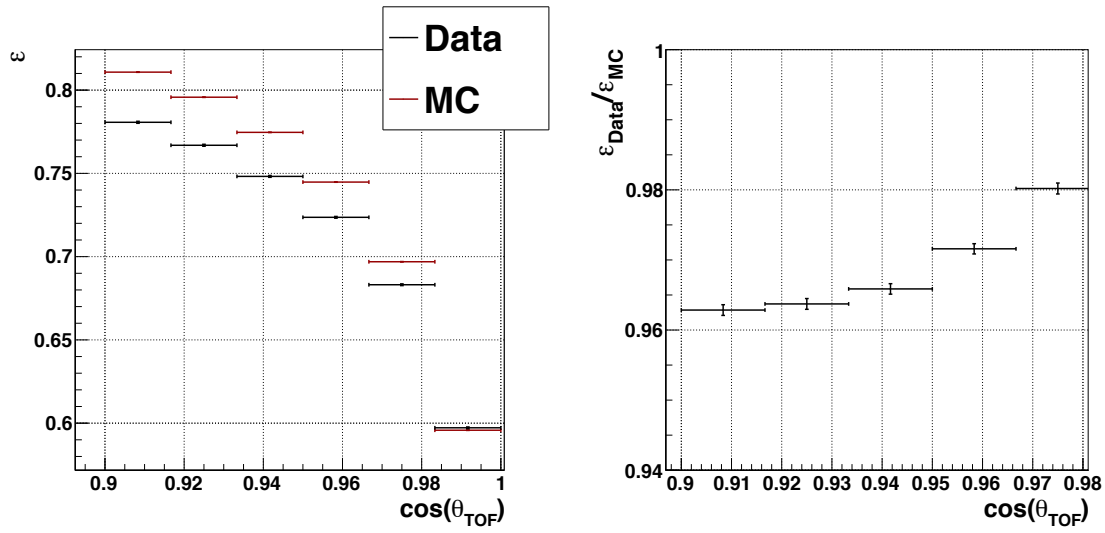

(a) (b)

Figure 4.28: a) Efficiency of the "1 single track" request in DATA (black) and MC (red) as function of incidence angle (given by TOF Road) for p_{TOF}>0.4 GeV. b) Ratio between DATA and MC efficiencies.

the β measurement, assuming the muon mass, is possible to study the efficiency of cut as function of momentum measured by TOF:

$$p_{TOF} = m_{\mu}\beta\gamma \tag{4.3}$$

The evaluation is possible, due to the β resolution, up to $\sim$ 1 GeV. To study the effect of the cut as function of the zenithal angle, instead, and compare the efficiency in DATA and MC, the TOF Road has been used to evaluate the particle direction.
The efficiency of the cut in DATA (black) and MC (red), as function of momentum, is shown in Fig. 4.27(a). The behaviour of the efficiencies may be interpreted in terms of the dependence with the particle velocity of the energy released in the tracker silicon sensors. The muon, indeed, is a MIP around $\sim$ 250 MeV [35]. Following the Bethe-Bloch function the energy deposit is higher both at lower energies (dE/dx $\propto 1/\beta^2$), and at higher ones due to radiative effects and radiation losses. The ratio between the two efficiencies is shown in Fig. 4.27(b) within the angular range matching the geometrical acceptance of the full tracker. Above 0.4 GeV the ratio of efficiencies is flat. At lower energies, a discrepancy is observed due to several causes: β measurement calibration, proton and electron backgrounds and the accuracy of the MC simulation.
The efficiency of the cut in DATA (black) and MC (red), as function of momentum is shown in Fig. 4.28(a), while the ratio between the two efficiencies is shown in Fig. 4.28(b), within the angular range matching the geometrical acceptance of the full tracker and for particles with a p_{TOF}>0.4 GeV.
The DATA - MC discrepancy has been evaluated to be:

$$C_{OneTrack} = 0.973 \pm 0.008$$

4.4.6 Geometrical compatibility between Silicon Tracker track and Time of Flight hits

In the AMS reconstruction, a *Normal Particle* is defined whenever a β measurement can be associated to a tracker track: matching of the two measurements requires that the TOF paddles crossed by the trajectory defined by the tracker track are the same used for the β evaluation. In most cases, the Normal particle matching fails in the xz view due to a wrong assignment of the x coordinate in resolving the hit multiplicity in the tracker, as shown in Fig 4.29.
In our analysis, the requirement of a Normal particle rejects $\sim$ 1% of the events in the angular acceptance of the full tracker, mainly at rigidities below the GV.
The efficiency of the cut has been studied in both DATA and MC as function of rigidity (see Fig. 4.30) and incidence angle (see Fig. 4.31). The DATA - MC discrepancy, above 1 GV can be quoted as:

$$C_{Normal} = 0.993 \pm 0.002$$

At low rigidities the efficiency behaviours observed in DATA and MC are not compatible. This can be due to very low rigidity background particles (physical

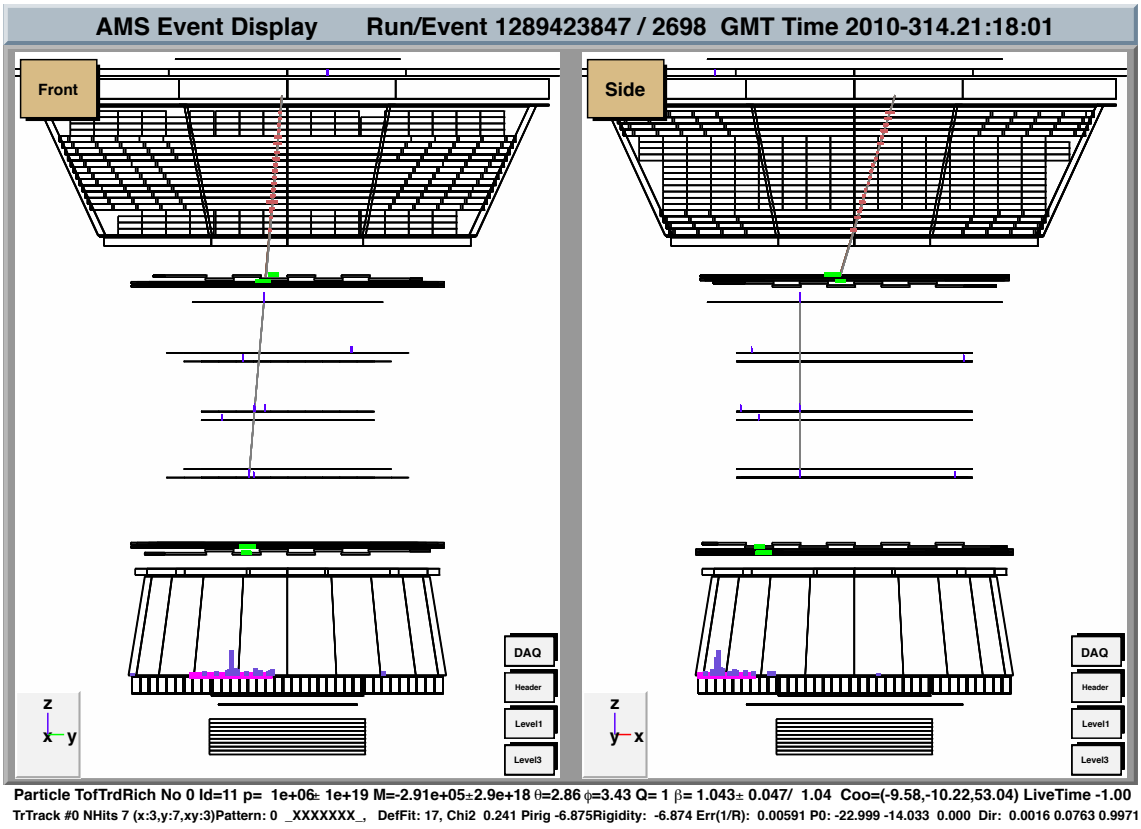

Figure 4.29: An event with only one Silicon Tracker track and only one Time of Flight β measurement, not geometrical compatible between themselves. The tracker track direction on x view is not compatible with the TOF hits. Most likely event like this are due to a wrong multiplicity resolution on ladder x-side.

protons and positrons/electrons, positrons/electrons due to interactions in the detector or in the SSPF roof) that are not simulated in the MC or, at these rigidities, the simulation is not enough accurate in describing the detector properties.

4.4.7 Tracker pattern

Depending on the lever arm used in the trajectory determination, the resolution of the spectrometer varies significantly as well as its acceptance. Within the $\sim$ 100 tracker clusters per event, the pattern recognition algorithm scans the combination of clusters that can be associated in a track starting in the inner tracker, layers 3-4 and 7-8, looking for a matching measurement in layer 2 and then adding the measurements in layers 5-6. As discussed previously, $\sim$ 75% of the triggered events have a reconstructed track, at least at the inner tracker level. However, this corresponds to a rigidity measurement over an 80 cm lever arm in magnetic field (55 cm when no hit found in layer 2) which corresponds to a $\sim$ 200 GV maximum detectable rigidity. Once the inner track has been reconstructed, its trajectory is extrapolated to search for an hit association on the external layers in order to perform the rigidity measurement over the full lever arm, $\sim$ 3 m, which corresponds to a maximum detectable rigidity of 2 TV.

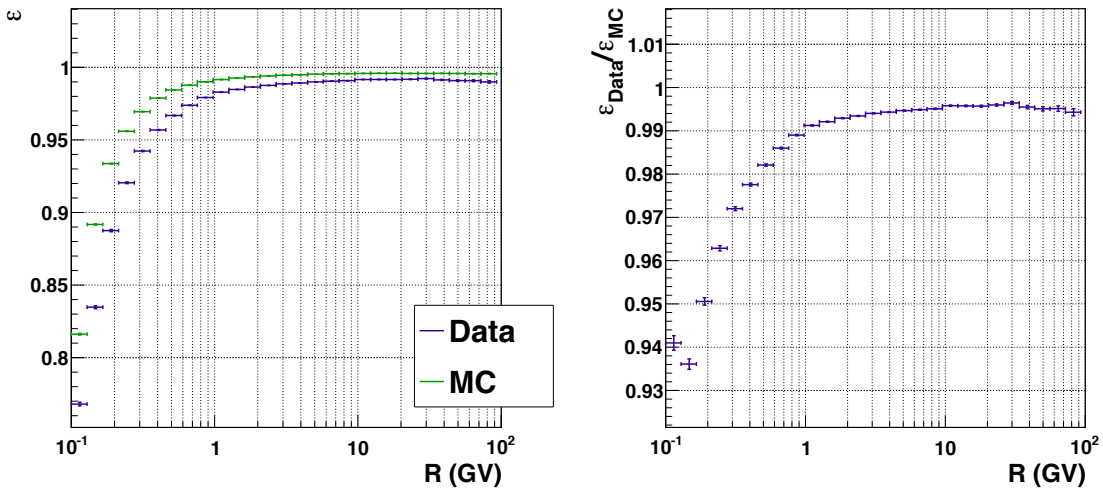

(a) (b)

Figure 4.30: a) Efficiency of the "Normal Particle" request in DATA (green) and MC (blue) as function of rigidity. b) Ratio between DATA and MC efficiencies. The discrepancy between DATA and MC is flat above 1 GV. Below the effect of background particles or not enough realistic MC lead to a more relevant discrepancy.

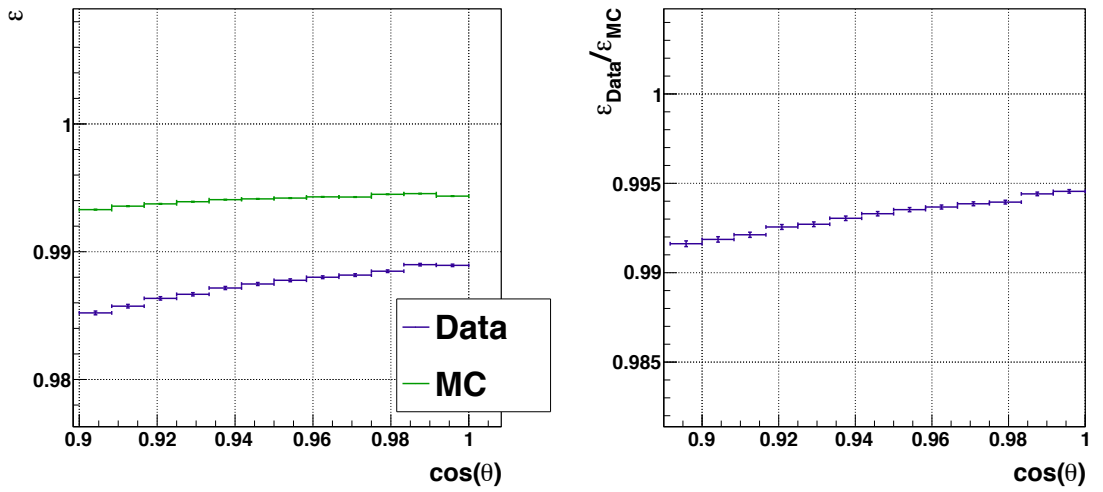

(a) (b)

Figure 4.31: a) Efficiency of the "Normal Particle" request in DATA (green) and MC (blue) as function of incidence angle. b) Ratio between DATA and MC efficiencies. A slight dependance on the incidence angle is seen in the DATA - MC discrepancy.

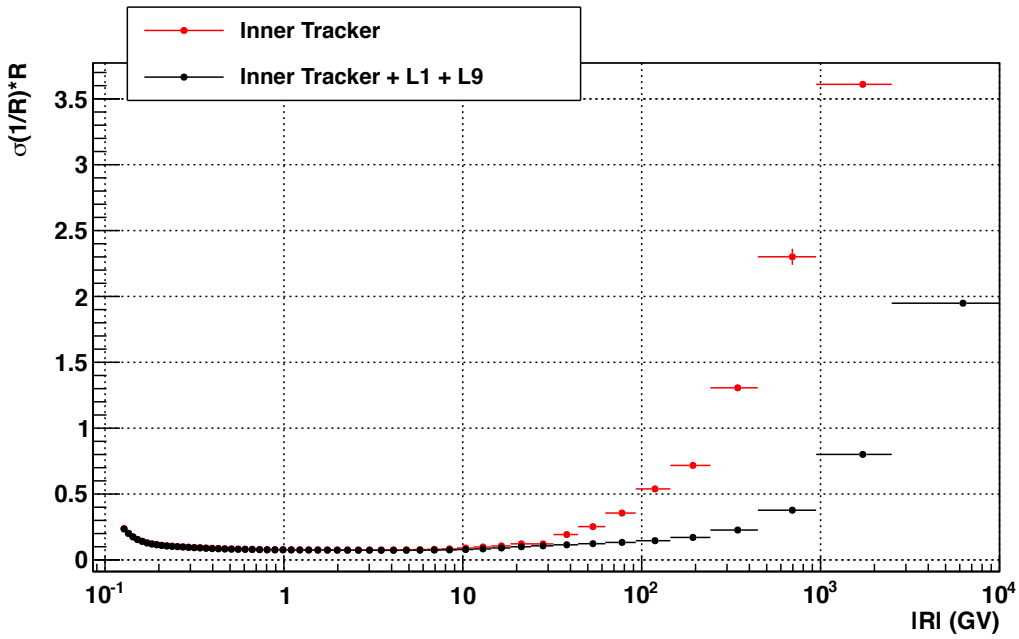

Figure 4.32: Tracker resolution ($\sigma(\frac{1}{R})/\frac{1}{R}$) as function of the particles Rigidity, using only inner tracker (red) or using also hit on layers 1 and 9 (black).

Fig. 4.32 shows the momentum resolution as a function of momentum evaluated in the MC for muon events with 1 Normal Particle reconstructed in the INNER tracker and with the full span measurement.
In our analysis we have required to have a rigidity measurement performed over the full tracker span: this greatly reduces the acceptance, keeping only $\sim$ 10% of the statistics, and the effect of this request has been studied on both DATA and MC as a function of rigidity and particle θ angle as shown in Figs. 4.33 and 4.34. The main effect is due to the reduction in geometrical acceptance: not all the tracks found with INNER tracker are passing trough the two external layers. This effect is clearly seen in Fig. 4.34 where the efficiency of this request is reported as a function of the zenithal angle θ: events at large θ values are highly suppressed, due to the reduction of the angular acceptance. For vertical tracks, a $\approx$ 45% of the events reconstructed in the INNER tracker falls out of the last tracker layer, which has a reduced acceptance.
The DATA - MC discrepancy, above $\sim$ 0.3 GV can be quoted as:

$$C_{Span} = 0.97 \pm 0.01$$

At very low rigidities both the acceptance decreases significantly both in the MC and DATA and a discrepancy up to 20% is observed. In fact, at low energies, the extrapolation of the INNER tracker to external layers is affected of a larger uncertainty due to the multiple scattering in the detector material (TOF, TRD). This results in a poorer efficiency in the hit association on the external layers, with a critical dependence of the extrapolation on the accuracy in the description of the detector geometry and materials.

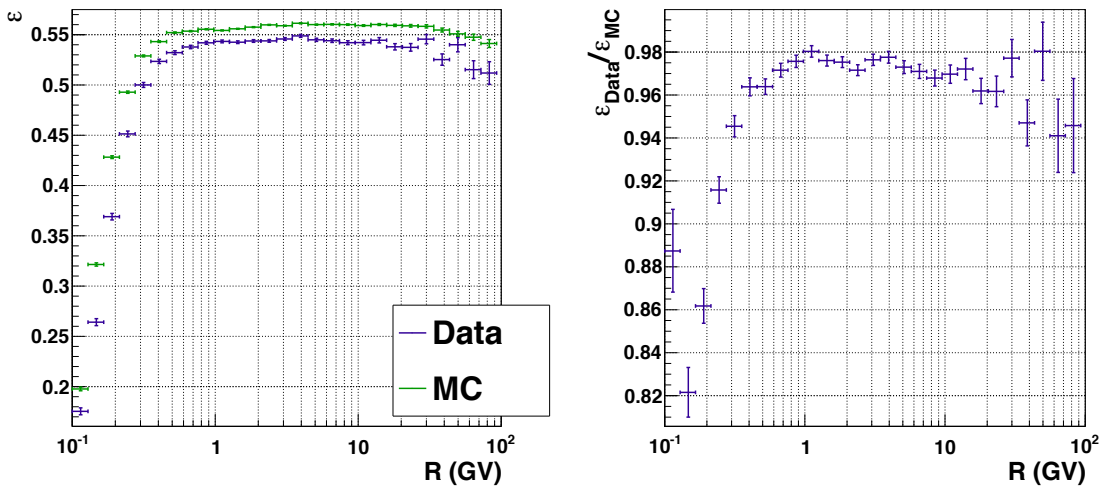

(a) (b)

Figure 4.33: a) Efficiency of the "Span1-9" request in DATA (green) and MC (blue) as function of rigidity, for "vertical" particles. b) Ratio between DATA and MC efficiencies.

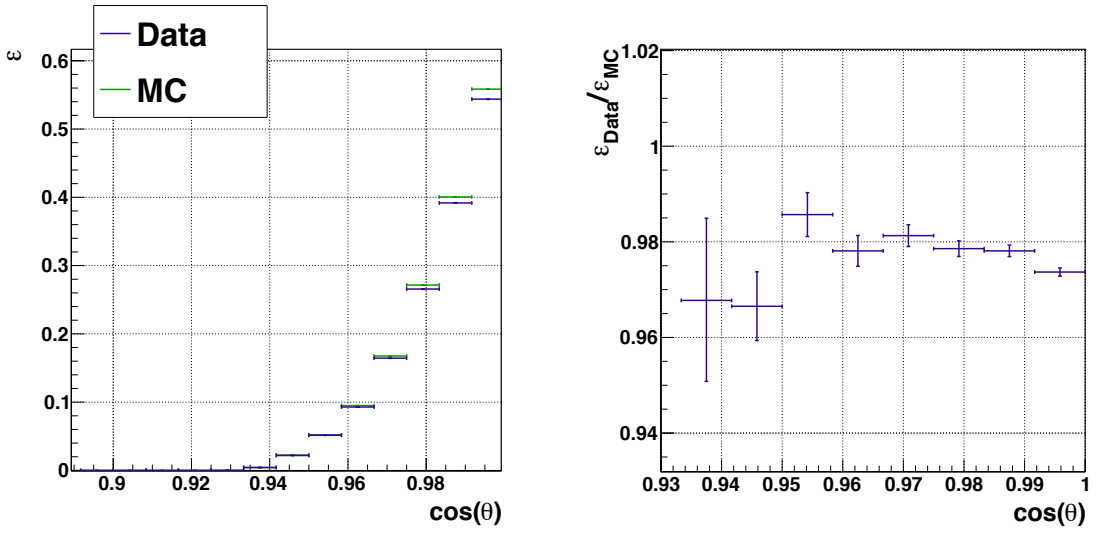

(a) (b)

Figure 4.34: a) Efficiency of the "Span1-9" request in DATA (green) and MC (blue) as function of incidence angle. b) Ratio between DATA and MC efficiencies.

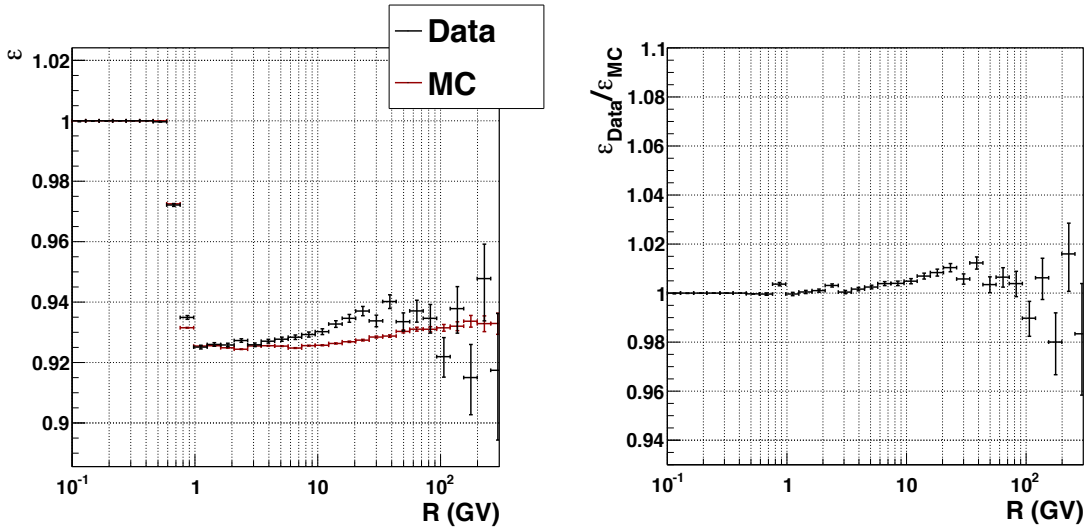

(a) (b)

Figure 4.35: a) Efficiency of the "Layer 2" request in DATA (black) and MC (red) as function of the rigidity, b) Ratio between DATA and MC efficiencies as a function of the rigidity.

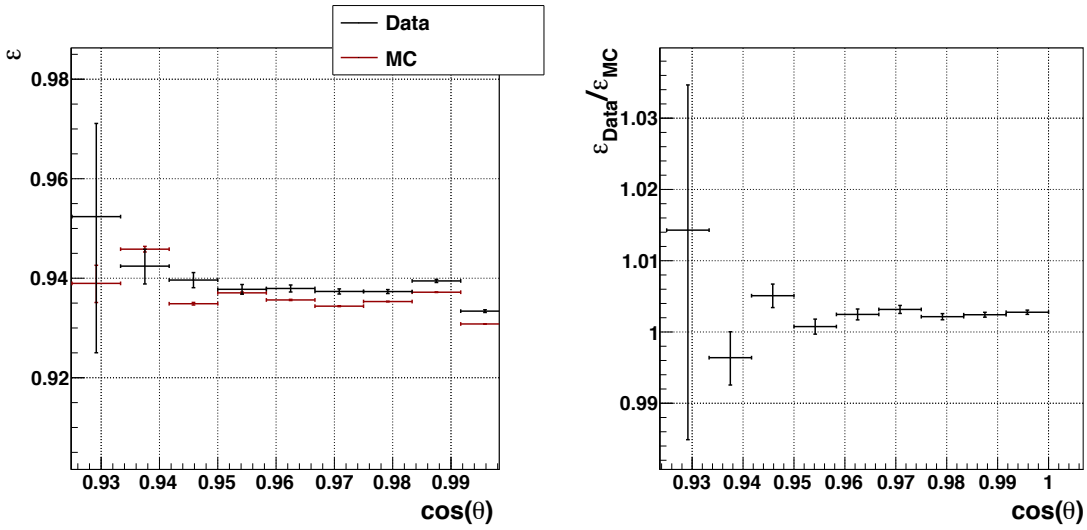

(a) (b)

Figure 4.36: a) Efficiency of the "Layer 2" request in DATA (black) and MC (red) as function of incidence angle. b) Ratio between DATA and MC efficiencies.

Table 4.1: Encoding of the β-pattern

β-pattern	TOF planes used
0	1,2,3 and 4
1	1, 2 and 3
2	1, 2 and 4
3	1, 3 and 4
4	2, 3 and 4
5	1 and 3
6	1 and 4
7	2 and 3
8	2 and 4
9	1 and 2
10	3 and 4

After the selection of full span tracks, a further request on the presence of a measurement point on layer 2 in the reconstructed track was performed. While adding a $\sim$ 5% inefficiency, expected due to the geometrical inefficiencies at the layer level, this request insures a better quality of the track since it guarantees a better extrapolation of the inner tracker track to the layer 1 when the hit association on the external layer is performed.
The efficiency of the cut has been studied in both DATA and MC as function of rigidity (see Fig. 4.35) and incidence angle (see Fig. 4.36).
The behaviour of the efficiency at low momenta, both in DATA and MC, is a feature of the pattern recognition algorithm. The matching window to associate an hit on layer 2 and the track built with the inner layers is a function of the particle rigidity, increasing at low momenta to take into account multiple scattering effects. However, at rigidities below 1 GV, the chosen window is clearly too wide and also noise hits are associated to the track. This feature, which will be corrected in the next tracker reconstruction code version, is anyhow well reproduced in the MC which contains also a realistic simulation on noise clusters.
The DATA - MC discrepancy is estimated to be:

$$C_{L2} = 1.005 \pm 0.005$$

For the reasons explained above the two efficiencies become strictly one at low rigidities and so no DATA - MC discrepancy can be seen in this range.

4.4.8 Measurement of velocity quality

To get rid of the poorly measured velocities, a selection of the events based on the quality of the TOF information used in the β measurement was performed. Events were rejected if one or more TOF clusters used in the β satisfied the following conditions:

- the corresponding TOF paddle was tagged as “bad”;

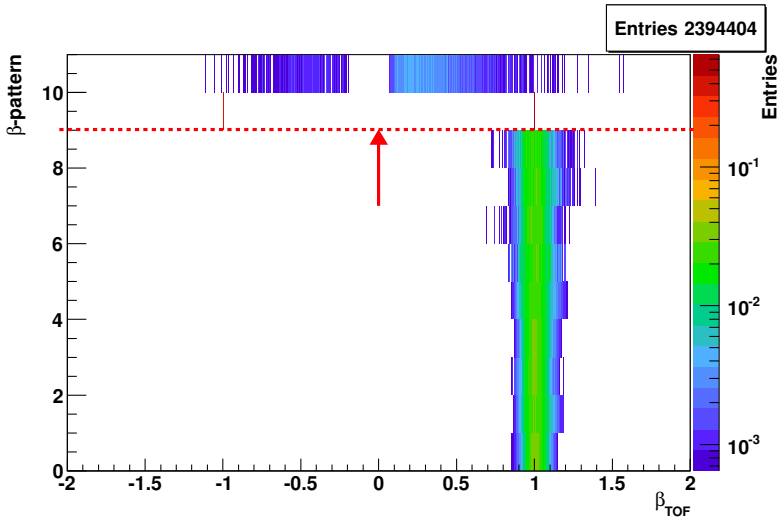

Figure 4.37: The pattern of TOF layers used to evaluate β as a function of β itself. Events with only two layers from the Upper (Lower) TOF are rejected, since evidently misreconstructed. In each β_{TOF} bin the β-pattern distribution has been normalized to the unity.

- the cluster had a "bad history". More than one temporal information in the same cluster (more than one particle traversed the TOF paddle) and is not possible to recover the "correct" one;
- the temporal information is given only by one side of the TOF paddle;
- the cluster was not contributing to the trigger.

Depending on the number of TOF layers used in the β measurement (at least two) different reconstruction quality is expected. In Fig. 4.37 the number of TOF layers, encoded according to Table 4.1, is plotted against the reconstructed β. As expected, velocity measurements using only two clusters from adjacent TOF planes have a different distribution - mostly misreconstructions - and are not relevant in our analysis. The events with β-patterns below 9 have been rejected. All the requests performed on β quality measurement remove less than 1% of the events and their efficiency has been studied in both DATA and MC as function of rigidity (see Fig. 4.38) and incidence angle (see Fig. 4.39). As for the other selection criteria, the DATA - MC efficiency ratio has been studied in order to assess the discrepancy and the corresponding error:

$$C_{BetaQuality} = 0.993 \pm 0.002$$

The discrepancy is greater below ~ 0.2 GV and reaches up to a 2% level.

4.4.9 Number of Transition Radiation Detector tracks

High energy particles interacting in upper part of the detector are the biggest source of "internal" background. They were discussed in Sec. 3.5 ("Low Reco"

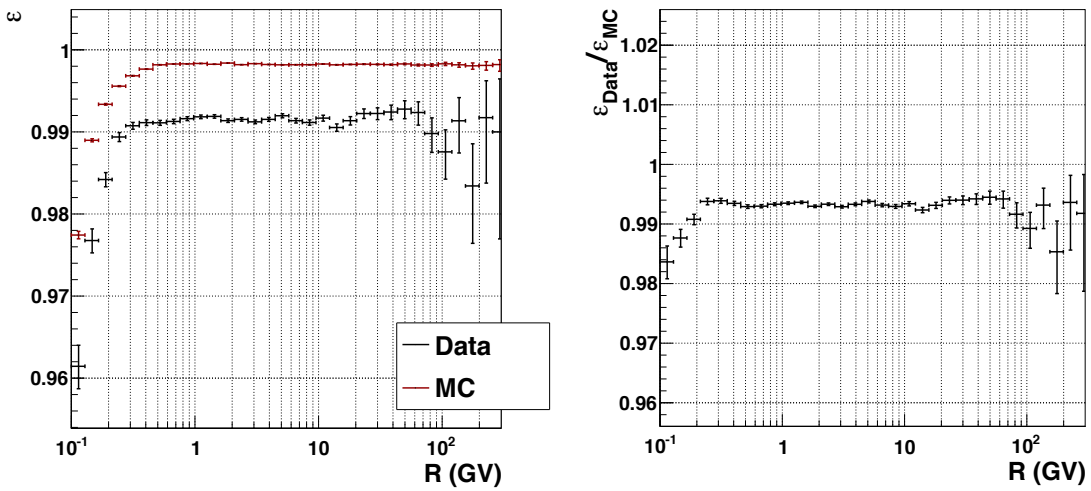

(a) (b)

Figure 4.38: a) Efficiency of the "Beta Quality' requests (together) in DATA (black) and MC (red) as function of rigidity. b) Ratio between DATA and MC efficiencies.

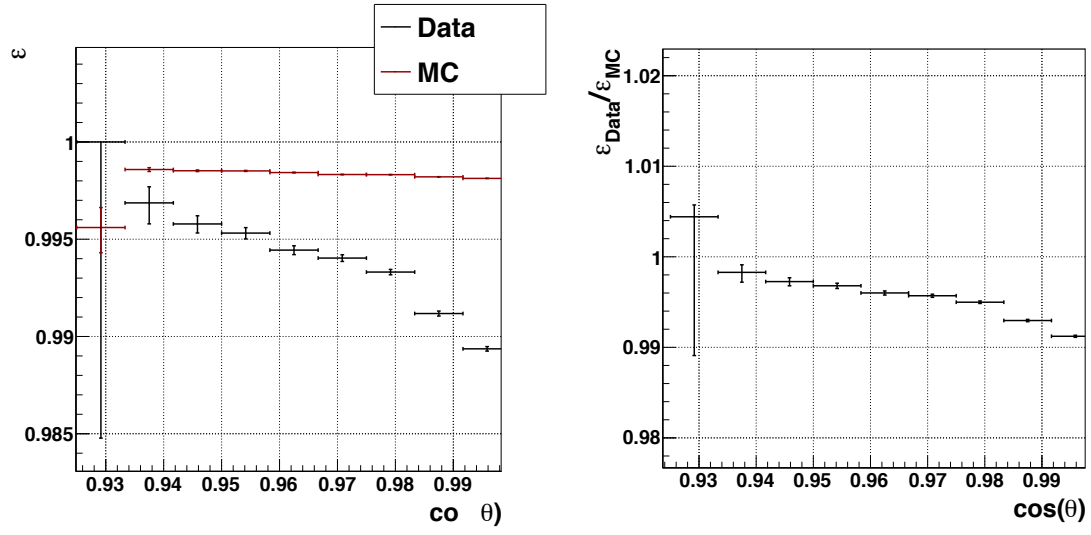

(a) (b)

Figure 4.39: a) Efficiency of the "Beta Quality" requests (together) in DATA (black) and MC (red) as function of incidence angle. b) Ratio between DATA and MC efficiencies.

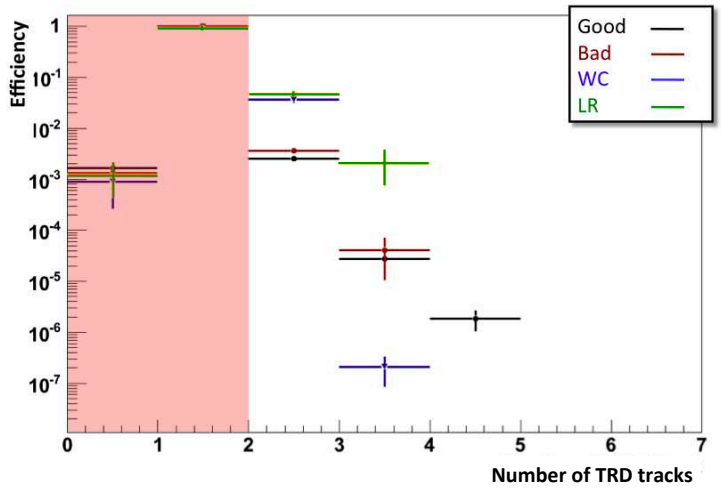

Figure 4.40: Cut efficiency on MC categories with respect to number of reconstructed TRD tracks. Asking for at maximum 1 TRD track removes $\sim$ 5% of "Wrong Charge" and "Low Reco" events keeping more than 99.5% of "Good" events.

category) and their signature will be further discussed later (see 4.4.10).
Events with an interaction or a δ-ray production are characterized by other particles in addition to the "primary", releasing a larger multiplicity of signals in different detectors. From the study carried on the MC sample, the requests of no ACC fired, one single track and one single β measurement already reject $\sim$ 90% of this class of events.
We also studied the multiplicity of the other subdetector signals: TRD, RICH and ECAL. In fact, looking at the number of tracks reconstructed in the TRD (Fig. 4.40) a further 5% of the *LowReco* and *WrongCharge* events is removed by asking at most 1 TRD track reconstructed in the event. This cut, in total, removes less than 0.5‰ of the events and, after, no events are characterized by multiple RICH rings or ECAL showers
Its effect has been studied in both DATA and MC as function of rigidity (see Fig. 4.41) and incidence angle (see Fig. 4.42) and the DATA - MC discrepancy has been evaluated as:

$$C_{AtMost1TRDTrack} = 0.9995 \pm 0.0005$$

As observed also in the previous selection criteria at very low rigidities (below $\sim$ 0.4 GV) the behaviour on DATA is not well reproduced in MC and the discrepancy reaches up to a 4% level.

4.4.10 Mass selection

The small background from atmospheric protons, electrons and positron can be in principle rejected by mass measurement of the detected particle, defined from

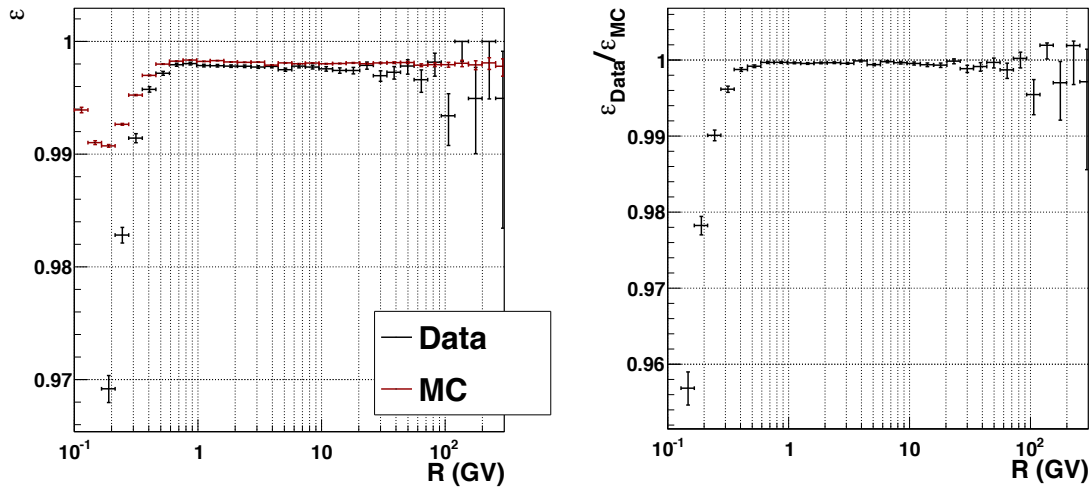

(a) (b)

Figure 4.41: a) Efficiency of the "At most 1 TRD track" request in DATA (black) and MC (red) as function of rigidity. b) Ratio between DATA and MC efficiencies. Almost no discrepancy is found above ~ 0.5 GV.

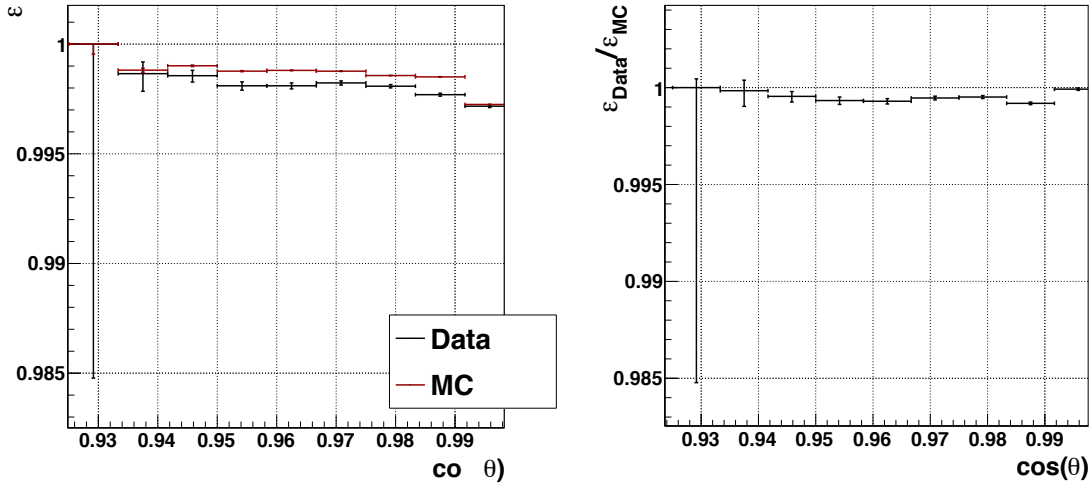

(a) (b)

Figure 4.42: a) Efficiency of the "At most 1 TRD track" request in DATA (black) and MC (red) as function of incidence angle. b) Ratio between DATA and MC efficiencies.

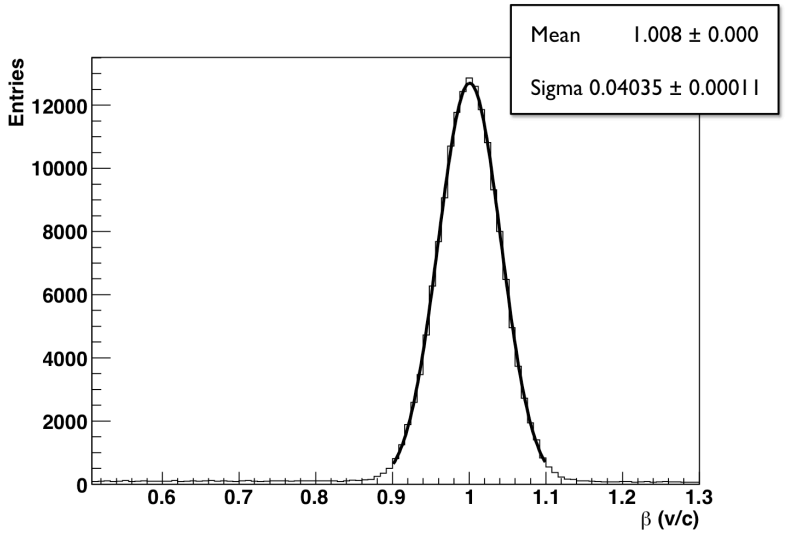

Figure 4.43: Distribution of velocities measured by AMS-02 using the Time of Flight, for β=1 particles. The width of the distribution is the velocity resolution.

the rigidity and velocity measurement:

$$m = R\frac{\sqrt{(1-\beta^2)}}{\beta} = \frac{R}{\gamma\beta} \tag{4.4}$$

where the unitary charge $Z = 1$ has been assumed. The mass resolution can be evaluated from the uncertainties in the rigidity and beta determination as follows:

$$\frac{\delta m}{m} = \sqrt{\frac{(\delta R)^2}{R^2} + \gamma^4\frac{(\delta\beta)^2}{\beta^2}} \tag{4.5}$$

A momentum resolution between 20% and 10% characterizes the tracker measurement between 0.1 GV and few GVs (see 4.32) whereas a 4% resolution in the β measurement of the TOF can be estimated from the distribution of the ultra-relativistic particles presented in Fig. 4.43. At 100 MV, the momentum resolution of Silicon Tracker dominates and the mass resolution is $\sim$ 20% for both protons and muons. As the rigidity increases, the γ^4 factor makes the velocity resolution the dominant source of error. At 1 GV, the mass resolution becomes $\sim$ 15% for protons and $\sim$ 40% for muons. Above 1 GV, the two species are no longer separable.

A more accurate measurement of velocity could be performed with the RICH detector, with a per-mille resolution, at the price of a severe reduction in the statistics due to the reduced acceptance of the RICH detector. Given the smallness of the background level and the limited statistics available we therefore judged not to require the RICH measurement in the selected events.

In order to exploit the mass difference between muons, protons and electrons, we

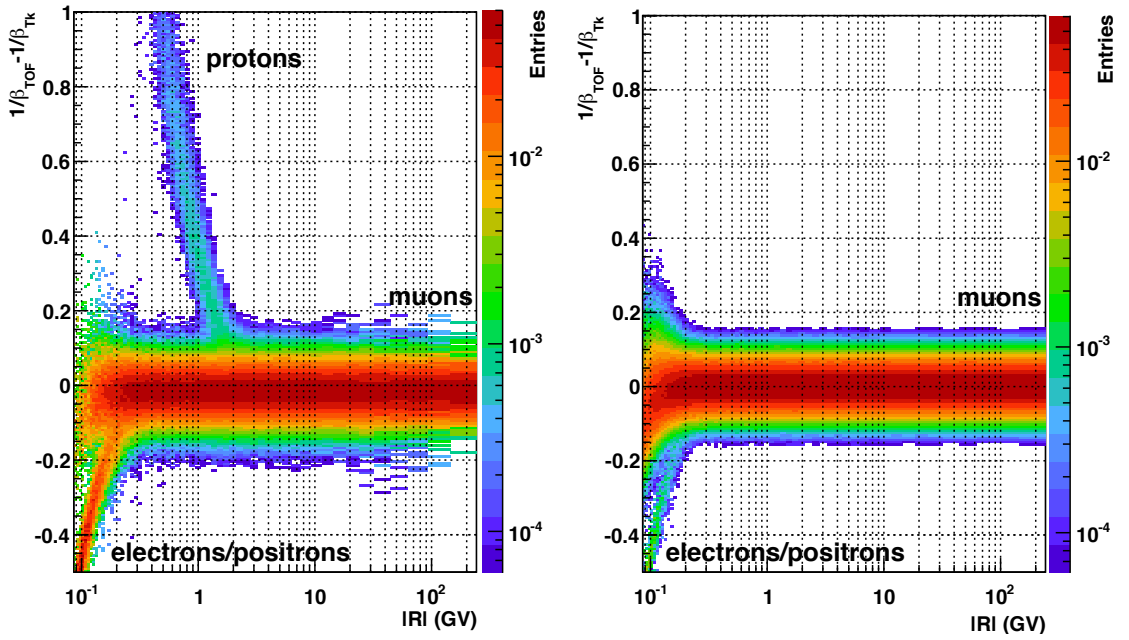

Figure 4.44: Difference between $1/\beta_{TOF}$ and $1/\beta_{Tk}$ (assuming muon mass) as function of rigidity. On the left the distribution for DATA and on the right for MC. The distribution has to be equal to zero independently from rigidity for a muon. In the DATA are clearly visible protons (cosmic) and electrons/positrons (can be cosmic, produced into the detector or into the KSC roof). In the MC are visible electrons/positrons produced into the detector. The mass resolution is dominated by TOF resolution in the almost complete rigidities range. The distributions are normalized to unity in the y-slices.

defined the particle β from tracker assuming the muon mass as:

$$\beta_{Tk} = \sqrt{\frac{R^2}{R^2 + m_\mu^2}} \tag{4.6}$$

comparing the β_{Tk} with the TOF measurement. The velocity measured by the TOF (β_{TOF}) and the velocity defined from the tracker should be null and independent from rigidity. Such a distribution is shown in Fig. 4.44 for DATA and MC samples, independently of the charge sign of the particle. The difference is made on the inverse of β since this is the gaussian quantity for TOF. In DATA are clearly visible protons (atmospheric) and electrons/positrons (can be atmospheric, produced into the detector or into the SSPF roof). In MC are visible electrons/positrons produced into the detector. The mass resolution is dominated by TOF resolution in the almost complete rigidities range.
In Fig. 4.45 the same distributions are shown separately for particles reconstructed with positive and negative charge sign. Protons and positron background are clearly visible in the positive particle sample on top of the dominant μ^+ distribution, whereas only electrons - as expected - are evident as background in the μ^- sample. Positrons and electrons can be due to external sources, either the normal atmospheric flux or interactions in the SSPF roof, but can also be

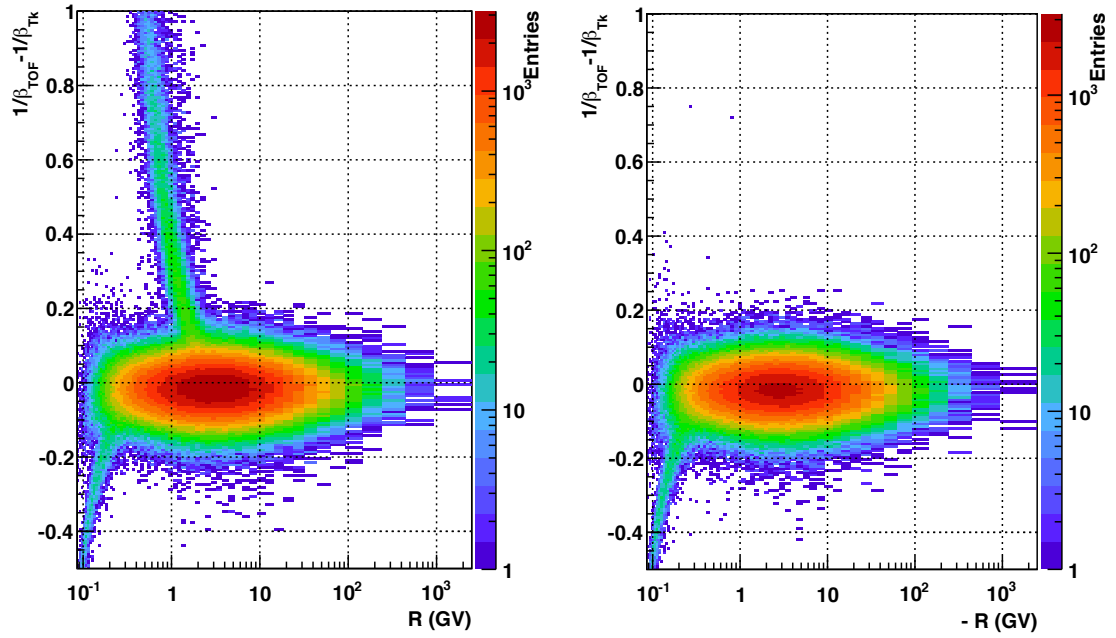

Figure 4.45: Difference between $1/\beta_{TOF}$ and $1/\beta_{Tk}$ (assuming muon mass) as function of rigidity, for DATA. On the left the distribution for positive reconstructed particles and on the right for negative ones. Protons are visible only in the positive charged sample, while electrons and positrons are visible in both.

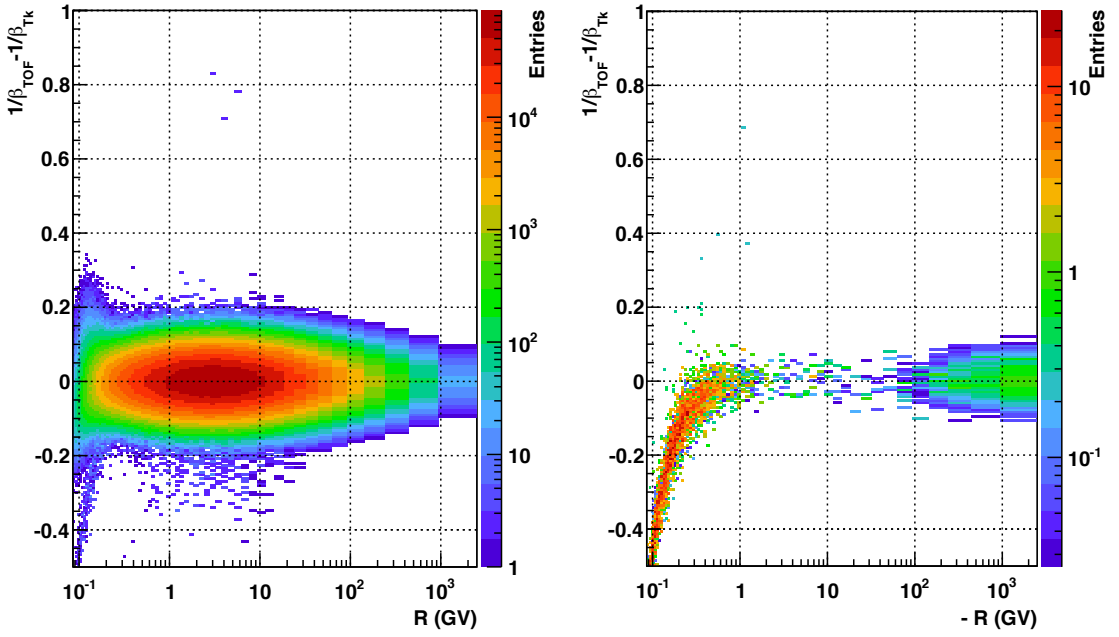

Figure 4.46: Difference between $1/\beta_{TOF}$ and $1/\beta_{Tk}$ (assuming muon mass) as function of rigidity, for MC. On the left the distribution for particles with a well reconstructed sign of charge (with respect to the generated one) and on the right for wrong ones. In the wrong sign reconstructed particles are visible two effects: at low rigidities the electrons and positrons produced by interactions and muon decays inside the detector while at high energies is visible the spillover.

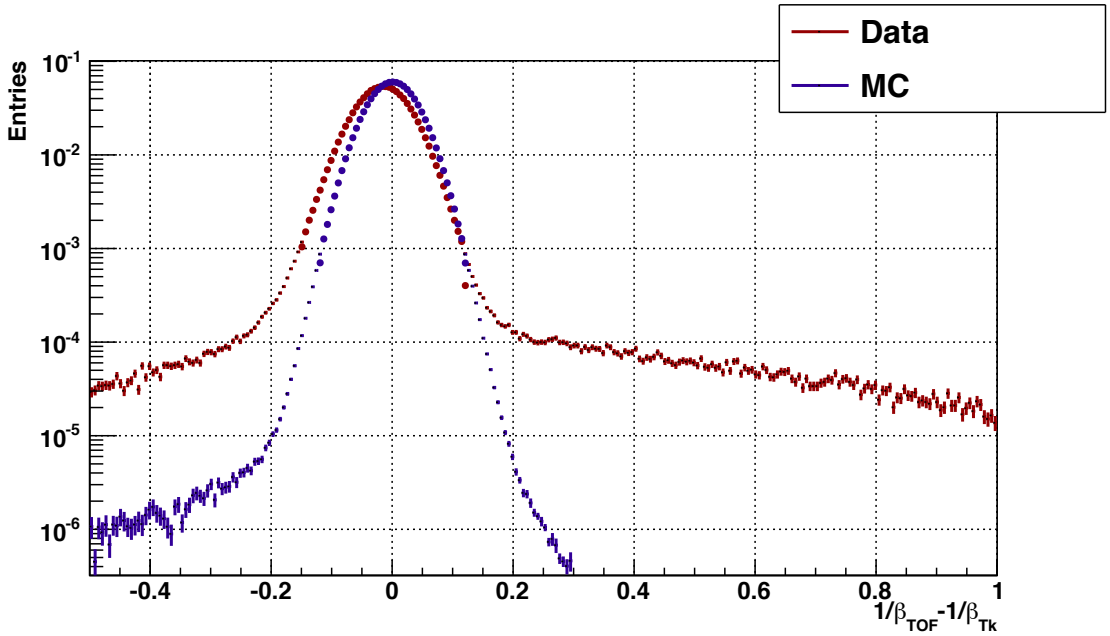

Figure 4.47: Difference between $1/\beta_{TOF}$ and $1/\beta_{Tk}$ (assuming muon mass). Distribution for MC (blue) is narrower with respect to DATA one (red) and perfectly center to zero. In DATA is visible the tail on the right due to proton background and the higher (with respect to MC) tail due to "physical" electrons/positrons. Underlined (bigger markers) the part of distribution kept after the $\mu \pm 3\ \sigma$ cut. Distributions areas are normalized to unity.

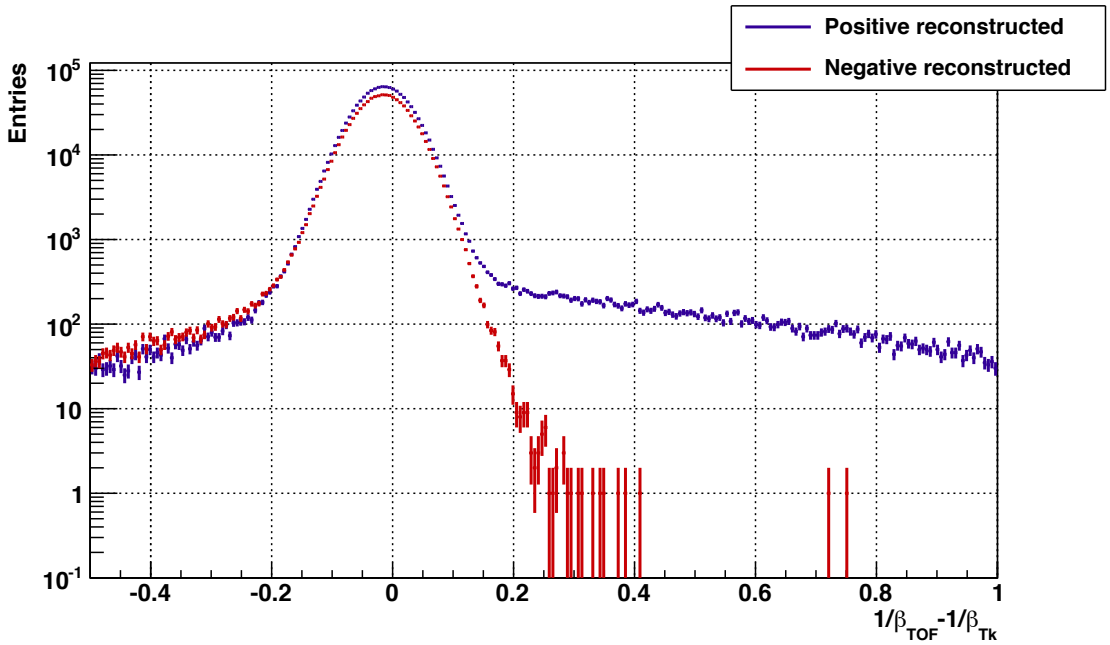

Figure 4.48: Difference between $1/\beta_{TOF}$ and $1/\beta_{Tk}$ (assuming muon mass) on DATA. Distribution for positive reconstructed (blue) shows the proton background and positrons tails. Negative reconstructed one (red) shows only the electrons tail. Electrons and positrons tails are almost of the same intensity and this doesn't depend on the μ^+ and μ^- relative abundances.

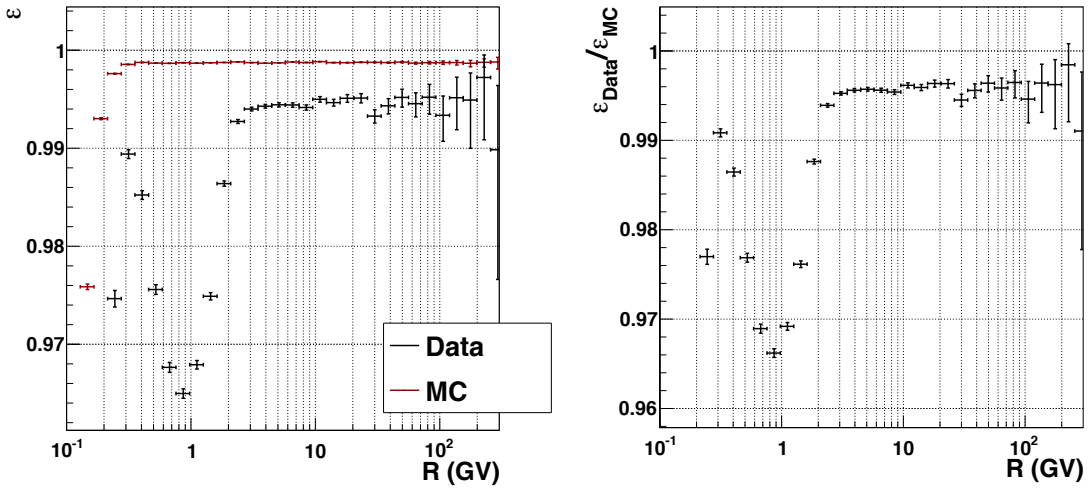

(a) (b)

Figure 4.49: a) Efficiency of the "Muon Mass" request in DATA (black) and MC (red) as function of rigidity. b) Ratio between DATA and MC efficiencies. Below 3 GV is visible when the cut becomes to be effective on protons and on electrons/positrons.

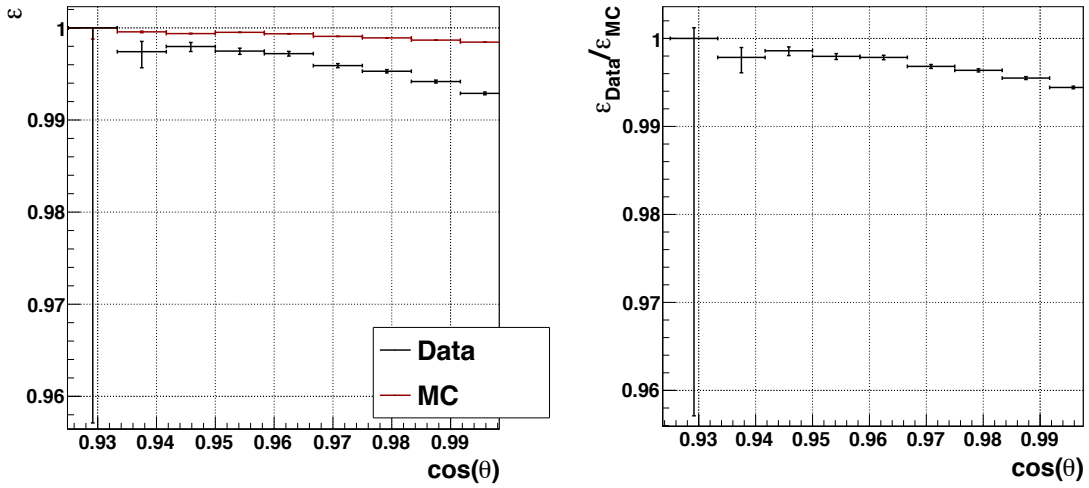

(a) (b)

Figure 4.50: a) Efficiency of the "Muon Mass" request in DATA (black) and MC (red) as function of incidence angle, for R > 3 GV. b) Ratio between DATA and MC efficiencies.

secondaries from the interactions in the detector or muon decay.

In Fig. 4.46 is shown the difference in MC separately for particles having the correct or the wrong reconstructed charge sign with respect to the generated muon. In the correct charge sample muons and electrons/positrons are visible, whereas in the wrong charge sample there is a clear component at low rigidity of electrons/positrons produced in the detector. In the wrong charge sample also wrong sign muons are clearly recognizable at high rigidities: they are due to spillover.

The cumulative distributions of $1/\beta_{TOF} - 1/\beta_{Tk}$ shown in Fig. 4.47 have been used to define the selection criteria. In MC the resolution is slightly narrower than in DATA and perfectly centered to zero, in order to apply an homogeneous rejection criteria on both samples, the mean (μ) and standard deviation (σ) of the distribution have been separately evaluated on DATA and MC by a gaussian fit, rejecting the events outside a 3σ window centered on the fitted μ.

The events removed by the cut are due to protons (only on DATA) and e^+/e^-.

The efficiency of the cut has been studied in both DATA and MC as function of rigidity (see Fig. 4.49) and incidence angle (see Fig. 4.50). Above ~ 3 GV a good agreement between DATA and MC is found, with an average ratio between the efficiencies of 99.8%. At lower energies, the different behaviour between DATA and MC is clearly related to the background rejection, which is effective only on the DATA. In fact, the efficiency dip in DATA between 0.4-3 GV is related to the energy range where the proton background is present and the corresponding rejection is effective. At energies below 300 MeV rejection of the electron/positron background becomes important and, as can be observed in Fig. 4.47 a larger electron/positron component is present in the DATA with respect to the MC. The efficiencies and their ratio as a function of incidence angle have been compared for rigidities greater than 3 GV. The discrepancy can be quoted as:

$$C_{MuonMass} = 0.994 \pm 0.002$$

Chapter 5

Muon Measurements on Ground: Flux and Ratio Evaluation

5.1 Introduction

In the previous chapter we selected 484 runs to be analyzed applying several run quality criteria, for a global initial statistics of $\sim 6 \cdot 10^7$ events and 242 hours of data taking. Taking into account the livetime of the experiment is possible to calculate the real exposure time of the experiment evaluated in ~ 238 hours (see §5.3).
After applying criteria for a clean muon measurement selection we remained with $2.14 \cdot 10^6$ events. The last energy bin of the measurement in the rigidity range between 1 TV – 2.5 TV counts 20 events for an associated statistical error of 20%.
The same selection designed to remove background and improve the muon reconstruction quality on DATA has been applied on MC to evaluate the acceptance.
The raw number of counts per rigidity bin, combined with the exposure time and the acceptance evaluated from the MC will give the flux estimation. Errors both of statistical and systematic origin - due to finite resolution, background, and acceptance evaluation - must be associated to the flux measurement.
From the counts of positive and negative reconstructed particles, we can also derive the μ^+/μ^- ratio. In the ratio the acceptance, the exposure time cancel out as well as most of the systematic uncertainties. Only statistical error and systematics due to background and finite resolution have been added.

In this chapter will be discussed the evaluation exposure time and of the acceptance needed to the flux estimation. Then flux and the associated uncertainties will be discussed. The ratio measurement will be presented as well.

5.2 Number of counts and acceptance

Once applied the above described selection we remain with the number of counts spectra shown in Fig. 5.1.

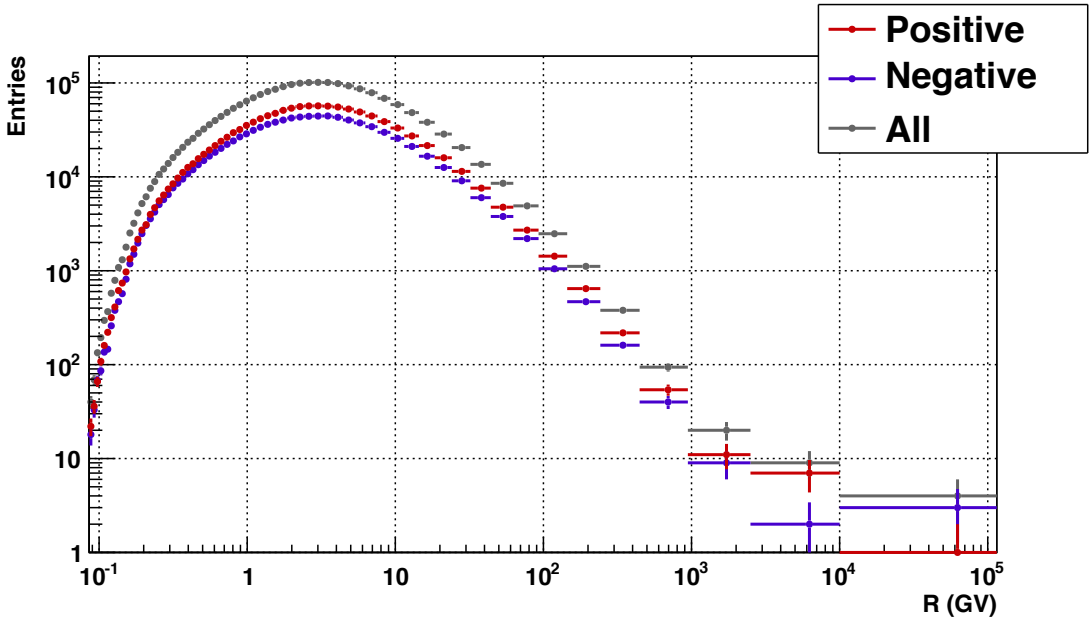

Figure 5.1: Raw number of counts after selection. Positive (red) and negative (blue) reconstructed particles are shown. Overall number of counts (grey) is shown as well. Errors on y are statistical.

We will determine the flux using:

$$\varphi(\overline{R}) = \frac{N_{det}(R_1 < R < R_2)}{\Delta T \; A(\overline{R}) \; \Delta R} \qquad \left[\left(\text{GV m}^2 \text{ sr s}\right)^{-1}\right] \quad (5.1)$$

where A($\overline{R}$) is the acceptance evaluated in the same point $\overline{R}$ where the flux is quoted and ΔT is the exposure time of the analyzed period. The point $\overline{R}$ is the mean rigidity [39], over the bin, and can be evaluated after a first fit to the measured flux: in the first step the bin center (i.e. $(R_1 + R_2)/2$) or the geometric mean (i.e. $\sqrt{R_1 R_2}$) is used to stick the point, the overall flux is fitted and the point is evaluated again.
Since the acceptance is enough flat for a very wide range of rigidities (see Fig. 5.2) the mean acceptance in the $[R_1, R_2]$ range has been used:

$$A(\overline{R}) \approx \frac{\int_{R_1}^{R_2} A(R) dR}{\Delta R} \quad (5.2)$$

5.2.1 Evaluation of Acceptance

The acceptance has been evaluated on MC applying the same selection used for DATA and is shown in Fig. 5.2 as [49][1]:

$$A(R) = A_{gen.pl.} \frac{N_{det}(R)}{N_{gen}(R)} = \pi l^2 \frac{N_{det}(R)}{N_{gen}(R)} \qquad \left[\text{m}^2 \text{ sr}\right] \quad (5.3)$$

[1]For N(R) we mean N(R_1<R<R_2), i.e. the number of entries in the bin which contains R. For $\mathcal{A}$(R) we mean, instead, the differential acceptance evaluated in the point R (i.e. the bin mean point). This has be done for sake of simplicity in the notation.

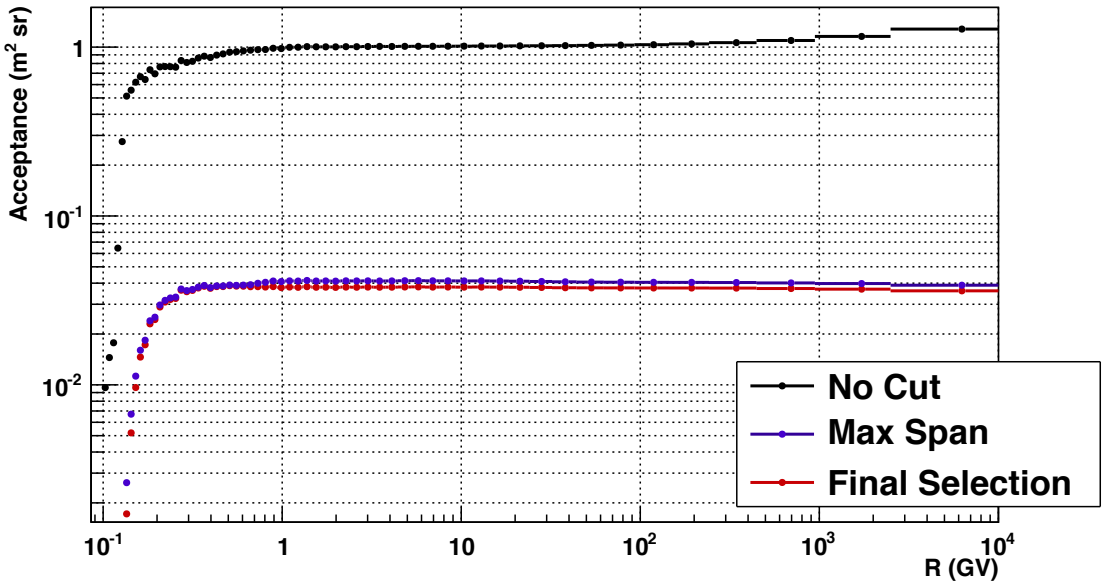

Figure 5.2: Muon acceptance curves in different steps of analysis. The muon acceptance without any selection (black), after requiring the Max Span configuration (blue) and the final one (red).

The final value of acceptance is dominated by the Max Span request that reduces at one tenth the field of view. The initial acceptance (without any selection) increases at high energies for the interaction of very inclined particles: the produced particles are enough "vertical" to give trigger. At low rigidities the acceptance falls for two reasons: the energy losses into the detector materials are enough to stop the particles and the magnetic gyro-radium is not enough to let the particles reach the lower part of TOF.
The acceptance has to be multiplied (or alternatively the flux divided) by the correction factor evaluated by the DATA - MC comparison:

$$A_{corr}(R) = A_{raw}(R) \cdot C$$

where the correction has been evaluated as:

$$C = C_{OneBeta} \cdot C_{OneTrack} \cdot C_{Normal} \cdot C_{Span} \cdot C_{L2} \cdot C_{BetaQuality} \cdot C_{AtMost1TRDTrack} \cdot C_{MuonMass}$$

using the discrepancies of various cuts evaluated in §4 and summarised in Tab. 5.1. The total correction has a value of:

$$C = 0.929 \pm 0.014 \tag{5.4}$$

where the error o the correction to apply to the acceptance will be used as systematic for the flux measurement.
For the last 6 cuts (after the request of a track) the same kind of comparison (explained in §4) made for the various cuts has been performed as they were a

Table 5.1: Discrepancies from DATA - MC comparison

Discrepancy from cut	value of discrepancy ± systematic error
$C_{OneBeta}$	1.00001 ± 0.00001
$C_{OneTrack}$	0.973 ± 0.008
C_{Normal}	0.993 ± 0.002
C_{Span}	0.97 ± 0.01
C_{L2}	1.005 ± 0.005
$C_{BetaQuality}$	0.993 ± 0.002
$C_{AtMost1TRDTrack}$	0.9995 ± 0.0005
$C_{MuonMass}$	0.994 ± 0.002

single cut. The DATA - MC discrepancy, both as function of incidence angle and of rigidity, after 3 GV, has been estimated to be:

$$C_{Normal-MuonMass} = 0.96 \pm 0.01$$

combining this number with the discrepancy of the two residual cuts gives:

$$C_{OneBeta-MuonMass} = 0.93 \pm 0.01$$

that is fully compatible with the correction evaluated in Eq. 5.4.
Below 3 GV the discrepancy grows up, either due to the cut on the muon mass either due to the low energies discrepancy shown for each single cut.
Below 1 GV the additional, with respect to the one accounted in the correction, discrepancy estimated for all the cuts, except the mass cut, has been associated as systematic error on the acceptance and, consequently, on the flux.

The MC evaluated acceptance depends on the injected MC angular spectrum. MC sample has been generated with an isotropic spectrum while muons on ground have a steeper angular distribution. To take into account the possible systematic due to this effect the differential acceptance has been evaluated as:

$$\mathcal{A}(R, \cos\theta) = \mathcal{A}_{gen.pl.} \frac{N_{det}(R, \cos\theta)}{N_{gen}(R, \cos\theta)} = 2\pi l^2 \cos\theta \frac{N_{det}(R, \cos\theta)}{N_{gen}(R, \cos\theta)} \left[\mathrm{m}^2 \text{ rad}\right] \quad (5.5)$$

and is shown in Fig. 5.3.
The number of accepted events can be written in terms of generated ones and differential acceptance as:

$$N_{det}(R, \cos\theta) = \frac{N_{gen}(R, \cos\theta)\ \mathcal{A}(R, \cos\theta)}{2\pi l^2 \cos\theta} \quad (5.6)$$

The acceptance can be evaluated, starting from the differential acceptance, as:

$$\begin{aligned} A &= \pi l^2 \frac{N_{det}(R)}{N_{gen}(R)} = \pi l^2 \frac{\sum_{\cos\theta} N_{det}(R, \cos\theta)}{\sum_{\cos\theta} N_{gen}(R, \cos\theta)} = \\ &= \frac{\sum_{\cos\theta} N_{gen}(R, \cos\theta)\ \mathcal{A}(R, \cos\theta) \cos^{-1}\theta}{\sum_{\cos\theta} N_{gen}(R, \cos\theta)} \end{aligned} \quad (5.7)$$

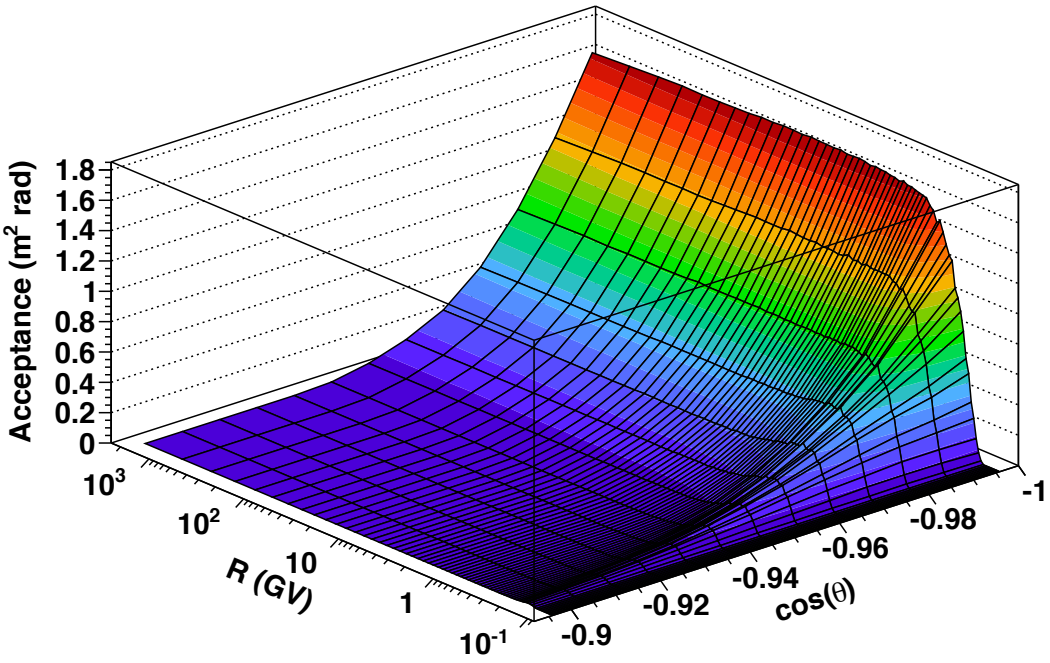

Figure 5.3: Differential acceptance after the selection.

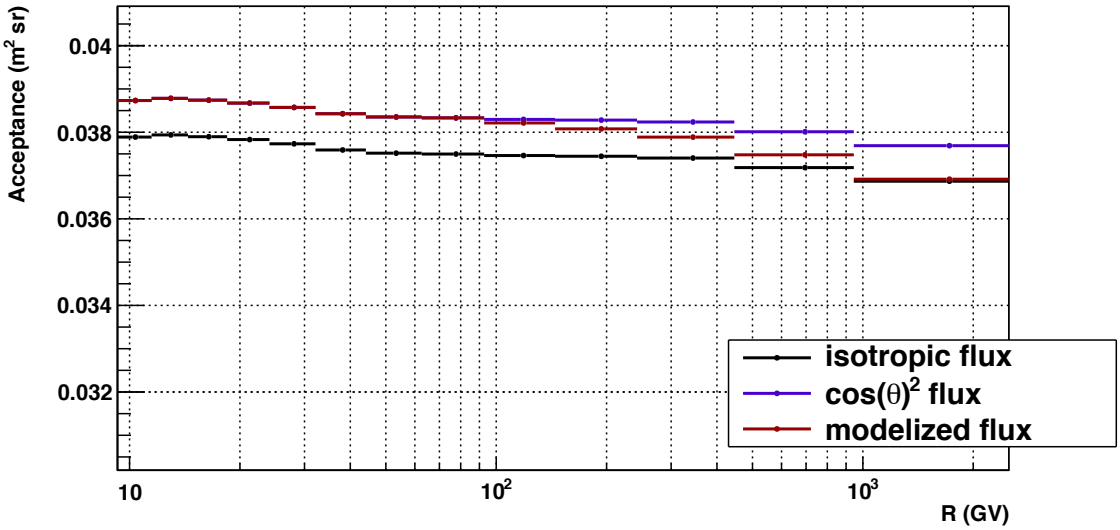

Figure 5.4: Acceptance evaluated assuming different angular distributed fluxes. Isotropic (black), Angular distribution $\propto \cos^2\theta$ (blue, low energies muon flux on ground) and a modelized [32] (red) one are shown. The discrepancy between isotropic and low energies muon flux on ground is $\sim$ 2%. The modelized flux is within the 2% band.

To study the systematic error made in the acceptance evaluation having used an isotropic flux we can modify the latter as:

$$A = \frac{\sum_{\cos\theta} w(\cos\theta) N_{gen}(R, \cos\theta)\ \mathcal{A}(R, \cos\theta) \cos^{-1}\theta}{\sum_{\cos\theta} w(\cos\theta) N_{gen}(R, \cos\theta)} \tag{5.8}$$

where $w(\cos\theta)$ is a weight, function of $\cos\theta$, used to modify the original isotropic simulated spectrum. An angular distribution $\propto \cos^2\theta$ (i.e. the spectrum of low energy muons on ground) and a modelized one [32] that takes into account the flattening (approaching $\sec\theta$) of the spectrum at very high rigidities, have been used. The acceptances, calculated with the three different injection spectra are shown in Fig. 5.4. The discrepancy is at the 2% level and has to be added to the acceptance uncertainties.

5.3 Exposure Time

As discussed also in Sec. 2.2.10.4 for an absolute flux measurement is necessary to know the exact time the detector is open to accept events.
Each AMS-02 event has a time stamp given by the JLV1 (the time of the given Level-1 trigger). Only a part to of each single data taking run (30 minutes) has been analyzed and its duration has been decide off-line. The period start (end) has been chosen randomly in a few seconds "window" after (before) the first (last) event. In such a way the duration of the data taking is completely asynchronous with respect to the presence of events and no bias on the exposure time is induced. A variable amount of events, from the head and from the tail of each single run, will be not used for the analysis.
Each AMS-02 event has, also, a Live Time value (see Sec. 2.2.10.4) measured as the fraction of not busy time in a 1 second long gate. After the end of a gate and during the next gate, all the triggered events will be recorded on disk with associated the same Live Time value (measured during first gate). At the beginning of the run the events have a Live Time value that is wrong for up two seconds. Let's take, as example, a gate starting at the time t_0. This gate will end at $t_0 + 1\,s = t_1$, the next gate will be delimited by t_1 and $t_0 + 2\,s = t_2$, the next to next by t_2 and $t_0 + 3\,s = t_3$ and so on. Let's suppose the run starting somewhere between t_1 and t_2, let's call t_s. The first event recorded will be somewhere after t_s. For the first part (a fraction of second between t_s and t_2) events will have a Live Time value referred to a gate during which the system was disabled (i.e. before the start of the run, between t_0 and t_1). For the latter part (a complete second between t_2 and t_3) events will have a value referred to a gate (between t_1 and t_2) during which the system was enabled only for a fraction of time (between t_s and t_2).
For this analysis, as shown in Fig. 5.5, one single event per second has been taken for the Exposure Time evaluation. The events used are the ones within a time window that starts $1 - 2$ seconds after the first event and terminates $0 - 1$ seconds before the last event, for each single run. The integral of Fig. 5.5 distribution gives the Exposure Time: the mean is the mean Live Time ($\sim$ 98.5%)

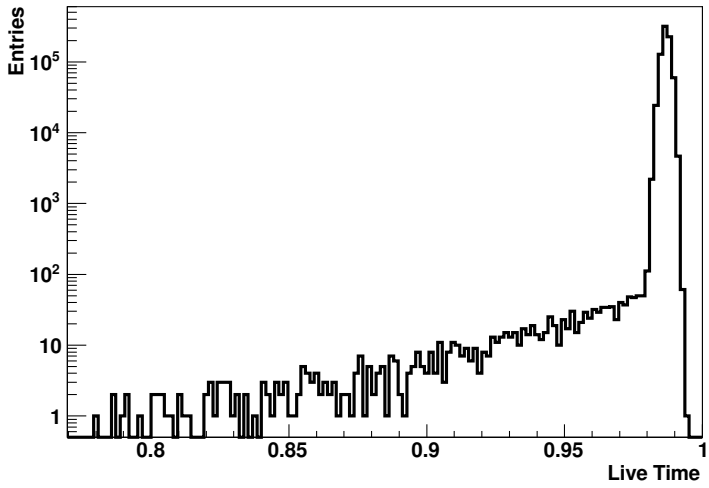

Figure 5.5: Live Time distribution for the runs selected for analysis. One event per second has been used. The integral of distribution gives the Exposure Time: the mean is the mean Live Time ($\sim$ 98.5%) during the whole data taking and the number of entries is the data taking duration itself.

during the whole analysed data taking period and the number of entries is the period duration itself:

$$\Delta T = \int_T LT\,dt \tag{5.9}$$

The Live Time measurement is done with a 20 ns counter during a 1 s long gate. For a 0.90 Live Time value (even well below the mean) the device counted $0.9 \cdot 10^9$ counts. The statistical error is below the 0.1 ‰.
As explained above, the Live Time measurement, performed in the 1 s long gate, is retrieved at the end of the gate itself. For each run, the first Live Time measurement we used is referred to events not used during analysis. The last Live Time measurement we used is not referred to the very last events: for them the measurement is in the following, rejected, events. Missing 2 measurements over 1800 (each run is 30 m long) leads. at most, to a $\sim$ ‰ error.

5.4 Errors on flux

The overall error on the flux measurement and its breakdown in the main components previously discussed is reported in Fig. 5.6. A conservative approach has been used in the evaluation of the single components, leaving room for significative improvements in the future.
The discrepancy evaluated on MC after unfolding dominates the systematic uncertainty at very low (< 200 MV) rigidities and above few hundred GVs and is partially related to large statistical fluctuations of the MC sample used for the evaluation (see Fig. 3.12). In fact, the behaviour of this correction as a function of

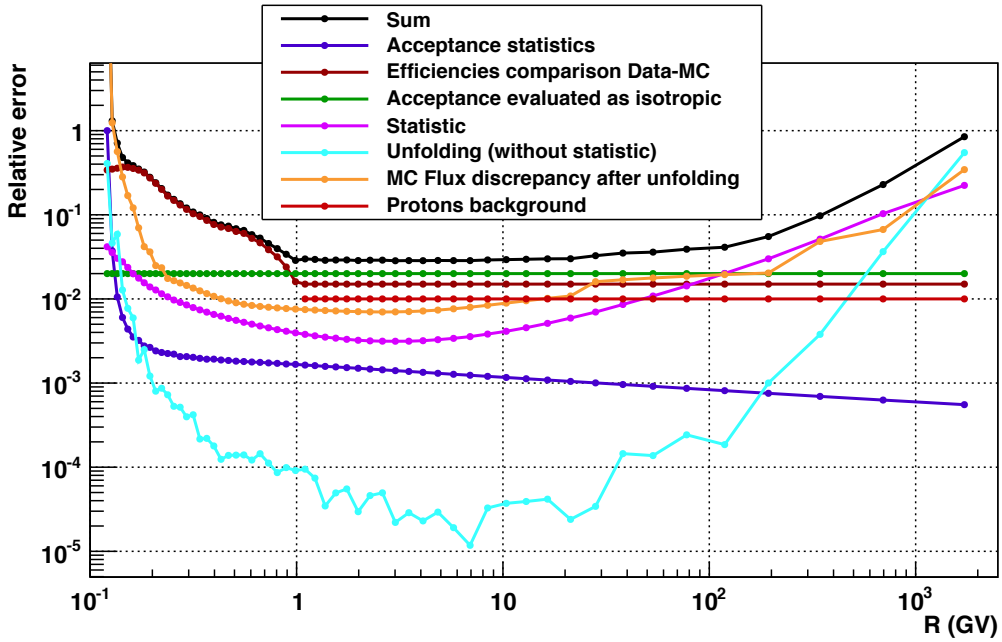

Figure 5.6: Error on "vertical" muon flux on ground measurement (black) as function of rigidity. The error, to be associated to the flux, is the sum of various components, both systematics that statistics. The various components are superimposed: MC statistics used to evaluate the acceptance (blue), efficiencies comparison between DATA and MC (maroon), acceptance evaluated as isotropic (green), statistic (violet), unfolding (cyan), MC discrepancy after unfolding (orange), protons background (red). Errors coming from protons background have been considered only after 1 GV.

energy clearly correlates with the unfolding error (and hence with the statistical fluctuations), however we conservatively added them in quadrature in the overall error.

As discussed in Sec. 3.7 the error coming from the unfolding procedure in each energy interval is a mixture of the statistical and systematics uncertainties, we artificially separated the two contributions in the error breakdown by subtracting in quadrature the statistical error - as defined by the number of counts after unfolding - from the total error resulting at the end of the unfolding procedure.

Below 1 GV, a large systematic error is related to the discrepancy observed in the DATA-MC comparison of the different selection criteria efficiencies. Also in this we adopted a very conservative approach; in that energy region the contamination of physical background - not simulated in the Monte Carlo - is one of the most important sources of discrepancy but we treated the disagreement as if it was all due to a poor description of the detector response.

The largest contribution to the systematics in the GV - 100 GV range (2%) comes from the acceptance evaluation (see Sec. 5.2.1): this can be easily reduced by direct evaluation of the angular flux.

The relative abundances of electrons and protons backgrounds is known from literature and has been discussed in Sec. 1.4. A 1% error coming from protons

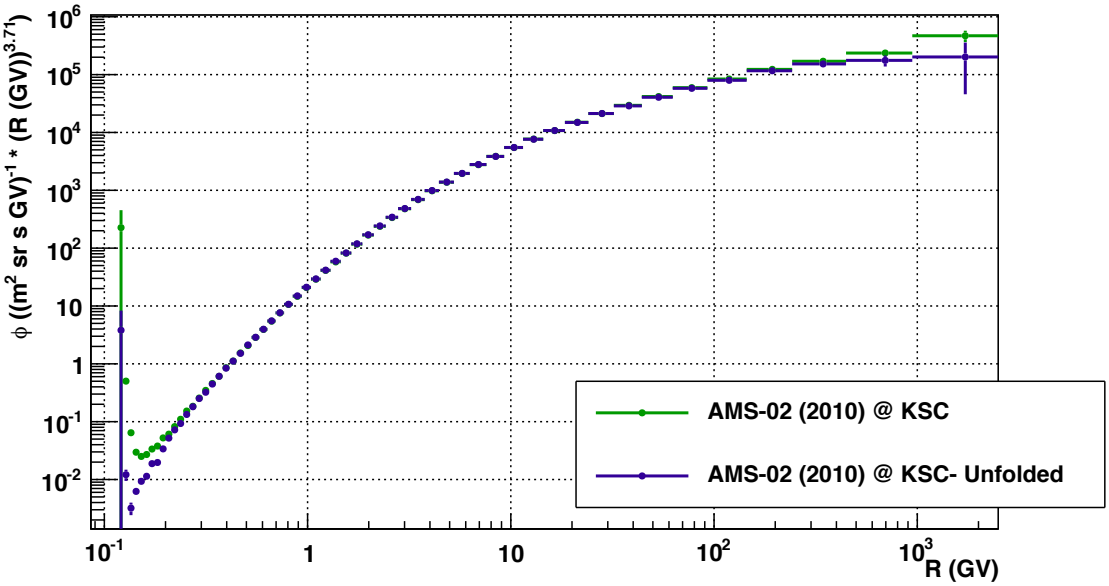

Figure 5.7: Muon on ground flux. Raw (green) and unfolded (blue) fluxes are shown. Errors are only statistics for raw flux and coming out from unfolding procedure for the corrected one. Fluxes have been scaled by $R^{3.71}$.

background has been considered after 1 GV. Below, the protons have been cut with the mass cut. As discussed in §4.4.10 using the RICH one can separate muons from protons up to an higher energy ($\sim$ 10 GV). The RICH, therefore, can be used to further remove the proton background or, at least, to give an estimation of the proton/muon ratio in the 1 - 10 GV reducing the associated systematic error on flux.
No error due to the electrons/positrons background has been considered. This background, however, if not negligible, can be further investigated looking at signals into ECAL.
All the various components have been added quadratically.
The systematic error, in a very wide range of rigidities (1 - 100 GV), has been evaluated to be at the few percent level (3 - 4%). Above, the statistical uncertainty becomes the greatest source of error and the statistical fluctuations have driven, as discussed above, also the evaluation of the residual discrepancy after unfolding. In the very last rigidity bin, around the MDR, the uncertainty related to the unfolding dominates the total error: this reflects the 100% error on rigidity measurement at the MDR.

5.5 Flux

Muon "vertical" flux measurement resulting from this analysis is shown in Fig. 5.7. Unfolding has been applied to DATA raw counts to correct, as explained in Sec. 3.7, for energy losses into the detector materials and for the effects of finite resolution in conjunction with a power law falling spectrum.

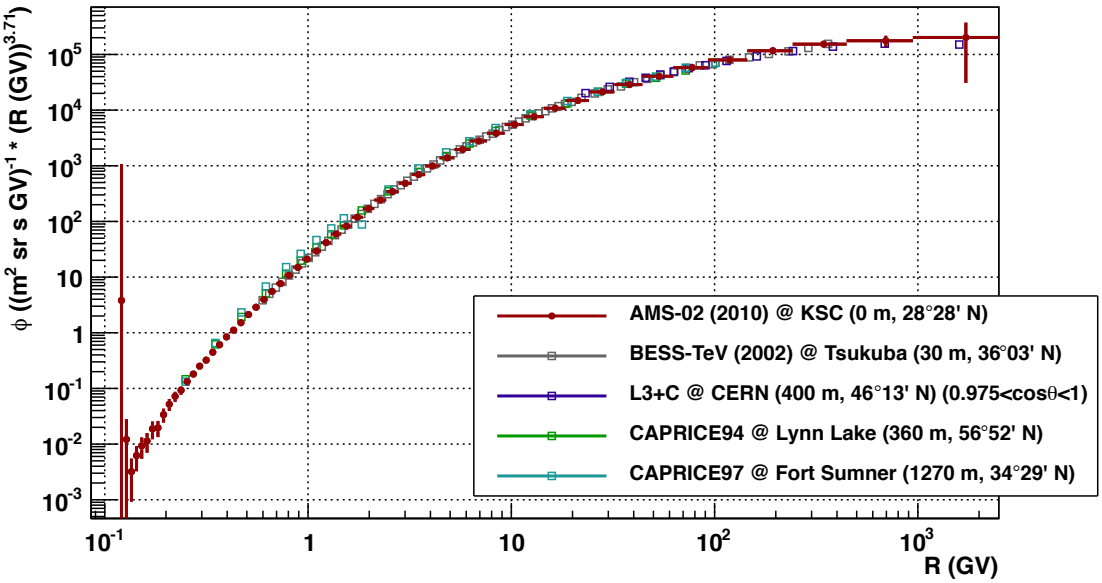

Figure 5.8: Muon "vertical" flux. Flux of this analysis (blue circles) with systematic and statistic errors can be compared with Bess [31] (grey squares), L3+C [1] (blue squares), CAPRICE94 and CAPRICE97 [38] "vertical" fluxes. Fluxes have been scaled by $R^{3.71}$.

Errors estimated in 5.4 has been associated to the unfolded flux and the result is shown in Fig. 5.8. BESS [31], L3+C [1], CAPRICE94 and CAPRICE97 [38] "vertical" fluxes are shown for comparison.
Experimental results are given in Tab. A.1 in Appendix A. Points with a relative error greater than 100% are not reported.
The analysis performed obtained a flux measurement with a systematic error competitive with previous experiment in a very wide range of rigidities. Further improvements, however, are possible to reduce even more the systematic error: the measurement of differential fluxes would remove one of the greatest sources of systematic in the acceptance evaluation.
Further improvements, as the inclusion in the analysis flow of the RICH (to remove the possible background from protons in the 1-10 GV range) and of the ECAL (to remove the possible background of electrons/positrons at very low energies), and as the simulation of the effect of the KSC roof, are foreseen.

5.6 Errors on ratio

With respect of flux, most of the systematics cancel out in the ratio and the only systematics to be considered are the deformation on the spectra due to finite resolution and the physical background. The error breakdown is shown in Fig. 5.9.
The discrepancy on ratio evaluated on MC dominates the systematic uncertainty at very low (< 1 GV) rigidities and above $\sim$ 100 GV. Its behaviour, as discussed

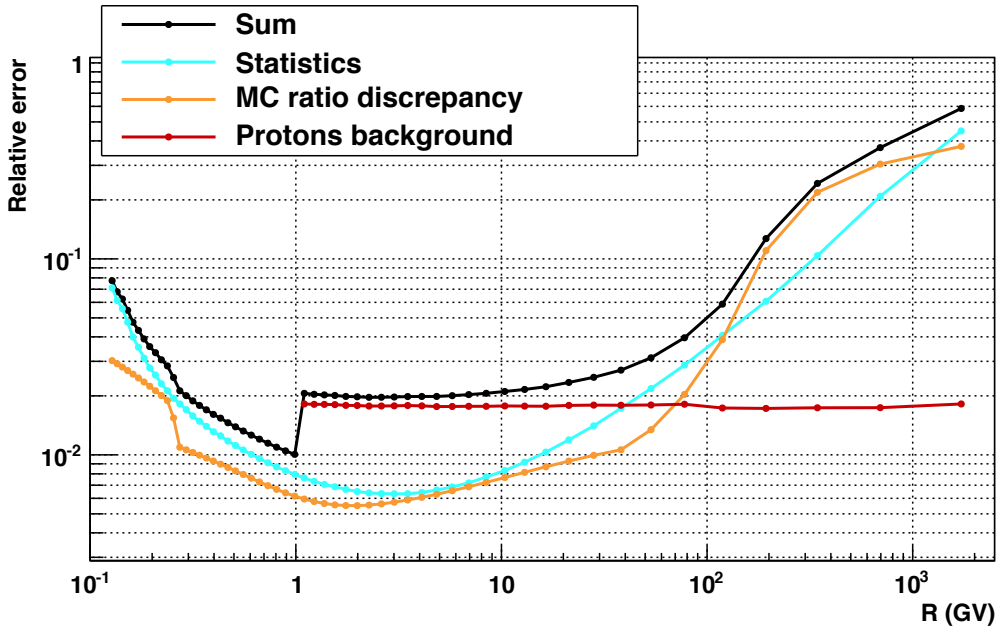

Figure 5.9: Error on "vertical" μ^+/μ^- ratio on ground measurement (black) as function of rigidity. The error, to be associated to the flux, is the sum of various components, both systematics that statistics. The various components are superimposed: statistics (cyan), MC ratio discrepancy (orange), protons background (red). Errors coming from protons background has been considered only after 1 GeV.

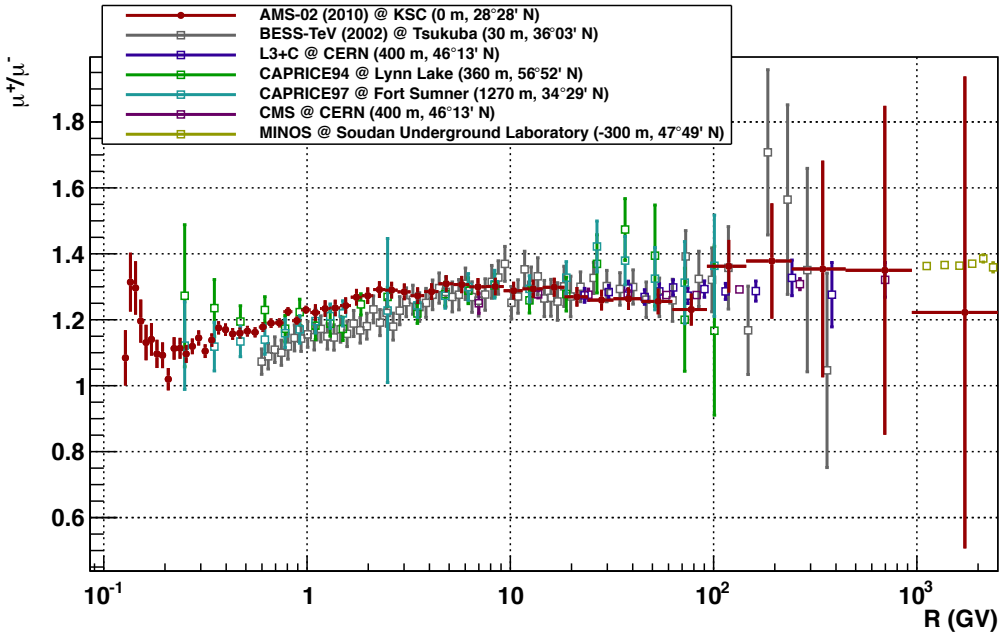

Figure 5.10: μ^+/μ^- ratio as function of rigidity. Ratio of this analysis (red full circles) with systematic and statistic errors can be compared with Bess (grey squares) [31] and L3+C (blue squares) [1], CAPRICE94 (green squares) and CAPRICE97 (azure squares) [38], CMS [36] (violet squares) and MINOS [2] (ochre squares) "vertical" ratios.

for the discrepancy in the flux (see Sec. 5.4), follows the statistical errors and, most likely, is related to large statistical fluctuations of the MC sample used for the evaluation (see Fig. 3.14).
Systematic due to protons background have been calculated and added to the "vertical" measurement of μ^+/μ^- ratio. In each rigidity bin, in facts, a p quantity of protons contaminates the ratio and what we really measured is:

$$\frac{\mu^+ + p}{\mu^-} = \frac{\mu^+}{\mu^-} + \frac{p}{\mu^-} = \frac{\mu^+}{\mu^-} + \frac{p}{\mu^+ + \mu^-}\frac{\mu^+ + \mu^-}{\mu^-} \tag{5.10}$$

With a ratio $p/(\mu^+ + \mu^-)$ of, at most, 1% (see Sec. 1.4) and being μ^- approximately the half of the all muons spectrum, we obtain a 2% error. Error due to protons background has been considered only above 1 GV. Below, protons have been removed with mass cut. As discussed in §4.4.10 the RICH can be used to further remove the proton background or, at least, to give an estimation of the proton/muon ratio in the 1 - 10 GV. This would help in reducing the associated systematic error on ratio. No error due to the electrons/positrons background has been considered. If not negligible this background can be removed easily looking for electromagnetic showers in the ECAL.
All the various components have been added quadratically.
The systematic error, in a very wide range of rigidities (1 - 100 GV), has been evaluated to be at the 2% level. Above, the statistical uncertainty becomes the greatest source of error and the statistical fluctuations have driven, as discussed above, also the evaluation of the discrepancy evaluated on MC. As future improvement one can remove all the statistical driven part of uncertainty from the systematic error due to finite resolution. Once reduced this source of systematic and the systematic due to proton background, the ratio uncertainty would be dominated by statistics.

5.7 Ratio

The "vertical" μ^+/μ^- ratio measurement resulting from this analysis is shown in Fig. 5.10. Errors estimated in 5.6 has been associated to the quoted ratio. Bess [31], L3+C [1], CAPRICE94 and CAPRICE97 [38], CMS [36] and MINOS [2] "vertical" ratios are shown for comparison.
Experimental results are given in Tab. A.1 in Appendix A.
As already discussed in §5.5 the analysis performed obtained a fmeasurement with a systematic error competitive with previous experiment in a very wide range of rigidities.
Further improvements are foreseen to remove possible systematics not included in the present measureement: the inclusion in the analysis flow of the RICH and ECAL to remove the possible background from protons and electrons/positrons and the simulation of the effect of the KSC roof on ratio.

Conclusions

Just one year ago, in January 2011, the commissioning of the AMS-02 spectrometer with atmospheric muons ended : the analysis of the $\sim 6 \cdot 10^7$ recorded events has been discussed in this dissertation and the first AMS-02 measurements of the atmospheric muon flux and μ^+/μ^- ratio presented.
Although very preliminary, the obtained results are competitive with previous measurements of different instruments, both in terms of statistics and systematic uncertainties, and span the widest energy interval for a single experiment.
Further improvements on the systematic uncertainties can, and will, be achieved in the muon flux measurement explicitly considering the differential detector acceptance, one of the largest sources of uncertainties over an extended energy range in the current measurement. At the same time, a careful revision of the statistical contribution to the MC evaluation of the errors in the flux and ratio measurements will allow to significantly reduce the overall uncertainties, especially in the high energy range. A direct measurement of the background components using RICH and ECAL, will finally allow to reduce the systematic uncertainties, both in the muon flux and ratio.
Large systematics errors have been attributed at low energies, i.e. below $\sim$1 GV, due to discrepancies observed between data and MC sample in the detector response. In fact, a contribution from physical background - absent in the MC simulation - is expected both from atmospheric electrons and protons and from secondaries generated in the interactions of atmospheric particles with the roof of the Space Shuttle Processing Facility were AMS was located. An estimate of the background could be performed by means of a dedicated simulation, allowing to disentangle the instrumental and physical effects in the observed behaviour. This will permit not only to reduce the uncertainties related to the background in the ratio measurement, but also to better understand and qualify the instrument performance at the lowest energies.
One of the objectives of this work was to test the AMS-02 simulation and reconstruction software as well as the single elements, from the detector acceptance to the livetime estimate, needed for flux measurements of cosmic rays in space; in this concern we accomplished the goal: unwanted features of the reconstruction were found during the analysis and have been already corrected for the processing of flight data.
As a summary of the three years spent in the AMS-02 construction, integration, beam test calibration, commissioning on ground and in flight I would conclude: it has been one of the most exciting experiences I have done, and more fun is still to come!

Appendices

Appendix A

Experimental Results

In Tab. A.1 the experimental results of this analysis: vertical all muons flux and μ^+/μ^- ratio on ground.

Table A.1: Observed vertical muon flux and μ^+/μ^- ratio on ground.

Rigidity range (GV)	Flux $\pm \Delta_{stat} \pm \Delta_{sys}$ (GV m^2 s sr)$^{-1}$	$\mu^+/\mu^- \pm \Delta_{stat} \pm \Delta_{sys}$
$0.1314 - 0.1391$	$5 \pm 0.2^{+4}_{-4}$	$1.31 \pm 0.08^{+0.04}_{-0.04}$
$0.1391 - 0.1475$	$8 \pm 0.2^{+4}_{-4}$	$1.30 \pm 0.07^{+0.04}_{-0.04}$
$0.1475 - 0.1565$	$1.0 \pm 0.02^{+0.4}_{-0.4} \times 10^1$	$1.20 \pm 0.06^{+0.03}_{-0.03}$
$0.1565 - 0.1663$	$10 \pm 0.2^{+4}_{-4}$	$1.13 \pm 0.05^{+0.03}_{-0.03}$
$0.166 - 0.177$	$1.3 \pm 0.02^{+0.5}_{-0.5} \times 10^1$	$1.14 \pm 0.04^{+0.03}_{-0.03}$
$0.177 - 0.188$	$1.1 \pm 0.02^{+0.3}_{-0.3} \times 10^1$	$1.10 \pm 0.03^{+0.03}_{-0.03}$
$0.188 - 0.201$	$1.5 \pm 0.02^{+0.4}_{-0.4} \times 10^1$	$1.09 \pm 0.03^{+0.02}_{-0.02}$
$0.201 - 0.214$	$1.8 \pm 0.02^{+0.4}_{-0.4} \times 10^1$	$1.02 \pm 0.03^{+0.02}_{-0.02}$
$0.214 - 0.229$	$1.9 \pm 0.02^{+0.4}_{-0.4} \times 10^1$	$1.11 \pm 0.03^{+0.02}_{-0.02}$
$0.229 - 0.245$	$1.9 \pm 0.02^{+0.3}_{-0.3} \times 10^1$	$1.11 \pm 0.02^{+0.02}_{-0.02}$
$0.245 - 0.263$	$2.1 \pm 0.02^{+0.3}_{-0.3} \times 10^1$	$1.10 \pm 0.02^{+0.02}_{-0.02}$
$0.263 - 0.282$	$2.2 \pm 0.02^{+0.3}_{-0.3} \times 10^1$	$1.12 \pm 0.02^{+0.012}_{-0.012}$
$0.282 - 0.304$	$2.4 \pm 0.02^{+0.3}_{-0.3} \times 10^1$	$1.14 \pm 0.02^{+0.012}_{-0.012}$
$0.304 - 0.327$	$2.3 \pm 0.02^{+0.2}_{-0.2} \times 10^1$	$1.10 \pm 0.02^{+0.011}_{-0.011}$
$0.327 - 0.353$	$2.4 \pm 0.02^{+0.2}_{-0.2} \times 10^1$	$1.14 \pm 0.02^{+0.011}_{-0.011}$
$0.353 - 0.381$	$2.5 \pm 0.02^{+0.2}_{-0.2} \times 10^1$	$1.18 \pm 0.02^{+0.011}_{-0.011}$
$0.381 - 0.413$	$2.6 \pm 0.02^{+0.2}_{-0.2} \times 10^1$	$1.17 \pm 0.02^{+0.011}_{-0.011}$
$0.413 - 0.448$	$2.5 \pm 0.02^{+0.2}_{-0.2} \times 10^1$	$1.16 \pm 0.014^{+0.010}_{-0.010}$
$0.448 - 0.487$	$2.5 \pm 0.015^{+0.2}_{-0.2} \times 10^1$	$1.16 \pm 0.014^{+0.010}_{-0.010}$
$0.487 - 0.531$	$2.6 \pm 0.014^{+0.2}_{-0.2} \times 10^1$	$1.17 \pm 0.013^{+0.010}_{-0.010}$
$0.531 - 0.579$	$2.6 \pm 0.013^{+0.2}_{-0.2} \times 10^1$	$1.16 \pm 0.012^{+0.009}_{-0.009}$
$0.579 - 0.634$	$2.53 \pm 0.013^{+0.13}_{-0.14} \times 10^1$	$1.178 \pm 0.012^{+0.009}_{-0.009}$
$0.634 - 0.696$	$2.51 \pm 0.012^{+0.12}_{-0.13} \times 10^1$	$1.190 \pm 0.011^{+0.009}_{-0.009}$
$0.696 - 0.766$	$2.44 \pm 0.011^{+0.10}_{-0.11} \times 10^1$	$1.191 \pm 0.011^{+0.008}_{-0.008}$

Rigidity range (GV)	Flux $\pm \Delta_{stat} \pm \Delta_{sys}$ (GV m^2 s sr)$^{-1}$	$\mu^+/\mu^- \pm \Delta_{stat} \pm \Delta_{sys}$
$0.766 - 0.846$	$2.39 \pm 0.010^{+0.08}_{-0.09} \times 10^{1}$	$1.225 \pm 0.011^{+0.008}_{-0.008}$
$0.846 - 0.936$	$2.30 \pm 0.009^{+0.06}_{-0.07} \times 10^{1}$	$1.197 \pm 0.010^{+0.008}_{-0.008}$
$0.94 - 1.04$	$2.21 \pm 0.009^{+0.04}_{-0.06} \times 10^{1}$	$1.230 \pm 0.010^{+0.008}_{-0.008}$
$1.04 - 1.16$	$2.07 \pm 0.008^{+0.04}_{-0.05} \times 10^{1}$	$1.222 \pm 0.009^{+0.02}_{-0.007}$
$1.16 - 1.30$	$1.95 \pm 0.007^{+0.04}_{-0.05} \times 10^{1}$	$1.234 \pm 0.009^{+0.02}_{-0.007}$
$1.30 - 1.46$	$1.82 \pm 0.006^{+0.04}_{-0.05} \times 10^{1}$	$1.236 \pm 0.009^{+0.02}_{-0.007}$
$1.46 - 1.64$	$1.63 \pm 0.006^{+0.03}_{-0.04} \times 10^{1}$	$1.243 \pm 0.009^{+0.02}_{-0.007}$
$1.64 - 1.86$	$1.49 \pm 0.005^{+0.03}_{-0.04} \times 10^{1}$	$1.268 \pm 0.008^{+0.02}_{-0.007}$
$1.86 - 2.12$	$1.33 \pm 0.004^{+0.03}_{-0.03} \times 10^{1}$	$1.273 \pm 0.008^{+0.02}_{-0.007}$
$2.12 - 2.42$	$1.16 \pm 0.004^{+0.02}_{-0.03} \times 10^{1}$	$1.292 \pm 0.008^{+0.02}_{-0.007}$
$2.42 - 2.79$	$9.8 \pm 0.03^{+0.2}_{-0.3}$	$1.290 \pm 0.008^{+0.02}_{-0.007}$
$2.79 - 3.23$	$8.1 \pm 0.03^{+0.2}_{-0.2}$	$1.285 \pm 0.008^{+0.02}_{-0.007}$
$3.23 - 3.77$	$6.68 \pm 0.02^{+0.13}_{-0.2}$	$1.273 \pm 0.008^{+0.02}_{-0.007}$
$3.77 - 4.43$	$5.29 \pm 0.02^{+0.10}_{-0.14}$	$1.285 \pm 0.008^{+0.02}_{-0.008}$
$4.43 - 5.25$	$4.00 \pm 0.013^{+0.08}_{-0.10}$	$1.309 \pm 0.009^{+0.02}_{-0.008}$
$5.2 - 6.3$	$2.96 \pm 0.010^{+0.06}_{-0.08}$	$1.307 \pm 0.009^{+0.02}_{-0.009}$
$6.3 - 7.6$	$2.12 \pm 0.008^{+0.04}_{-0.06}$	$1.300 \pm 0.009^{+0.02}_{-0.009}$
$7.6 - 9.3$	$1.41 \pm 0.005^{+0.03}_{-0.04}$	$1.301 \pm 0.010^{+0.02}_{-0.009}$
$9.3 - 11.5$	$9.4 \pm 0.04^{+0.2}_{-0.2} \times 10^{-1}$	$1.288 \pm 0.011^{+0.02}_{-0.010}$
$11.5 - 14.4$	$5.68 \pm 0.03^{+0.12}_{-0.2} \times 10^{-1}$	$1.29 \pm 0.012^{+0.03}_{-0.011}$
$14.4 - 18.5$	$3.33 \pm 0.02^{+0.07}_{-0.09} \times 10^{-1}$	$1.30 \pm 0.013^{+0.03}_{-0.011}$
$18.5 - 24.1$	$1.77 \pm 0.010^{+0.04}_{-0.05} \times 10^{-1}$	$1.27 \pm 0.02^{+0.03}_{-0.012}$
$24.1 - 32.1$	$9.0 \pm 0.06^{+0.2}_{-0.3} \times 10^{-2}$	$1.26 \pm 0.02^{+0.03}_{-0.013}$
$32 - 44$	$3.91 \pm 0.03^{+0.10}_{-0.12} \times 10^{-2}$	$1.26 \pm 0.02^{+0.03}_{-0.013}$
$44 - 63$	$1.58 \pm 0.02^{+0.04}_{-0.05} \times 10^{-2}$	$1.26 \pm 0.03^{+0.03}_{-0.02}$
$63 - 93$	$5.63 \pm 0.08^{+0.15}_{-0.2} \times 10^{-3}$	$1.23 \pm 0.04^{+0.03}_{-0.03}$
$93 - 145$	$1.60 \pm 0.03^{+0.04}_{-0.05} \times 10^{-3}$	$1.36 \pm 0.06^{+0.06}_{-0.05}$
$145 - 242$	$3.83 \pm 0.11^{+0.10}_{-0.12} \times 10^{-4}$	$1.4 \pm 0.08^{+0.2}_{-0.2}$
$242 - 446$	$5.9 \pm 0.3^{+0.3}_{-0.3} \times 10^{-5}$	$1.4 \pm 0.14^{+0.3}_{-0.3}$
$446 - 945$	$5.0 \pm 0.5^{+0.4}_{-0.4} \times 10^{-6}$	$1.4 \pm 0.3^{+0.4}_{-0.4}$
$945 - 2500$	$2.0 \pm 0.4^{+1.3}_{-1.3} \times 10^{-7}$	$1.2 \pm 0.5^{+0.5}_{-0.5}$

Bibliography

[1] Achard, P., et al., 2004: *Measurement of the atmospheric muon spectrum from 20 to 3000 GeV*. Physics Letters B, **598 (1-2)**, 15 – 32, 10.1016/j.physletb.2004.08.003, URL http://www.sciencedirect.com/science/article/pii/S0370269304011438.

[2] Adamson, P., et al., 2007: *Measurement of the atmospheric muon charge ratio at TeV energies with the MINOS detector*. Phys. Rev. D, **76**, 052 003, 10.1103/PhysRevD.76.052003, URL http://link.aps.org/doi/10.1103/PhysRevD.76.052003.

[3] Adriani, O., et al., 2009: *An anomalous positron abundance in cosmic rays with energies 1.5-100 GeV*. Nature, **458 (7238)**, 607–609, URL http://dx.doi.org/10.1038/nature07942.

[4] Adye, T., R. Claridge, K. Tackmann, and F. Wilson, 2011: Roounfold: Root unfolding framework. URL http://hepunx.rl.ac.uk/~adye/software/unfold/RooUnfold.html.

[5] Agostinelli, S., et al., 2003: *Geant4-a simulation toolkit*. Nuclear Instruments and Methods in Physics Research Section A: Accelerators, Spectrometers, Detectors and Associated Equipment, **506 (3)**, 250 – 303, 10.1016/S0168-9002(03)01368-8, URL http://www.sciencedirect.com/science/article/pii/S0168900203013688.

[6] Aguilar, M., et al., 2002: *The Alpha Magnetic Spectrometer (AMS) on the International Space Station: Part I – results from the test flight on the space shuttle*. Physics Reports, **366 (6)**, 331 – 405, 10.1016/S0370-1573(02)00013-3, URL http://www.sciencedirect.com/science/article/pii/S0370157302000133.

[7] Aguilar, M., et al., 2007: *Cosmic-ray positron fraction measurement from 1 to 30 GeV with AMS-01*. Physics Letters B, **646 (4)**, 145 – 154, 10.1016/j.physletb.2007.01.024, URL http://www.sciencedirect.com/science/article/pii/S0370269307001104.

[8] Aguilar-Benitez, M., et al., 2010: *In-beam aerogel light yield characterization for the AMS RICH detector*. Nuclear Instruments and Methods in Physics Research Section A: Accelerators, Spectrometers, Detectors and Associated Equipment, **614 (2)**, 237 – 249, 10.1016/j.nima.2009.12.027, URL http://www.sciencedirect.com/science/article/pii/S0168900209023444.

[9] Ahlen, S., et al., 1994: *An antimatter spectrometer in space*. Nuclear Instruments and Methods in Physics Research Section A: Accelerators, Spectrometers, Detectors and Associated Equipment, **350 (1-2)**, 351 – 367, DOI: 10.1016/0168-9002(94)91184-3, URL http://www.sciencedirect.com/science/article/B6TJM-473FRWB-2XS/2/1a3994b821abad548c27af928488d9b0.

[10] Ahn, E.-J., R. Engel, T. K. Gaisser, P. Lipari, and T. Stanev, 2009: *Cosmic ray interaction event generator SIBYLL 2.1*. Phys. Rev. D, **80**, 094 003, 10.1103/PhysRevD.80.094003, URL http://link.aps.org/doi/10.1103/PhysRevD.80.094003.

[11] Alpat, B., et al., 2010: *The internal alignment and position resolution of the AMS-02 silicon tracker determined with cosmic-ray muons*. Nuclear Instruments and Methods in Physics Research Section A: Accelerators, Spectrometers, Detectors and Associated Equipment, **613 (2)**, 207 – 217, DOI: 10.1016/j.nima.2009.11.065, URL http://www.sciencedirect.com/science/article/pii/S0168900209022803.

[12] Barwick, S. W., et al., 1997: *Measurements of the Cosmic-Ray Positron Fraction from 1 to 50 GeV*. The Astrophysical Journal Letters, **482 (2)**, L191, URL http://stacks.iop.org/1538-4357/482/i=2/a=L191.

[13] Beall, E. B., 2005: *Cosmic Ray Muon Charge Ratio in the MINOS Far Detector*. Department of Physics and Astronomy, University of Minnesota, USA, PhD Thesis.

[14] Berezinskii, V., S. Bulanov, V. Dogiel, V. Ginzburg, and V. Ptuskin, 1990: *Astrophysics of Cosmic Rays*. North Holland.

[15] Bindi, V., et al., 2010: *The scintillator detector for the fast trigger and time-of-flight (TOF) measurement of the space experiment AMS-02*. Nuclear Instruments and Methods in Physics Research Section A: Accelerators, Spectrometers, Detectors and Associated Equipment, **623 (3)**, 968 – 981, 10.1016/j.nima.2010.08.019, URL http://www.sciencedirect.com/science/article/pii/S0168900210017936.

[16] Bobik, P., M. J. Boschini, S. D. Torre, M. Gervasi, D. Grandi, K. Kudela, and P. G. Rancoita, 2009: *Galactic Cosmic Rays Modulation And Prediction For The AMS-02 Mission*. Astroparticle, Particle And Space Physics, Detectors And Medical Physics Applications - Proceedings of the 11th Conference - Villa Olmo, Como, Italy, 5 - 9 October 2009, 210 – 219, http://dx.doi.org/10.1142/9789814307529_0036, URL http://eproceedings.worldscinet.com/9789814307529/9789814307529_0036.html.

[17] Bongi, M., 2005: *Data analysis of cosmic rays at ground level with the PAMELA experiment*. Facoltá di Scienze Matematiche Fisiche e Naturali Dottorato di Ricerca in Fisica, XVIII Ciclo.

[18] Bruch, T. and W. Wallraff, 2007: *The Anti-Coincidence Counter shield of the AMS tracker*. Nuclear Instruments and Methods in Physics Research Section A: Accelerators, Spectrometers, Detectors and Associated Equipment, **572 (1)**, 505 – 507, 10.1016/j.nima.2006.10.376, URL http://www.sciencedirect.com/science/article/pii/S016890020602119X.

[19] Brun, R. and F. Rademakers, 1997: *ROOT - An object oriented data analysis framework*. Nuclear Instruments and Methods in Physics Research Section A: Accelerators, Spectrometers, Detectors and Associated Equipment, **389 (1-2)**, 81 – 86, 10.1016/S0168-9002(97)00048-X, URL http://www.sciencedirect.com/science/article/pii/S016890029700048X, see also http://root.cern.ch/.

[20] Cadoux, F., et al., 2002: *The AMS-02 electromagnetic calorimeter*. Nuclear Physics B - Proceedings Supplements, **113 (1-3)**, 159 – 165, 10.1016/S0920-5632(02)01836-4, URL http://www.sciencedirect.com/science/article/pii/S0920563202018364.

[21] Chung, C., et al., Unpublished: *AMS on ISS. Construction of a particle physics detector on the International Space Station.* AMS Internal Note Available on request.

[22] D'Agostini, G., 2010: *Improved iterative Bayesian unfolding*. arXiv, URL http://arxiv.org/abs/1010.0632.

[23] Di Falco, S., 2010: *Results of 2007 test beam of AMS-02 Electromagnetic Calorimeter*. Advances in Space Research, **45 (1)**, 112 – 122, 10.1016/j.asr.2009.08.005, URL http://www.sciencedirect.com/science/article/pii/S0273117709005419.

[24] Einasto, J., 2010: *Dark Matter*. arXiv, URL http://arxiv.org/abs/0901.0632.

[25] E.N.Parker, 1965: *The passage of energetic charged particles through interplanetary space*. Planetary and Space Science, **13 (1)**, 9 – 49, 10.1016/0032-0633(65)90131-5, URL http://www.sciencedirect.com/science/article/pii/0032063365901315.

[26] Gaisser, T., 1990: *Cosmic rays and particle physics*. Cambridge University Press, URL http://books.google.com/books?id=qJ7Z6oIMqeUC.

[27] Galaktionov, Y. V., 2002: *Antimatter in cosmic rays*. Reports on Progress in Physics, **65 (9)**, 1243, URL http://stacks.iop.org/0034-4885/65/i=9/a=201.

[28] Gleeson, L. J. and W. I. Axford, 1968: *Solar Modulation of Galactic Cosmic Rays*. The Astrophysical Journal, **154**, 1011.

[29] Greisen, K., 1966: *End to the Cosmic-Ray Spectrum?* Phys. Rev. Lett., **16**, 748–750, 10.1103/PhysRevLett.16.748, URL http://link.aps.org/doi/10.1103/PhysRevLett.16.748.

[30] Gustafsson, G., N. Papitashvili, and V. Papitashvili, 1992: *A revised corrected geomagnetic coordinate system for Epochs 1985 and 1990*. Journal of Atmospheric and Terrestrial Physics, **54 (11-12)**, 1609 – 1631, 10.1016/0021-9169(92)90167-J, URL http://www.sciencedirect.com/science/article/pii/002191699290167J.

[31] Haino, S., et al., 2004: *Measurements of primary and atmospheric cosmic-ray spectra with the BESS-TeV spectrometer*. Physics Letters B, **594 (1-2)**, 35 – 46, 10.1016/j.physletb.2004.05.019, URL http://www.sciencedirect.com/science/article/pii/S0370269304007567.

[32] Hebbeker, T. and C. Timmermans, 2001: *A Compilation of High Energy Atmospheric Muon Data at Sea Level*. arXiv, URL http://arxiv.org/abs/hep-ph/0102042v1.

[33] Hillas, A. M., 2006: *Cosmic Rays: Recent Progress and some Current Questions*. arXiv, URL http://arxiv.org/abs/astro-ph/0607109v2.

[34] Israel, M., J. George, R. Mewaldt, and G. DeNolfo, 2004: An overview of cosmic-ray elemental composition. URL http://www.srl.caltech.edu/ACE/ACENews/ACENews83.html.

[35] K. Nakamura *et al.* (Particle Data Group), 2010: *The Review of Particle Physics*. J. Phys. G, **37**, URL http://pdg.lbl.gov.

[36] Khachatryan, V., et al., 2010: *Measurement of the charge ratio of atmospheric muons with the CMS detector*. Physics Letters B, **692 (2)**, 83 – 104, 10.1016/j.physletb.2010.07.033, URL http://www.sciencedirect.com/science/article/pii/S0370269310008725.

[37] Kounine, A. and V. Koutsenko, 2011: *Flight Software for xDR and JINx nodes in AMS-02*. Internal AMS-02 note.

[38] Kremer, J., et al., 1999: *Measurements of Ground-Level Muons at Two Geomagnetic Locations*. Phys. Rev. Lett., **83**, 4241–4244, 10.1103/PhysRevLett.83.4241, URL http://link.aps.org/doi/10.1103/PhysRevLett.83.4241.

[39] Lafferty, G. and T. Wyatt, 1995: *Where to stick your data points: The treatment of measurements within wide bins*. Nuclear Instruments and Methods in Physics Research Section A: Accelerators, Spectrometers, Detectors and Associated Equipment, **355 (2-3)**, 541 – 547, 10.1016/0168-9002(94)01112-5, URL http://www.sciencedirect.com/science/article/pii/0168900294011125.

[40] Lin, C., 2005: *Trigger Logic Design Specifications*. Internal AMS-02 note.

[41] Lübelsmeyer, K., et al., 2011: *Upgrade of the Alpha Magnetic Spectrometer (AMS-02) for long term operation on the International Space Station (ISS)*.

Nuclear Instruments and Methods in Physics Research Section A: Accelerators, Spectrometers, Detectors and Associated Equipment, **654 (1)**, 639 – 648, 10.1016/j.nima.2011.06.051, URL http://www.sciencedirect.com/science/article/pii/S0168900211011752.

[42] Monfardini, A., P. Trampus, R. Battiston, and C. Gargiulo, 2005: *AMICA, an astro-mapper for AMS*. arXiv, URL http://arxiv.org/abs/astro-ph/0506377.

[43] Naumov, V. A., 2002: *Atmospheric muons and neutrinos*. arXiv, URL http://arxiv.org/abs/hep-ph/0201310.

[44] Olsen, N., et al., 2000: *Ørsted Initial Field Model*. Geophys. Res. Lett., **27 (22)**, 3607–3610, 10.1029/2000GL011930, URL http://dx.doi.org/10.1029/2000GL011930.

[45] Ostapchenko, S., 2006: *Nonlinear screening effects in high energy hadronic interactions*. Phys. Rev. D, **74**, 014 026, 10.1103/PhysRevD.74.014026, URL http://link.aps.org/doi/10.1103/PhysRevD.74.014026.

[46] Sakharov, A. D., 1991: *Violation of CP in variance, C asymmetry, and baryon asymmetry of the universe*. Soviet Physics Uspekhi, **34 (5)**, 392, URL http://stacks.iop.org/0038-5670/34/i=5/a=A08.

[47] Smart, D. and M. Shea, 2005: *A review of geomagnetic cutoff rigidities for earth-orbiting spacecraft*. Advances in Space Research, **36 (10)**, 2012 – 2020, 10.1016/j.asr.2004.09.015, URL http://www.sciencedirect.com/science/article/pii/S0273117705001997, <ce:title>Solar Wind-Magnetosphere-Ionosphere Dynamics and Radiation Models</ce:title>.

[48] Strong, A. W., I. V. Moskalenko, and V. S. Ptuskin, 2007: *Cosmic-ray propagation and interactions in the Galaxy*. ANNUAL REVIEW OF NUCLEAR AND PARTICLE SCIENCE, **57**, 285–327, 10.1146/annurev.nucl.57.090506.123011.

[49] Sullivan, J., 1971: *Geometric factor and directional response of single and multi-element particle telescopes*. Nuclear Instruments and Methods, **95 (1)**, 5 – 11, 10.1016/0029-554X(71)90033-4, URL http://www.sciencedirect.com/science/article/pii/0029554X71900334.

[50] The Fermi LAT Collaboration, 2011: *Measurement of separate cosmic-ray electron and positron spectra with the Fermi Large Area Telescope*. arXiv, URL http://arxiv.org/abs/1109.0521v1.

[51] The Pierre Auger Collaboration, 2011: *The Pierre Auger Observatory II: Studies of Cosmic Ray Composition and Hadronic Interaction model*. arXiv, URL http://arXiv:1107.4804v1.

[52] Von Doetinchem, P., et al., 2006: *Performance of the AMS-02 transition radiation detector*. Nuclear Instruments and Methods in Physics Research

Section A: Accelerators, Spectrometers, Detectors and Associated Equipment, **558 (2)**, 526 – 535, 10.1016/j.nima.2005.12.187, URL http://www.sciencedirect.com/science/article/pii/S0168900205024691.

[53] Zurbach, C. and P. Azzarello, 2010: *AMS-02 TRACKER - Tracker Calibration & Data Reduction*. Internal AMS-02 note.

List of Figures

Ringraziamenti

Il primo ringraziamento è sicuramente per la mia famiglia. Senza i loro sacrifici e la loro fiducia in me non avrei potuto sicuramente studiare fisica, non avrei mai avuto a che fare con CERN e NASA ed ora non mi troverei dove mi trovo (ed intendo proprio dove mi trovo in questo istante: Ginevra).

Il secondo ovvio ringraziamento va al gruppo AMS di Perugia. Mi seguono e investono il loro tempo in me oramai da 6 anni.
Per questa tesi, in particolare, un ringraziamento di cuore a Bruna e Alberto per il tempo "perso" a discutere ore ed ore su questo lavoro e non solo e a leggere la mia tesi ed il mio scarso inglese.
Un grazie anche a Nicola che ha contribuito in maniera molto incisiva a questa tesi e alle discussioni che hanno accompagnato questo lavoro.
Per il bagaglio di conoscenza ed esperienza maturato in questi tre anni un grazie va anche a Paolo, Giovanni e Philippe: grossa parte del profilo che oggi mi caratterizza come fisico è merito, o colpa, anche vostra.
Per il rush finale anche un grazie a Maura e Cecilia che, per il mio lavoro di tesi, hanno perso un pomeriggio facendo una delle cose in assoluto più noiose.

Per il rush finale un grazie pure a Ciccio. Quella tabella non ne voleva sapere di formattarsi correttamente...

Un grazie a tutti quelli che hanno favorito questo lavoro: il Grandi ed i milanesi tutti per il MC, Gabriele per avermi ispirato negli istogrammi residenti su disco, Capello per le nottate passate a debuggare, etc...

Un grazie al Red che domattina mi porta la tesi in segreteria, perchè con lui sono oramai 10 anni che ci troviamo a condividere la stessa strada e le stesse prospettive ed è stato un ottimo compagno di strada.

Infine un ringraziamento a Glenda che non solo non mi ostacola nelle mie scelte professionali ma mi sprona e mi segue, rinunciando probabilmente a quella che invece potrebbe essere la sua carriera.